Design and Modeling of Distal Dexterity Mechanisms for Needle-sized Robots: Systems for Lung and Endonasal Interventions

By

Philip Joseph Swaney

Dissertation
Submitted to the Faculty of the
Graduate School of Vanderbilt University
in partial fulfillment of the requirements
for the degree of

DOCTOR OF PHILOSOPHY
in
Mechanical Engineering

August, 2016

Nashville, Tennessee

Approved:

Robert J. Webster III

Michael Goldfarb

Pietro Valdastri

Robert L. Galloway, Jr.

Kyle D. Weaver

To my dearest Lori,

your unwavering love, support, and prayers

have carried me through the creation of this work.

ACKNOWLEDGMENTS

First and foremost, I want to begin by thanking the Lord who has given me the knowledge and determination to complete this work. There are truly not enough words to describe Him, but I believe Dr. S.M. Lockridge does a fantastic job attempting to in his sermon “That’s My King.” If you have not heard it before, please put down this dissertation and go listen to it. It is my hope that the work presented in this body of work glorifies Him.

I would like to extend my sincere thanks and appreciation to my advisor, Bob Webster, who has been a constant source of encouragement, support, and inspiration throughout my graduate career. Without Bob’s guidance, this dissertation would not have been possible. He was always there to listen whenever I was struggling with graduate school and would remind me that, while my work is important, there is much more to life than work. His genuine concern for his students is ever-present and guides all of his actions, giving us the best possible chance of success. Whenever I find myself in a mentorship position in the future, I will do my best to emulate the mentorship Bob provided me with. I would also like to thank my dissertation committee members: Bob Webster, Michael Goldfarb, Pietro Valdastri, Robert Galloway, and Kyle Weaver. Through each of your own innovative research and contributions to science and medicine, you have exemplified what it means to be a world-class researcher and have set a high bar to strive for in my future career. Thank you for reading this work and providing your feedback. As a result of your guidance and edits, this dissertation is stronger than anything I could produce on my own, and for this I thank you.

The work presented herein benefited greatly from the contributions of a number of mentors and colleagues. First, I would like to thank Jessica Burgner-Kahrs, who was an irreplaceable research partner during our joint time at Vanderbilt. In addition to being a great colleague, Jessica has become a trusted mentor and close friend, and I will never forget her words of encouragement during our monthly Skype calls. I would also like to

thank Hunter Gilbert, whose friendship has made my time in graduate school exponentially more enjoyable. His calm demeanor and genuine care for everyone meant that he would always put down his own work to help others, and I was the beneficiary of his generosity countless times. He is also a fantastic researcher and colleague, and I have had the pleasure of working with him on a number of research projects throughout the years. I would like to thank Art Mahoney for his friendship and mentorship, especially in the past twelve months. Art's character is exemplified by the time he left work at 10 AM to spend the entire day helping me remove spray paint from my neighbors car by hand. Needless to say, I will never spray paint when it is windy outside again. I want to thank Peter York for allowing me to mentor him during his time in our lab and for his contributions to this work. His random questions and positive outlook always brought joy and laughter to our lab. I would also like to thank Caleb Rucker for taking me under his wing during my first year in graduate school and helping to keep my head above water both academically and spiritually. I want to thank Kyle Weaver, Paul Russell, Jim Bekeny, Bryan Hartley, and Richard Feins for their clinical expertise and support of this work. During my graduate school tenure I have had the pleasure of collaborating with a number of individuals (including those mentioned above) and these collaborations have resulted in a number of great publications that I am fortunate to have my name on. I would like to thank all of my co-authors for their time and effort publishing our results.

One of the most important aspects of graduate school is the work environment, and I could not have asked for a better place to work than the MEDLab. The MEDLab is full of collaborative, selfless, and fun individuals who made my time in graduate school fly by. I want to thank all the members of the MEDLab during my graduate career (in no particular order): Loris Fichera, Isuru Godage, Art Mahoney, Raul Wirz, Ray Lathrop, Patrick Wellborn, Patrick Anderson, Neal Dillon, Michael Siebold, Andria Remirez, Rich Hendrick, Trevor Bruns, Hunter Gilbert, Jessica Burgner-Kahrs, Lou Kratchman, Jenna Gorlewicz, Caleb Rucker, David Comber, Jadav Das, and all the medical residents and undergraduates that have worked in the MEDLab. In addition to my graduate school friends and colleagues, I want to thank my close friends outside of graduate school who helped me ensure that my life did not revolve solely around my research. I want to especially thank Steve and Gracie Moakler and Wil and Kyle Shults, who have been lifelines of support these past six years. I would like to acknowledge and thank the National Science Foundation and the National Institutes of Health, who have provided the necessary funding support to pursue the research presented here. Additionally, the hard work and support of the Mechanical Engineering and Graduate School staff have been invaluable during my time in graduate school, and a special thanks goes out to Suzanne Weiss, Jean Miller, Myrtle Daniels, and Rachel Ruffin.

In addition to the many individuals mentioned above who have helped me during my time here at Vanderbilt, there are several people whom I owe more thanks than I can possibly write down. My parents, Mark and Kerry, have supported and loved me since the day I was born. Through their actions, they demonstrated to me what it means to be a hard worker and raised me to have a servant's heart. Above all, they showed me where to put my trust in times of trouble. I believe that these traits are passed down from generation to generation, and thus I owe my sincere thanks to my grandparents Bernard and Rita Swaney and Frank and Jane Miller as well. I also want to thank my sisters Mary Hannah and Rebecca for encouraging me in all my endeavors and always making time for me when I come home to visit. Two years ago, I was fortunate enough to have married into an amazing family as well. Thank you Barry and Camille for all the kind words and encouragement over the past few years and for entrusting me with your amazing daughter, and thank you Brian for keeping me laughing and focused on the big picture these past few months. Most importantly, I want to thank my beautiful wife Lori. She prayed for me, supported me, and loved me through the ups and downs of this work, and she never let me forget what was most important. While I am very proud of this body of work, my marriage to Lori is the single best thing to have come from my time in graduate school.

ABSTRACT

The central objective of this dissertation is to use mechanics and geometry to inform the design of novel, less invasive, surgical robots and tools. In the human body, there are numerous critical locations that are difficult or impossible to reach safely in a minimally-invasive fashion using existing tools and approaches. This work presents two dexterous needle-sized mechanisms that are integrated with robotic surgical systems for accessing and providing therapy to these hard to reach locations in the body. The first dexterous device developed in this work improves upon a commonly used tool for minimally-invasive access to the body: the needle.

While traditional needles provide a minimally-invasive path into the body, their usefulness could be improved if given the ability to steer and correct for errors in soft tissue through intelligent design of the needle itself. In Chapter 2, a novel type of needle is presented that uses flexures and appropriately selected needle parameters to steer through tissue, thus increasing the dexterity and clinical utility of needles. This new dexterous needle is called the flexure-tip steerable needle, and it is shown that it can achieve high curvature while reducing tissue damage. A model is developed to describe the behavior of the device, and experimental testing validates both the model and the design. The other dexterous tool developed in this work also has the diameter of a needle, but instead of steering through tissue, it was created to improve the dexterity of needlescopic manipulators.

In order to create a dexterous needlescopic tool, it is critical to utilize geometry and mechanics in the design of the tool because the small diameter of the tool makes it difficult to use traditional mechanical linkages and joints. In Chapter 3, a miniature wrist is presented that uses flexures to increase the distal dexterity of needle-sized manipulators, giving surgeons the ability to perform near scarless procedures while navigating and operating around sharp corners in the anatomy. The wrist achieves its bending motion via multiple flexure joints built into an elastic tube. The geometry of the flexure joints affect the performance of the wrist, and both kinematic and mechanics-based models are used to

model the behavior. These models reveal the dexterous motion of the device and inform design of the mechanism based on specified constraints. The models are experimentally validated, and the utility of the wrist is illustrated in a clinical scenario. Both the flexure-tip steerable needle and the miniature wrist use mechanics and geometry to aid in the design of these needle-sized surgical tools, enabling minimally-invasive access to hard to reach locations in the body.

One such location in the body that is difficult to safely reach via a minimally-invasive approach is the lung. Lung collapse is a serious complication arising from percutaneous needle-based procedures, yet transoral access, while safer, is currently limited by existing surgical tools. In Chapter 4, a robotic system is developed that integrates the flexure-tip steerable needle with two other types of continuum devices to combine the accuracy and reach of a percutaneous approach with the safety of a transoral approach. A flexible clinical bronchoscope provides transoral access to the lung, after which a concentric tube robot is used to increase the dexterity of the system, providing access to previously unreachable configurations. Lastly, the flexure-tip steerable needle deploys from the tip of the concentric tube robot to provide enhanced dexterity and accuracy to the system. Experimental results demonstrate the accuracy and utility of the system for accessing difficult to reach targets within the lung. Another location in the body that is difficult to access in a minimally-invasive fashion is the skull base.

Tumors located at the skull base are difficult to remove in a minimally-invasive fashion due to anatomical constraints that make the procedure difficult and limit its use. In Chapter 5, a minimally-invasive robotic system using needle-sized concentric tube robots is developed for removing skull base tumors through a single nostril. The surgeon operates the robotic system using a teleoperation paradigm, and an actuation unit controls the curvilinear motion of the dexterous manipulators in the skull base. Additional dexterity is provided to the tip of the manipulator by integrating the miniature wrist with the concentric tube robot. Experimental testing of the system is performed in phantom and cadaveric

models, and a system calibration method using robot arm collisions is explored.

In this dissertation, mechanics and geometry are used to inform the design of novel, less invasive, surgical robots and tools. The design and modeling of these dexterous mechanisms provide new capabilities to needle-sized surgical tools, which are then utilized in robotic systems developed for minimally-invasive treatment of lung and skull base cancers. The goal in developing these dexterous mechanisms and surgical robotic systems is to provide physicians with better minimally-invasive tools and systems in order to improve the treatment of their patients. The novel surgical robots and tools developed in this work ultimately have the potential to positively impact many lives by improving the standard of care for a multitude of procedures.

TABLE OF CONTENTS

Page

Chapter

Appendix

LIST OF TABLES

LIST OF FIGURES

Figure Page

Chapter 1

Introduction

1.1 Motivation

There was a time not long ago when just the mention of a robot in the operating room would seem absurd, with people imagining C-3PO from Star Wars or the T-800 robot from The Terminator performing surgery. However, in the 30 short years since the first robot was used to perform a neurosurgical biopsy in 1985 [15], an entire subfield of robotics has been created that centers around robots in the operating room. There are now multiple commercial companies selling surgical robot systems, with over 2 million robotic procedures performed to date. Commercially available surgical robots are used for assisting with bone drilling [16], placement of surgical instruments in the brain [17], steerable catheters [18], and robotically-assisted laparoscopic and endoscopic systems [19, 20, 21] (see Fig. 1.1 for images of several commercial surgical robotic systems). There has even been a set of guidelines developed for how to best integrate surgical robots into the operating room [22], making it clear that surgical robots are here to stay. Robotic surgical systems offer a multitude of benefits to the surgeon, including:

1. better dexterity when compared with existing non-wristed laparoscopic instruments,
2. the ability to restore correct hand-eye coordination of the surgical instruments,
3. increased precision of the tools, and
4. the potential for improved ergonomics,

among others. In the end, these benefits provide physicians with better minimally-invasive tools and systems in order to improve the treatment of patients.

Figure 1.1: (a) The RIO orthopedic surgical robot. ©*2015 Mako Surgical Corp.* (b) The Sensei robotic catheter system ©*2015 Hansen Medical* (c) The Pathfinder neurosurgical robot ©*2012 Prosurgics, Inc.* (d) The da Vinci laparoscopic surgical robot. ©*2015 Intuitive Surgical, Inc.*

To date, the most successful surgical robot is the da Vinci surgical system, which uses robotic arms to control laparoscopic tools with wristed end effectors [21]. While the da Vinci is by far the most successful commercial system and provides both patients and surgeons with the benefits listed above, it is not without its shortcomings. For example, the diameter (8 mm) of the tools combined with the rigid nature of the tool shafts limit the areas in the body where the system can safely be used. While the size of the tools and the rigid tool shafts are not problematic when operating within an insufflated abdomen, it becomes a major challenge to use the da Vinci when attempting to safely maneuver in tight anatomical spaces such as the brain or the lungs. Fortunately, the surgical robotics research community has set out to address these shortcomings with the next generation of surgical robots.

1.2 Dexterous Continuum Devices

A major push in surgical robotics research is the creation of systems that are smaller, inherently safe, and provide access to locations that rigid instruments and devices cannot access. These systems often employ flexible, curved tool shafts that enable surgeons to access and operate in hard to reach locations, providing alternative routes to the target that utilize natural orifices or small incisions. The use of continuously flexible robots (i.e., “continuum robots”) in medicine is aimed at improving dexterity while minimizing the size of the tools (see e.g., [23, 24, 25]).

One example of such a system is the Hansen Medical Sensei robotic catheter. This dexterous continuum device is comprised of a controllable guide sheath and a robotic catheter that uses tendons to actuate a flexible distal tip [18]. The steerable catheter is 4.8 mm in diameter and is controlled by a surgeon using a teleoperated master device. The use of robotics in this application allows the surgeon to intuitively control the catheter tip while employing tools such as motion scaling and force feedback. Researchers have also used multiple constrained continuum backbones operated in a push-pull manner to create a 4.2 mm dexterous, flexible robot for use in throat surgery [26] and single port abdominal surgery [27]. In [28], a 10 mm dexterous continuum manipulator is described that uses many rigid cylindrical links connected by cables, allowing the device to deploy in a follow-the-leader approach in 3D space. The device was originally investigated for cardiac procedures, but has now been commercialized for use in transoral throat surgery [29]. A common theme among each of these continuum devices is that they make intelligent use of geometric constraints to provide surgeons with additional dexterity at a small scale.

Steerable needles and concentric tube manipulators are two other types of small continuum devices that can be made more dexterous through the use of geometry and mechanics, enabling usage in critical locations inside the body. In the sections that follows, work related to the design and modeling of these small dexterous mechanisms is reviewed. Existing robotic approaches for the treatment of lung and skull base diseases are also reviewed, as these are the two clinical applications targeted in this dissertation using the dexterous mechanisms developed.

1.3 Design of Steerable Needles

Researchers have used different design approaches to cause needles to move in a predefined way, effectively creating a dexterous steering tool that can improve accuracy and curve around obstacles. One example is the use of shape-memory actuators (SMA) to change the needle shape and direction upon insertion into soft tissue using both one [30] and two discrete active bending joints (see Fig. 1.2(a)) [1]. While both of these designs can actively change their shape in a predefined way, the time response and heat generation of the shape memory actuator used to alter the needle shape may be challenging in clinical use. Another approach for needle articulation is the use of tendons to actuate the tip of a needle (see Fig. 1.2(b)) that is connected to the needle shaft with a ball joint [2]. This creates a dexterous needle tip but comes at the expense of simplicity, since multiple tendons must be carefully constrained to create controllable actuation of the tip. Another approach to actively change the needle shape involves geometrically constrained interlocking fibers that change the shape of the needle when translated with respect to one another [31]. While each of these approaches provide added dexterity, in this dissertation a simpler approach to achieve the same steering objectives will be sought. A simpler design will facilitate manufacturability and enable fabrication at smaller sizes.

One such approach that has previously been suggested is bevel-tip steered needles, which use the geometry of their asymmetric tip to create lateral forces that cause a flexible needle shaft to bend in a predictable direction when inserted into tissue. The bend direction can be changed by axially rotating the needle shaft, enabling 3D control using only two

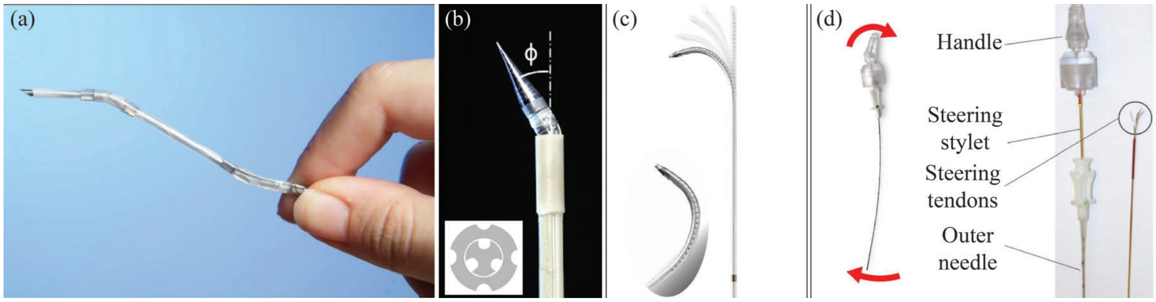

Figure 1.2: (a) A dexterous steerable needle that uses discretely actuated shape-memory actuators [1]. (b) A steerable needle with an active needle tip controlled using tendons [2]. (c) The clinically available Osseoflex Steerable Needle is a 10 gauge needle that uses a tendon-actuated distal tip for vertebral augmentation surgery [3]. (d) The PneumRx needle could actively change its shape using push pull actuation of flexible nitinol tendons [4].

inputs. This creates a simple yet dexterous needle in which the curved shape of the needle shaft remains unchanged as the tip of the needle moves forward through tissue (i.e. “follow-the-leader” deployment).

Bevel-tip steered needles have achieved the greatest interest from the research community as it pertains to tip steered needles (see Fig. 1.3 for examples). The motion of bevel-tip steerable needles is often modeled using a simple nonholonomic unicycle or bicycle model [32], though others have included additional effects such as the complex needle-tissue interaction forces [33, 34] and torsion experienced along the needle shaft [35, 36]. In order to maximize the utility of bevel-tip steerable needles though, researchers have sought to increase their workspace by increasing the achievable curvature of the needles.

The simplest approach to increase needle curvature is to use a kinked bevel-tip needle design which will be more fully described in Chapter 2. This design takes advantage of the geometry of the kinked needle tip to create even greater tip forces than bevel-tip needles, thus increasing the curvature of the needle [37]. However, these needle designs have two significant drawbacks. First, the geometry of kinked bevel-tip tips cut large helical tracks in tissue when the needle is axially rotated during insertion, which is required to steer it to a desired location. Second, the rigid nature of the kinked tip make it difficult or impossible to deploy with a clinical coaxial needle system. Thus, these drawbacks limit

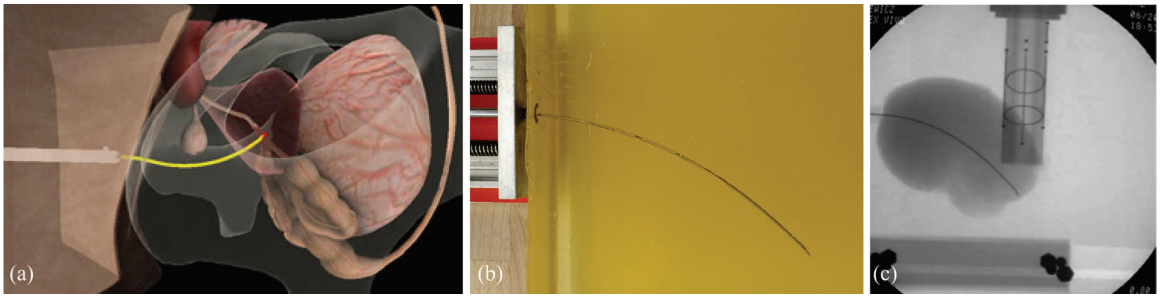

Figure 1.3: (a) A simulated needle path around obstacles is shown with a bevel-tip needle [5]. (b) A steerable needle path through gelatin shows the needle achieving appreciable curvature [6]. (c) An X-ray image shows a steerable needle after insertion into an ex vivo kidney [7].

the clinical usefulness of existing high curvature bevel-tip steerable needles. In Chapter 2, a novel type of steerable needle is presented that increases the dexterity and clinical utility of the needle, while also reducing tissue damage when compared with kinked bevel-tip needles. The new steerable needle utilizes geometry and mechanics to inform the design of a passively actuated flexure joint, whose elastic nature motivates the creation of a new kinematic model that accounts for motion of the flexible needle tip to better predict the behavior of the needle. In Chapter 3, the same geometry and mechanics principles are applied to the design of needle-sized wrists for teleoperated surgical robots. The following subsection provides the background for these devices.

1.3.1 Dexterous Mechanisms for Needle-sized Manipulators

Due to the small diameter of needle-sized manipulators such as needlescopic instruments (<3 mm) and concentric tube robots (typically <2 mm), the use of traditional articulating wrist-like mechanisms (e.g., [38, 39] for reviews) is challenging and often impossible. Based on this researchers have sought to use continuum structures that are made from elastic materials, where intelligent use of mechanics and geometrical designs cause the structures to bend in a predetermined manner. In [8], a dexterous device was developed that used mechanics to enable motion of multiple continuum structures comprised of flat springs arranged in a circle around the shaft of the device (see Fig. 1.4(a)). The springs

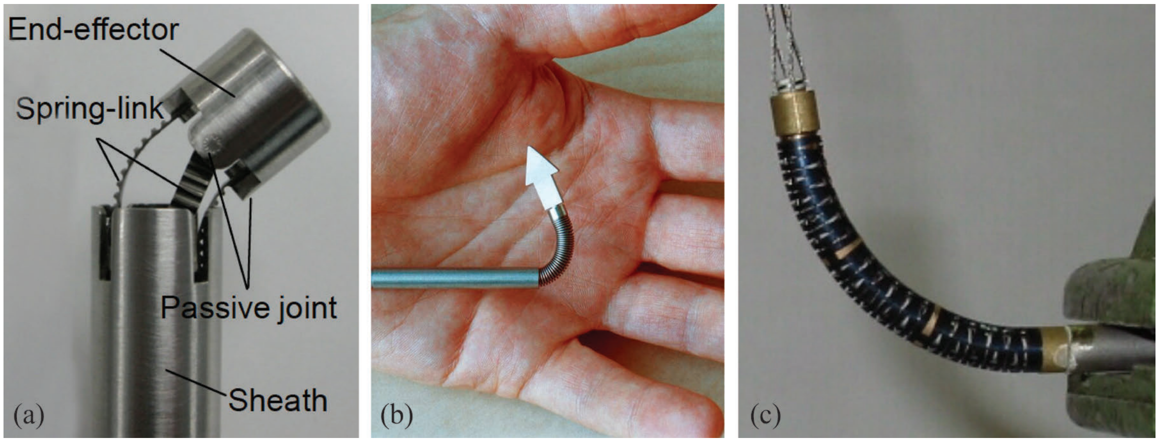

Figure 1.4: (a) a dexterous device comprised of multiple continuum structures arranged around the shaft of the device [8]. (b) A continuum mechanism made using a ring of cables sandwiched between two coil springs provides high tip dexterity [9]. (c) A distal dexterity mechanism made from an elastic nitinol tube that has been laser machined in a specific pattern [10].

were actuated using a rigid link attached to the springs by a pin joint. In [9], a dexterous continuum device is made using a ring of cables that is geometrically constrained axially along the tool shaft between an outer and inner set of coil springs [9]. By pulling the cables on one side of the device and releasing the cables on the other, the continuum mechanism bends in an arc (see Fig. 1.4(b)).

The use of multiple flexible backbones routed through a series of spacer discs has also been shown to provide added dexterity in a continuum structure [40], as has a flexible tubular nitinol structure design that is actuated with multiple tendons [41]. In [42], a tendon-driven flexible catheter is studied and detailed mechanics based models are developed for the dexterous catheter. Another modeling approach for continuum robots and mechanisms is to use a constant curvature approximation, due to the simplifications this assumption enables in kinematic modeling. For a review of several different continuum modeling approaches that utilize the piecewise constant curvature assumption, see [43]. An example continuum mechanism that uses the constant curvature assumption is the hybrid style parallel continuum robot developed in [44]. While the designs presented above all improve the dexterity of surgical devices, those that utilize the fewest components are most desirable for miniaturizability and manufacturability for needle-sized manipulators.

One method for achieving a dexterous continuum mechanism with the minimum number of components is to create a compliant bending region in an elastic member, often utilizing geometric patterns to constrain the motion of the device. For example, one group developed a 10 mm tool for endoscopic camera steering using a nitinol tube (see Fig. 1.4(c)) with an intricate geometric pattern laser-machined into the tube [10]. Another group used a similar concept to create a 6 mm tendon-actuated tool for arthroscopy [45]. Others have created dexterous continuum mechanisms for use with catheters by laser-machining springs into an elastic backbone and using hydraulic suction for actuation [46], while another group created a 3.8 mm dexterous catheter tip using a laser-machined elastic member actuated with a tendon and a restoring spring [47].

Although each of the designs above feature a dexterous manipulator, this work set out to create a device that was truly needle-sized yet simple to manufacture and actuate using the fewest number of tendons, while also providing the largest possible lever arm over which the tendon can act for a tube of a given diameter. In Chapter 3, a compliant bending region is designed into an elastic tube by cutting away a predetermined geometric shape from the tube, thus creating a dexterous, needle-sized wrist actuated using a single tendon. The shape of the compliant bending region and the mechanics of actuating the wrist are coupled with a piece-wise constant curvature assumption to model the behavior of the wrist, informing an appropriate design for the desired task. By utilizing geometry and mechanics to aid design, both the flexure-tip steerable needle and the miniature wrist can be integrated with robotic systems to provide minimally-invasive, dexterous access to hard to reach locations in the body.

1.3.2 Systems for Treating Lung Cancer

Although lung cancer is the deadliest form of cancer in the United States [48], there have been few robotic systems developed to treat it. Perhaps one of the main reasons why there has been limited work toward a robotic system for treating lung cancer is the difficult anatomy such a system would have to navigate. Unlike laparoscopic procedures in the abdomen that use insufflation to enlarge the abdominal cavity, there is no large, cavernous space in the lung in which to maneuver. This places a premium on small dexterous devices. Additionally, the tortuous path through the bronchial tree and the fragility of lung tissue make lung collapse a real danger and necessitate a robotic system that can perform follow-the-leader motion through lung tissue while being deployed transorally.

Robotic stereotactic radiosurgery has been performed using the Cyberknife System (see Fig. 1.5(a), Accuray Incorporated, USA) on patients who are unfit to undergo lung tumor resection. The Cyberknife approach uses a large robotic arm to precisely aim a radiation beam at the tumor from many different positions, effectively targeting the tumor while leaving the surrounding tissue with only a small dose of radiation [49]. The system also has the benefit of being able to compensate for breathing motion. Downsides to the system include the large space required to house it and the high cost of the system, meaning that only high volume centers will likely be able to provide such treatment. Researchers have also developed a robotic system for implanting radioactive seeds directly into the lung to treat tumors that are difficult to reach [50]. Such a system provides the surgeon with precise manipulation of the brachytherapy needle, thereby increasing the accuracy of seed placement, while also reducing the radiation dose to the surgeon. While promising, this system does pose a serious risk of lung collapse during placement of the radioactive seeds, as the outer membrane of the lung must be cut to access the tumor.

The combination of image-guidance and existing surgical tools (e.g., bronchoscopes and needles) has resulted in different types of systems aimed at increasing the efficacy of lung biopsy. Two commercial systems have been developed that utilize a bronchoscope and electromagnetic guidance to assist with the navigation of small, magnetically-tracked instruments deployed through the bronchoscope (see Fig. 1.5(b), [51, 52]). These systems allow the physician to navigate deeper into the bronchial tree to reach suspicious nodules

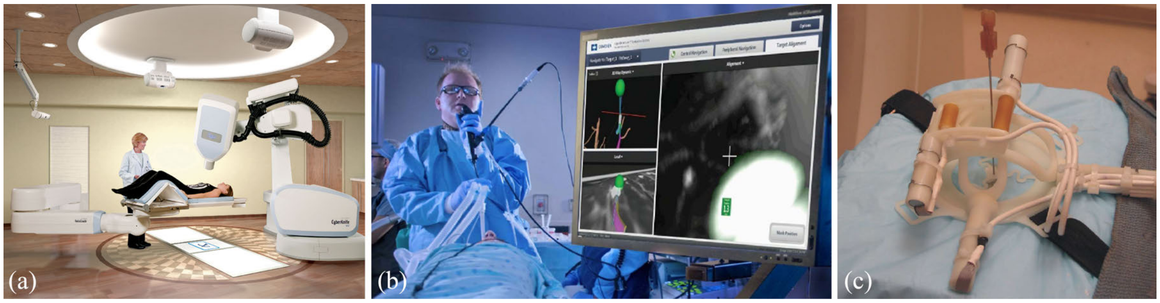

Figure 1.5: (a) The CyberKnife robotic stereotactic radiosurgery system ©*2016 Accuray Inc.* (b) The superDimension electromagnetically tracked bronchoscope system ©*2016 Medtronic* (c) A patient-mounted image-guided robotic system developed for percutaneous interventions [11].

for biopsy. Unfortunately, these systems have limited diagnostic yield for smaller nodules, and they are still only intended to navigate within the bronchial tree using a bronchoscope. Image-guided robotic systems have also been developed for percutaneous lung access, including the use of an industrial robot manipulator to drive a rigid needle toward a target under CT-guidance [53]. A custom patient-mounted robotic system was developed to control a needle in a scanner without imaging artifacts (see Fig. 1.5(c), [11]), and a similar approach was taken in [4] but included control of a tendon-actuated steerable needle. While these robotic systems all provided accurate targeting through the integration of needles and image-guidance, they all pose a serious risk of lung collapse since the needles must cut through the outer membrane to reach the lung.

In this work, we set out to create a robotic system that could combine the safety of a transoral approach with the efficacy of a percutaneous approach. Toward this end, the surgical system presented in Chapter 4 couples a flexible bronchoscope with a new distal dexterity mechanism for concentric tube robots and the dexterous flexure-tip steerable needle developed in Chapter 2. The system deploys transorally to maneuver through the bronchial tree and then operates as a steerable needle when deployed into the soft lung tissue, accurately reaching the target via a transoral approach. Another critical location in the body that is difficult to access in a minimally-invasive fashion is the skull base.

1.3.3 Systems for Treating Skull Base Tumors

The skull base is located at the approximate center of the head, and it is here that 15-20% of all primary brain tumors arise, making it a critical location to reach [54]. Safely removing tumors from the skull base using a minimally-invasive, endonasal approach requires passing multiple tools through a single nostril where they must traverse a long, constrained corridor to reach the surgical site. Visualization must also be provided through this same anatomical corridor, adding to the complexity of an already difficult procedure. The need for controlling so many tools through a single nostril necessitates the use of at least one other surgeon or assistant to help maneuver all the tools, further increasing the complexity of the procedure. Once at the skull base, there are the additional challenges of providing dexterity to the surgical tools through constrained anatomy and accurately knowing where each tool is located with respect to the others. Due to all of these challenges, pituitary tumors are often still removed using open, extremely invasive approaches.

To address one or more of the above challenges, there have been a few robotic systems designed to operate at the skull base through either a transnasal or transoral approach. Surgeons have attempted to use the da Vinci surgical system to access and operate at the skull base with limited success (see Fig. 1.6(a), [12]). Rather than approach the skull base through the nostril, which provides good access to the skull base, the large diameter of the da Vinci's robotic arms require an invasive transoral approach. This approach limits the net benefit to the patient, and indicates that a smaller, more dexterous system is needed. A new clinical system has been proposed for endoscopic skull base surgery that uses multiple continuum segments deployed in an inchworm-like fashion to snake a flexible endoscope through the body to the surgical site, after which two end effectors are deployed from the tip of the endoscope (see Fig. 1.6(b), [13]). While this system shows the benefit of using flexible, continuum structures to provide dexterity when operating in tight anatomical spaces, the large diameter of the system requires an invasive transoral approach similar to the da Vinci. Systems have also been developed that provide the surgeon with a robotically

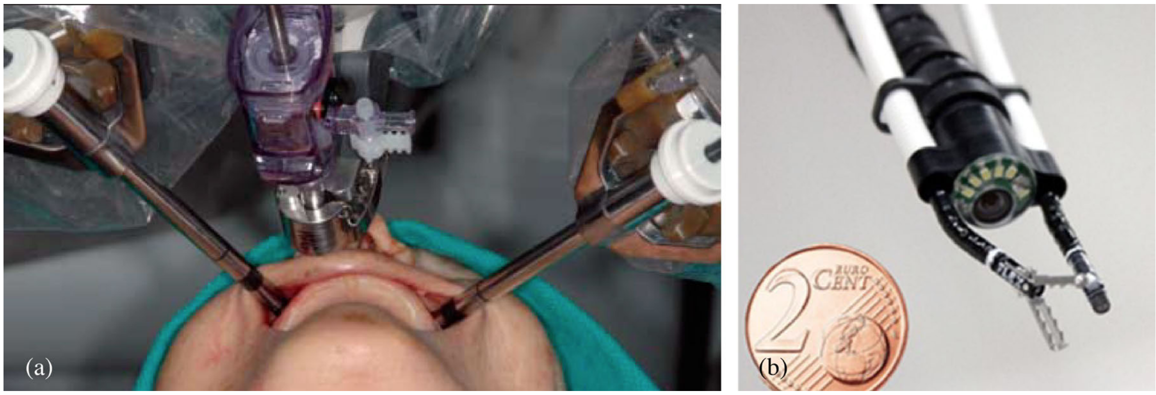

Figure 1.6: (a) The da Vinci system has been attempted for skull base surgery, but the tools require an invasive transoral approach rather than the endonasal approach [12]. (b) A new snake-like continuum robot has been investigated for skull base surgery, but the diameter again prevents an endonasal approach [13].

controlled endoscope for the skull base [55, 56, 57]. While these systems do offset the burden of controlling the endoscope from the surgeon, they do not provide flexible, dexterous tools that can assist the surgeon with removing the tumors.

In Chapter 5, a minimally-invasive robotic system using needle-sized concentric tube robots is developed for removing skull base tumors through a single nostril. The surgeon operates the robotic system using a teleoperation paradigm, and an actuation unit controls the curvilinear motion of the dexterous manipulators in the skull base. Additional dexterity is provided to the tip of the manipulator by integrating the miniature dexterous wrist developed in Chapter 3 with the concentric tube robot. Experimental testing of the system is performed in phantom and cadaveric models, and a system calibration method using robot arm collisions is explored.

1.4 Dissertation Overview and Contributions

The goal of this dissertation is to improve surgery (and thereby eventually patient care) through the development of needle-sized surgical tools and robotic systems that incorporate novel distal dexterity mechanisms. The use of mechanics and geometry to inform design results in a novel steerable needle and miniature wrist, which are then integrated into robotic systems developed for minimally-invasive treatment of lung and skull base cancers. This body of work aims, in the longer term, to improve patient care by enabling minimally-invasive treatment of diseases found deep within the body using new surgical robots and dexterous tools. It is intended that the work presented herein will leave a lasting impact on healthcare as others continue to build upon these results and push the boundary of what is possible in the operating room. The chief contributions of this work are summarized below:

1.4.1 Design

In this dissertation, the basic concepts of mechanics and geometry are coupled to design novel distal dexterity mechanisms. Using these ideas, it is possible to selectively alter the bending stiffness of a device along its length or constrain a device to move in a predefined way, resulting in changes to the overall device performance. Design examples found in this dissertation include a steerable needle that incorporates a flexure element located between the needle tip and shaft (Chapter 2, [6]), a miniature wrist integrated into an elastic tube that uses cutout sections of tube to decrease bending stiffness and create a dexterous device (Chapter 3, [58]), and a non-annular concentric tube robot that uses geometry to enable previously unreachable robot configurations and prevent elastic instability (Chapter 4, [59]). All of these designs use elastic materials, and the key to each device is that mechanics and geometry have informed the design in such a way as to enable desired motion and performance of the device.

1.4.2 Modeling

The modeling contributions of this dissertation are the kinematic and mechanics-based models that describe the behavior of the aforementioned needle-sized distal dexterity mechanisms. When modeling miniature elastic devices such as these it is often necessary to analyze both the kinematics and mechanics of the devices in order to predict the overall behavior of the device. For example, modeling the interaction of the tissue force and spring-like flexure element to determine the behavior of the flexure-tip needle and its trajectory through tissue requires both kinematic and mechanics-based modeling as described in Chapter 2 [60]. Similarly, modeling the miniature cutout wrist in Chapter 3 takes into account the geometry of the wrist and subsequent kinematic motion as well as the forces required to actuate the wrist in order to inform an appropriate design for the task at hand [58].

1.4.3 Systems

The design and modeling of distal dexterity mechanisms outlined above are incorporated into two surgical robotic systems in this dissertation. The first system, described in Chapter 4, provides transoral access to difficult or impossible to reach locations in the lung for biopsy of suspicious nodules [61]. The robotic lung system incorporates three continuum devices that have never been combined before to enable the accuracy of a percutaneous approach with the safety of a transoral approach. Our system sequentially deploys the following devices: a tendon-actuated bronchoscope, a concentric tube robot, and a flexure-tip steerable needle. The lung system incorporates the flexure-tip steerable needle with a previously developed needle steering controller to accurately reach the target. The second system, detailed in Chapter 5, is designed to provide a minimally-invasive robotic approach to endonasal tumor removal and delivers four concentric tube robot arms through a single nostril to the skull base under teleoperated surgeon control [62]. Because the approach to the skull base is through a long and narrow corridor, the use of the miniature wrist provides added dexterity to the endonasal system at the surgical site. With the endonasal system deploying multiple concentric tube robot arms to a delicate location in the body, a system procedure for calibration of multiple robot arms using collisions is also presented.

Chapter 2

Flexure-Tip Steerable Needle

2.1 Chapter Overview

In the quest to design higher curvature bevel-steered needles, kinked bevel-tips have been one of the most successful approaches yet proposed. However, the price to be paid for enhancing steerability in this way has been increased tissue damage, since the pre-bent tip cuts a local helical path into tissue when axially rotated. This is problematic when closed-loop control is desired, because the controller will typically require the needle to rotate rapidly. It is also difficult or impossible to use kinked bevel-tip needles in a clinical coaxial needle system because the kinked tip cannot pass through a tightly toleranced coaxial introducer needle. In this chapter we present a new type of steerable needle called the flexure-tip needle that overcomes these challenges. The flexure-tip needle design provides the enhanced steerability of kinked bevel-tip needles, while simultaneously minimizing tissue damage, and the needle can also be deployed through a coaxial introducer needle. The curvature of the flexure-tip needle is compared with a kinked bevel-tip needle and shown to be similar, and the reduced tissue damage of the flexure-tip needle is illustrated. A model predicting the behavior of the dexterous flexure tip is derived and experimentally tested, opening the door for integration of the flexure-tip needle with existing needle steering planners. The flexure-tip needle described in this Chapter was published in IEEE Transactions on Biomedical Engineering [6] and the modeling results are in preparation for submission to IEEE Transactions on Robotics [60]. The needle design has been patented (US 14/208,508) and we are in active discussions with a large medical device company to commercialize the needle as a hand-held device for correcting misalignment of coaxial biopsy needles.

2.2 Introduction

Needles are one of the least invasive tools available to reach sites requiring diagnoses or interventions in the human body. Many different procedures can be performed with needles including biopsy, thermal ablation (using either heat or cold), brachytherapy, and drug delivery, among others [63]. The efficacy of these needle-based procedures typically relies heavily upon the accuracy with which the needle tip reaches the desired location specified by the physician on medical images. However, there are numerous factors that contribute to needle placement inaccuracy, including tissue deformation, registration error, and (in the case of hand-held needles), the surgeon's hand-eye coordination. There are also situations where a straight-line path to the surgical site is not possible because of anatomical constraints. Examples include deep brain stimulation, where certain targets can be obstructed by eloquent brain tissue [64] and transperineal prostate brachytherapy, where the pubic arch can sometimes obstruct a portion of the prostate [65]. It may also be desirable to reach multiple sites within the target area without full retraction of the needle [64].

Steerable needles have recently received a great deal of interest in the medical robotics community (see [63, 66] for reviews), because they have the potential to address both accuracy enhancement and obstacle avoidance. In this chapter we consider only the subset of steerable needle research that addresses flexible needles that harness asymmetric tip forces (often combined with rotation of the needle shaft) to guide the needle through curved paths to reach a target. These needles, which typically feature a bevel tip, are able to enhance accuracy by enabling closed-loop control [67, 68], and can also enable the needle to steer around obstacles [64, 69] using pre-planned trajectories.

While there has been a great deal of recent progress on needle modeling and control (see e.g. [70, 66, 67, 71, 72, 73], among many others), comparatively little attention has been paid to needle design. One noteworthy design is a hand-held steering device that deflects a traditional biopsy needle through a curved path by varying the exposed length of a precurved stylet [74]. Another uses two interlocking shaft halves that can be extended relative to one another to steer the needle [75]. With bevel-tip needles, design studies have investigated the effects of bevel angles on curvature and bevel-tissue interaction parameters and needle curvature [70, 76]. The effects of kinked tips have been studied to enhance needle curvature [37], and tips that are larger than the needle shaft and are kinked [72] have also been used for this purpose.

Thus, much prior steerable needle work has considered a beveled or a kinked and beveled tip, with the latter enabling higher curvature and thus better steerability. An approach for adjusting the curvature of such a needle during insertion is duty-cycling [72], which is achieved by interspersing short periods of rapid axial rotation with short periods of a fixed axial angle during insertion. Using a kinked bevel-tip needle with duty-cycling yields high curvature capability with real-time curvature adjustment. However, a kinked bevel-tip that is rapidly rotated during insertion cuts a helical path through the tissue larger than the needle's shaft, due to the rigid nature of the kinked tip. The desire for high curvature steerable needles that do not cut helical paths through tissue motivated the design of a new type of steerable needle.

In this chapter, we present a new bevel-tip steerable needle design that incorporates a flexure. The flexure enables the needle to act like a kinked bevel-tip needle when inserted, while at the same time acting like a traditional bevel-tip needle when axially rotated. A kinematic model is developed for the flexure-tip needle in order to predict the behavior of the flexure and the influence it has on the overall needle trajectory. The flexure-tip needle design is able to provide high steerability with less tissue damage while still being able to pass through a coaxial introducer needle.

2.3 Flexure-Tip Needle Design

The flexure-tip needle consists of three parts: a flexible straight needle shaft, a beveled tip, and a flexure joint. During insertion into tissue, the bevel tip produces a transverse load

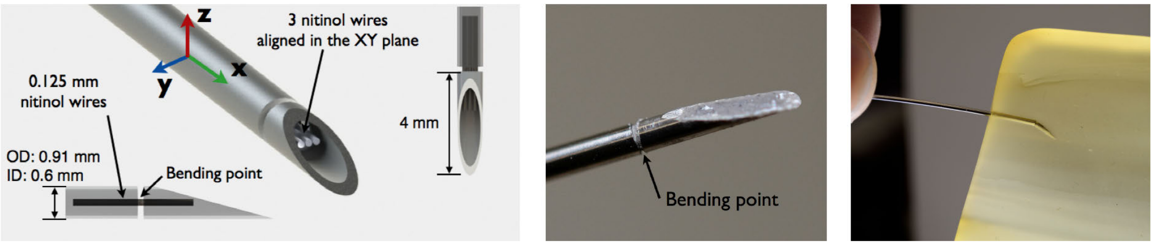

(a) (b) (c)

Figure 2.1: Flexure-tip needle design. The nitinol wires that comprise the flexure joint bend at the gap between the needle shaft and the tip as forces are applied to the bevel tip by tissue. (a) A CAD drawing of the flexure-tip needle concept with dimensions shown. (b) A close-up of the flexure-tip prototype. The nitinol wires are held in place by a cold weld epoxy in both the bevel tip and the needle shaft, which begin as tubes. (c) The flexure-tip bends in the direction of the bevel when inserted into tissue due to reaction forces on the bevel that cause the nitinol wires to deflect, thus kinking the tip of the needle.

which causes the needle to bend at the flexure (see Fig. 2.1(c)). As will be shown shortly, during pure insertion, this causes the needle to behave like a kinked bevel-tip needle (the fact that it has the same shape can be seen in Fig. 2.1(c)). However, during pure rotation, the flexure enables the needle to stay in place while spinning to reorient the bevel, without tearing through tissue.

The prototype needle used for the experiments presented in Section 2.4 has a flexible shaft (made from nitinol, see Fig. 2.1(b)) with an outer diameter (OD) of 0.91 mm and an inner diameter (ID) of 0.60 mm. The beveled tip section has the same OD as the shaft, is 4.0 mm long at its longest point, and features a 10 ° bevel angle. The flexure joint that connects the needle shaft and the tip section is made of three 0.125 mm diameter nitinol wires laid side by side in the middle of the needle, and oriented so that their least stiff direction is the one in which the bevel would naturally make the needle bend during tissue insertion (see Fig. 2.1(a)). The gap between the tip section and the needle shaft is approximately 0.15 mm, which allows the tip to flex to a maximum angle of roughly 22 °. To attach the wires to both the shaft and tip section, cold weld epoxy (J-B Weld, USA) was used. For a detailed step-by-step manufacturing process for the needle, see Appendix A.

The in-plane stiffness of the flexure joint (i.e., movement of the tip in the XZ plane

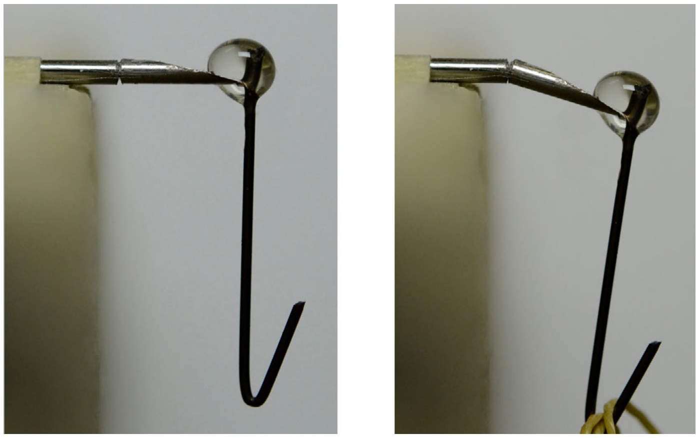

Figure 2.2: Experimental flexure stiffness test setup.

in Figure 2.1(a)) was determined experimentally by hanging weights from the beveled tip using a drop of glue and a hook (see Fig. 2.2) in 5 g increments. The resulting stiffness for the flexure was approximately 3.6 mNm/rad. The out-of-plane stiffness was determined to be 16.5 mNm/rad using the same experimental procedure.

2.4 Needle Characterization

To determine if the flexure-tip needle could accomplish the goals of high curvature and reduced tissue damage, we began by determining whether we could achieve curvatures similar to the kinked bevel-tip design we sought to replace. We then investigated whether duty-cycling was possible with the new needle, before lastly exploring tissue damage.

2.4.1 Curvature Comparison to Kinked Bevel-Tip Needle

We constructed a kinked bevel-tip needle using as the shaft the same nitinol tube used to make our flexure-tip needle (0.91 mm OD × 0.6 mm ID). We constructed a kinked tip from a stainless steel wire with a 0.91 mm OD, a bevel angle of 15 °, and a kink angle of approximately 25 ° at a point 4 mm from the tip. When inserted into a tissue phantom made from 10% by weight Knox Gelatin (Kraft Foods Global Inc., USA), the flexure-tip needle is able to achieve a comparable curvature to the kinked bevel-tip needle (see Fig. 2.3).

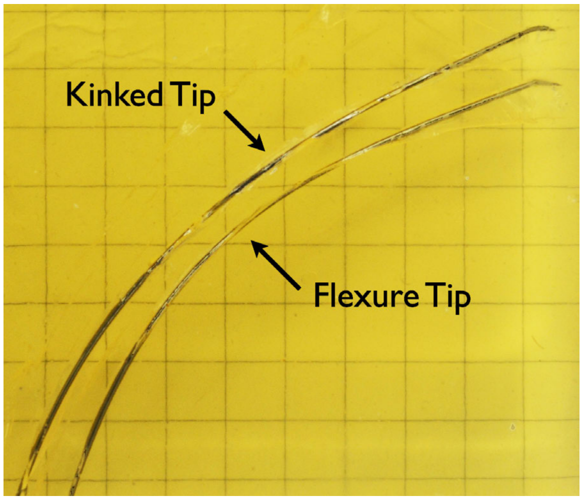

Figure 2.3: Curvature comparison of kinked bevel-tip needle and flexure-tip needle.

2.4.2 Feasibility of Duty-Cycling to Adjust Curvature

As proposed by Minhas et al. [72], duty-cycling adjusts needle curvature by alternating between periods of insertion without rotation, and insertion while constantly spinning the needle. To explore whether our flexure-tip needle was capable of providing adjustable curvature via duty-cycling, we performed the following experiment.

Two tissues were prepared: a 10% by weight Knox Gelatin tissue phantom, and *ex vivo* pork loin. The flexure-tip needle was inserted into these tissues with a constant insertion velocity of 0.5 cm/sec, and constant rotational velocity (during the periods of the duty-cycle when axial rotation occurs) of 4 rev/sec. Insertions were performed with duty-cycle ratios of 0%,20%,33%,50%,66%,80%, and 100% in phantom tissue, and 0%,25%,50%,75%, and 100% in pork loin, with 0% indicating no axial rotation, and 100% indicating constant axial rotation. When not axially rotating, the bevel orientation was always the same, such that the needle paths were all in the same plane. Fig. 2.4 shows superimposed images of several flexure-tip needle insertions into both tissue types. The radius of curvature for each duty-cycle ratio was determined by visually fitting a circle to the needle paths. Figure 2.4(c) shows the curvature with respect to the duty-cycle ratio in phantom tissue. The linear fit agrees with the results obtained in [72] using a kinked bevel-tip needle. The max-

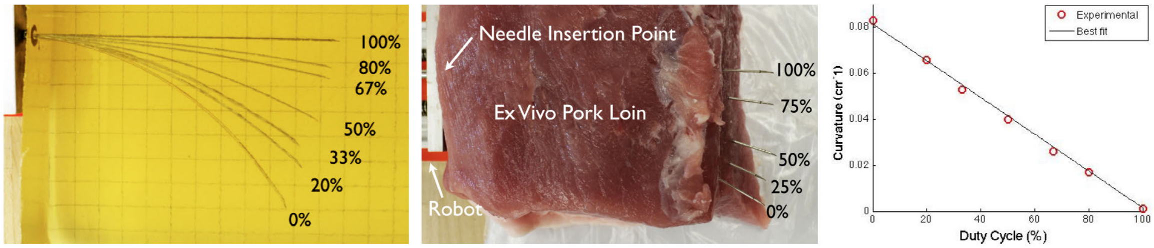

(a) (b) (c)

Figure 2.4: Achievable needle curvatures in phantom and biological tissue. (a) Superimposed insertions into phantom tissue. (b) Superimposed insertions into *ex vivo* pork loin. (c) Curvatures achieved for varying duty-cycle ratios in phantom tissue.

imum nominal radius of curvature of the flexure-tip needle (0% duty-cycle) was 12.1 cm in phantom tissue, and 17.6 cm in *ex vivo* pork loin.

2.4.3 Tissue Damage

While duty-cycling is a good method for adjusting the curvature of a steerable needle during insertion, it can cause damage to the tissue surrounding the needle. For a qualitative assessment of tissue damage caused by needle insertion using duty-cycling, we inserted the kinked bevel-tip needle, a clinical bevel-tip needle, and the flexure-tip needle (described in Sec. 2.4.2) into phantom tissue (10% by weight Knox gelatin). The clinical bevel-tip needle (Becton Dickinson & Co., USA) was a 20 gauge spinal needle (OD 0.91 mm) with an 18 ° bevel angle. Each needle was inserted with a constant velocity of 0.5 cm/sec, and constant axial velocity of 4 rev/sec (that is, a duty-cycle of 100%). After insertion, the needle was retracted using the same parameters with the intent of having its tip follow the same path as during insertion. Liquid dye was then injected into the insertion hole to visualize the needle path (see Fig. 2.5). As one can see in Fig. 2.5, because of the spinning of the kinked bevel-tip, the needle slices through the tissue in a local helical pattern during insertion. Note however, that the flexure-tip needle's tissue damage under these conditions is comparable to the path created by the clinical bevel-tip needle and the flexure-tip needle does not cause the helical insertion path created by the kinked bevel-tip.

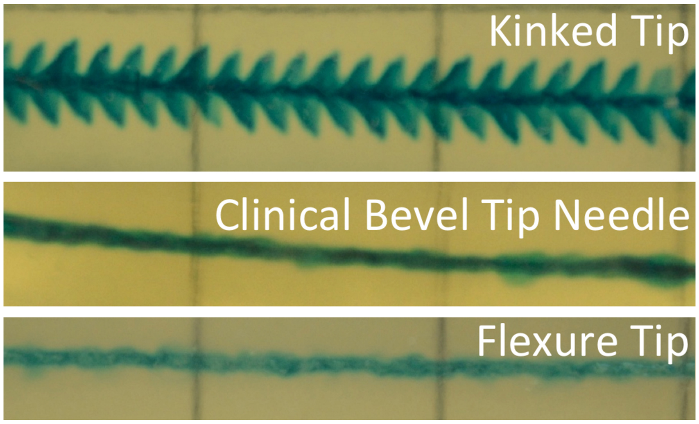

Figure 2.5: Tissue damage comparison of kinked bevel-tip needle, clinical bevel-tip needle, and flexure-tip needle.

2.5 Modeling the Flexure-Tip Needle

In this section, a kinematic model is developed in order to predict the behavior of the flexure and the influence it has on the overall needle trajectory. The kinematics of a flexure-tip needle are modeled with states that represent the needle orientation $R_n \in SO(3)$, the flexure tip pose orientation $R_t \in SO(3)$, and the needle position $\boldsymbol{p_n} \in \mathbb{R}^3$. The matrices, R_n and R_t, are packed as

$$R_n = \begin{bmatrix} \boldsymbol{x_n} & \boldsymbol{y_n} & \boldsymbol{z_n} \end{bmatrix} \qquad R_t = \begin{bmatrix} \boldsymbol{x_t} & \boldsymbol{y_t} & \boldsymbol{z_t} \end{bmatrix} \tag{2.1}$$

and are illustrated in Fig. 2.6.

The differential equation governing the behavior of the flexure-tip system is given by

$$\dot{R}_n = \widehat{\boldsymbol{\omega}}_{\boldsymbol{n}} R_n \tag{2.2}$$

$$\dot{R}_t = \widehat{\boldsymbol{\omega}}_{\boldsymbol{t}} R_t \tag{2.3}$$

$$\dot{\boldsymbol{p}}_{\boldsymbol{n}} = \frac{c_1 \boldsymbol{z_n} + (1 - c_1)\boldsymbol{z_t}}{\|c_1 \boldsymbol{z_n} + (1 - c_1)\boldsymbol{z_t}\|} v \tag{2.4}$$

where $\boldsymbol{\omega_n} \in \mathbb{R}^3$ and $\boldsymbol{\omega_t} \in \mathbb{R}^3$ are the angular velocities of the needle shaft and the flexure tip, respectively, and $\widehat{\ }$ maps $\mathbb{R}^3$ to SO(3) and is a skew-symmetric matrix. The inputs are

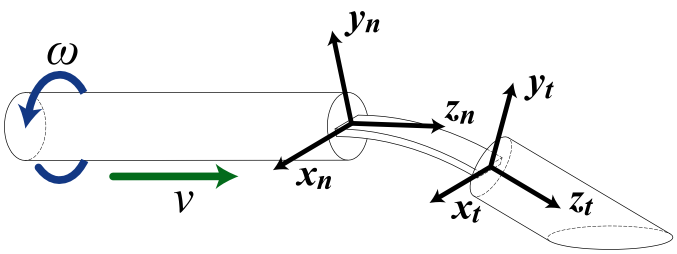

Figure 2.6: The coordinate systems used for the kinematic model. The inputs to the model are the shaft forward velocity v and shaft rotational velocity ω applied to the base of the needle during insertion.

the shaft forward velocity v and shaft rotational velocity ω applied to the base of the needle during insertion. The scalar c_1 incorporates tissue and needle geometry properties (e.g., flexure-tip length) that influence what proportion of the needle base velocity is parallel to the $\boldsymbol{z_n}$ and $\boldsymbol{z_t}$ directions.

We approximate the tissue as a viscous fluid acting on the needle shaft with no friction in the $\boldsymbol{z_n}$ direction and coefficient of friction b in every other direction, so that the needle shaft angular velocity $\boldsymbol{\omega_n}$ is linearly related to a torque $\boldsymbol{\tau_f}$ caused by the flexure tip moving through tissue and the component of the shaft angular velocity in the shaft direction $\boldsymbol{z_n}$ is equal to the shaft rotation velocity ω. The shaft angular velocity is approximated as

$$\boldsymbol{\omega_n} = R_n K_b R_n^{-1} \boldsymbol{\tau_f} + \omega \boldsymbol{z_n}. \tag{2.5}$$

where

$$\boldsymbol{\tau_f} = c_2 \boldsymbol{z_n} \times \boldsymbol{z_t} v. \tag{2.6}$$

The scalar c_2 incorporates tissue and needle properties (e.g., tissue stiffness, flexure length, etc.) and $K_b = \mathrm{diag}(b, b, 1)$.

The flexure tip angular velocity $\boldsymbol{\omega_t}$ is approximated as linearly related to the total torque applied to the flexure through no tissue friction in the tip direction $\boldsymbol{z_t}$ and friction coefficient b in every other direction. The torque acting on the flexure tip consists of a spring-like torque $\boldsymbol{\tau_h}$ applied by the flexure hinge, a torque $\boldsymbol{\tau_b}$ caused by the flexure tip's bevel, an inverted-pendulum-like torque $\boldsymbol{\tau_t}$ caused by the flexure tip's shaft translating through tissue, and a torque $\boldsymbol{\tau_l}$ created when the flexure tip reaches it's bend limit. The flexure tip angular velocity is approximated as

$$\boldsymbol{\omega_t} = R_t K_b R_t^{-1} \left(\boldsymbol{\tau_h} + \boldsymbol{\tau_b} + \boldsymbol{\tau_t} + \boldsymbol{\tau_l}\right) \tag{2.7}$$

where

$$\boldsymbol{\tau_h} = R_t K_{fxy} R_t^{-1} \left(\boldsymbol{z_t} \times \boldsymbol{z_n}\right) + R_t K_{fz} R_t^{-1} \left(\boldsymbol{x_t} \times \boldsymbol{x_n}\right) \tag{2.8}$$

$$\boldsymbol{\tau_b} = c_3 (\boldsymbol{z_n} \cdot \boldsymbol{z_t}) \boldsymbol{x_t} v \tag{2.9}$$

$$\boldsymbol{\tau_t} = c_4 \boldsymbol{z_n} \times \boldsymbol{z_t} v \tag{2.10}$$

$$\boldsymbol{\tau_l} = \frac{c_5 \left(\boldsymbol{z_n} \times \boldsymbol{z_t}\right)}{\|\boldsymbol{z_n} \times \boldsymbol{z_t}\|^2 - \sin^2 \theta_{max}} \tag{2.11}$$

The matrix $K_{fxy} = \mathrm{diag}(k_{fx}, k_{fy}, 0)$ is the flexure-hinge's stiffness matrix packed with the hinge stiffnesses in the $\boldsymbol{x_n}$ and $\boldsymbol{y_n}$ directions, which are denoted by k_{fx} and k_{fy}. $K_{fz} = \mathrm{diag}(0, 0, k_{fz})$ is the flexure-hinge's stiffness matrix in the $\boldsymbol{z_n}$ direction with stiffness k_{fz}. The stiffness matrices K_{fxy} and K_{fz} are diagonal in the needle tip frame.

The scalar c_3 incorporates tissue and geometric properties of the needle (e.g., bevel angle). The torque $\boldsymbol{\tau_t}$ makes the kinematics of the flexure tip very similar to a trailer being pushed in reverse (Fig. 2.7). The scalar c_4 incorporates tissue and is proportional to the length ℓ of the flexure tip. The scalar c_5 is the stiffness of the flexure tip limit. The flexure-limit torque is approximated with a barrier function (2.11) that approaches a vertical asymptote as the bend angle approaches the maximum bend angle $\theta_{\max}$ permitted by the flexure limit.

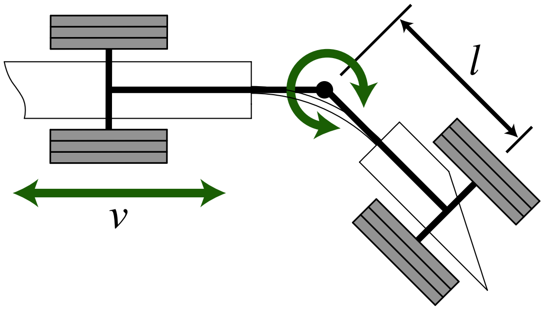

Figure 2.7: When inserted with spatial velocity v only, the behavior of a flexure-tip needle exhibits a "fold-over" effect that can be approximately modeled as a rear-driven trailer of length ℓ.

2.6 Experiments

The flexure-tip needle used to validate the kinematic model presented in Sec. 2.5 is shown in Fig. 2.8(a) and was made from a nitinol tube with an outer diameter (OD) of 1.65 mm and an inner diameter (ID) of 1.35 mm. In order to utilize magnetic tracking sensors inside of the needle to validate the model, a different flexure-tip needle design was used. Rather than using nitinol wires and epoxy to create the flexure joint, in this section the flexure joint was made by cutting out a portion of the nitinol tube with a rectangular cross

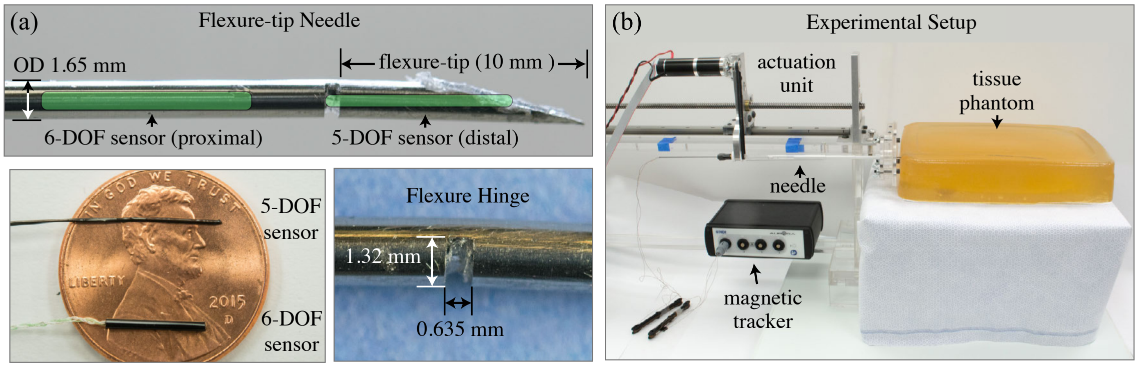

Figure 2.8: (a) The flexure-tip needle used for the experimental model validation is shown. The position of the embedded magnetic tracking sensors in the needle is illustrated, and the sensors are shown overlaid on top of a penny for scale. The flexure hinge is created by cutting out a portion of the nitinol tube near the bevel tip. (b) The experimental setup used for tracking the flexure-tip needle under various insertion trajectories is shown. A robotic actuation unit controlled the insertion and rotation velocity of the needle into a tissue phantom, while a magnetic tracking system recorded the position of the sensors in the needle.

section (width of 0.635 mm and a cut depth of 1.32 mm) using a square end mill (the same approach is described in [77]). The rectangular cutout resulted in a flexure with a maximum bend angle of approximately 32 °. The length of the flexure tip was selected to be 10 mm in order to fit a magnetic tracking sensor in the tip. Two magnetic tracking sensors, a 6-DOF sensor and 5-DOF sensor, were placed on the proximal and distal side of the flexure hinge, respectively. They were positioned in the needle as illustrated by Fig. 2.8(a). Both sensors are shown in the inset of Fig. 2.8(a). A bevel was ground into the flexure tip with an angle of approximately 10 °.

An actuation unit (derived from [14]) was used to rotate and insert the flexure-tip needle into a tissue phantom made from 10% by weight Knox gelatin (Kraft Foods Global Inc., USA). An NDI tabletop field generator (NDI Medical, Ontario, Canada) was used to track both magnetic sensors as the needle was inserted into the tissue phantom. The experimental setup is shown in Fig. 2.8(b).

2.6.1 Kinematic Model Calibration

The flexure-tip model parameters were calibrated by selecting the parameters that minimized the error between a set of actual needle trajectories (with known input insertion and rotation velocities) and the corresponding trajectories predicted by the flexure-tip model. The tissue friction cannot be identified from the other parameters because it always appears in the model equations (2.5)-(2.11) as a ratio with the other parameters, therefore, we identified the other parameters by setting $k_b = 1$. The flexure hinge stiffnesses k_{fy} and k_{fz} tend to be much stiffer than the stiffness k_{fx} and have a small effect on the measured trajectories, making them poorly identifiable from the data. Therefore, we set $k_{fy} = 100k_{fx}$ and $k_{fz} = 300k_{fx}$ and identified only the stiffness k_{fx}. We also found that the data is insensitive to the flexure-angle limit parameter c_5 that determines the flexure-limit stiffness, so we set $c_5 = 0.1$, which tends to match experimental results.

The identifiable parameters are packed in the vector

$$\boldsymbol{\eta} = [c_1 \;\; c_2 \;\; c_3 \;\; c_4 \;\; k_{fx}]^T \tag{2.12}$$

and were found by minimizing the error between a set of actual needle trajectories (with known input insertion and rotation velocities) and the trajectories predicted by the flexure-tip model. The error at time t is computed as

$$\boldsymbol{e}(t, \boldsymbol{u}(t)) = \|\boldsymbol{p_m}(t, \boldsymbol{\eta}, \boldsymbol{u}(t)) - \boldsymbol{p_s}(t, \boldsymbol{u}(t))\|, \tag{2.13}$$

where $\boldsymbol{p_s}$ is the position reported by the proximal magnetic tracker sensor and $\boldsymbol{p_m}$ is the position predicted by the kinematic model with parameters $\boldsymbol{\eta}$, computed by integrating (2.3)-(2.4) using the measured initial conditions obtained from the corresponding experimental trajectory.

The calibrated parameters solve the problem

$$\min_{\boldsymbol{\eta}} \sum_i \|\boldsymbol{e_i}(t, \boldsymbol{u_i}(t))\|^2, \quad \forall t > 0 \tag{2.14}$$

for all valid time, where $\boldsymbol{u_i}(t)$ are the known inputs for each trajectory (delimited by i) used in the calibration. We calibrated the needle parameters using two experimental trajectories with five trials each (i.e., a total of 10 trajectories). The experimental trajectories and their known inputs are presented in the next section. The calibration results are shown in Table 2.1 and the accuracy of the flexure-tip model with the calibrated parameters is analyzed in the next section.

2.6.2 Experimental Results

We evaluated the flexure-tip model presented in Sec. 2.5 by inserting the needle into the tissue phantom using two insertion/rotation-input trajectories. In the first trajectory, the

	Value	Units		Value	Units
c_1	0.49	n/a	k_b	1	1/ (N·m·s)
c_2	14.98	N·s	k_{fx}	1.09	N·m
c_3	401.0	N·s	k_{fy}	109	N·m
c_4	2016.5	N·s	k_{fz}	327	N·m
c_5	0.1	N·m			

Table 2.1: Calibrated flexure-tip model parameters.

needle is inserted at a constant speed of 6.5 mm/s without rotation, while in the second trajectory, the needle is inserted at the same constant speed but is periodically rotated at a rate of 1.1 rad/s for 5 s. Note that due to torsional compliance of the needle tube and tissue friction, torsional wind-up causes the input applied to the flexure tip to not be the same as that applied by the actuation unit. Some work has modeled these effects (e.g., [35, 36]), but for simplicity, we measure the inputs applied at the flexure tip using the 6-DOF proximal magnetic sensor. Due to compliance, friction, and sensor noise, there is uncertainty in the input at the flexure tip. Fig. 2.9(a) shows the mean measured input and one-standard-deviation interval for $n = 5$ trials of both trajectories.

Fig. 2.9(b) shows two views of the average tracked needle's path obtained from the proximal magnetic sensor for $n = 5$ trials for each trajectory. A one-standard-deviation volume, obtained from the position covariance at every time along the path, is also shown. For comparison, the average path and one-standard-deviation volume predicted by the flexure-tip model is also shown for both trajectories with $n = 5$ trials. The predicted flexure-tip model path is computed using the corresponding initial state conditions for each trial. Much of the uncertainty comes from sensor noise and experimental variation in the initial conditions.

For additional comparison, Fig. 2.9(b) also shows the average path (and the one-standard-deviation volume) that would have been followed if we had modeled the flexure-tip needle

Trajectory 1 Trajectory 2

(a) Input velocity measured at the proximal magnetic tracking sensor.

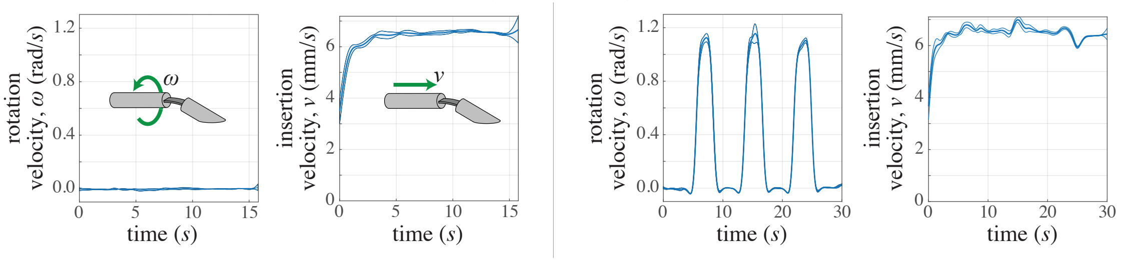

(b) Top and side views of the flexure-tip model, kinked bevel-tip model, and actual trajectories.

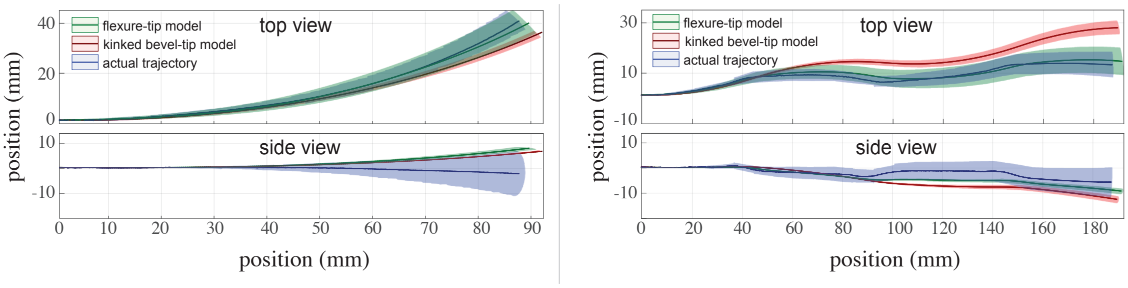

(c) Absolute trajectory position error for flexure-tip and kinked bevel-tip models.

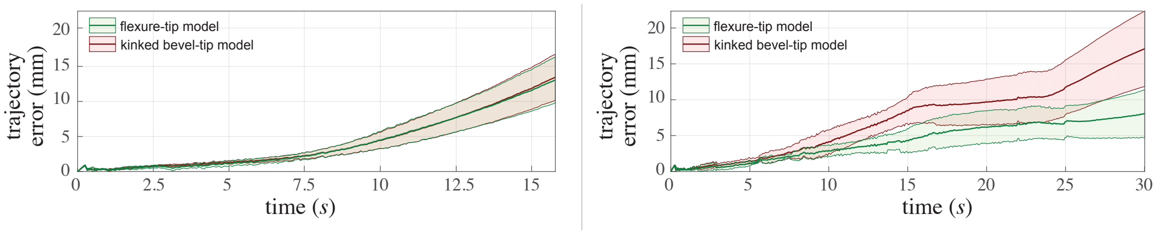

(d) Angle θ between needle body and the flexure tip for flexure-tip model and actual trajectories.

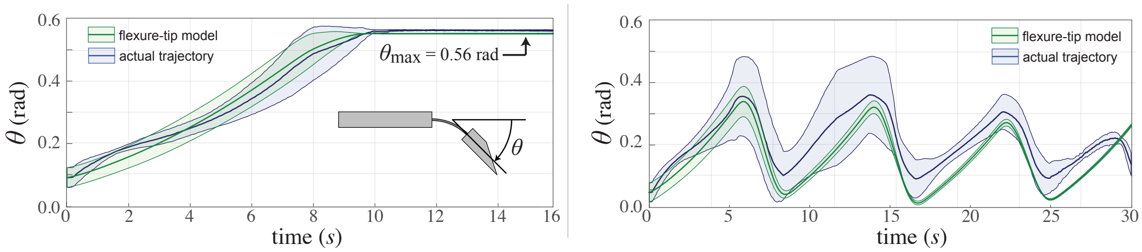

Figure 2.9: Experimental testing of the kinematics for the flexure-tip needle. Trajectory 1 and 2 were each run 5 times, and the mean data is presented here. The shaded areas in the plots represent one standard deviation interval for the data.

as if it were a kinked bevel-tip needle by simplifying the flexure-tip model so that

$$R_t = R_n e^{\theta_{\max} \widehat{\boldsymbol{e_1}}} \tag{2.15}$$

$$\boldsymbol{\omega_t} = \boldsymbol{\omega_n} \tag{2.16}$$

using the same initial conditions for each of the $n = 5$ trials. This simplification was used in [78] and ultimately turns the kinked bevel-tip model into the standard unicycle model [32].

Fig. 2.9(c) shows the average error along with one-standard-deviation interval between the flexure-tip model, the kinked bevel-tip model, and the actual measurements. The error is defined at every time t by (2.13). For the first trajectory (left-hand side of Fig. 2.9(c)), the flexure-tip and kinked bevel-tip models approximate the measured trajectory equally well with an average final error of 12 mm, which corresponds to 11.5% error when normalized by the total insertion depth (104 mm). For the second trajectory (right-hand side of Fig. 2.9(c)), the flexure-tip and kinked bevel-tip models approximate the measured trajectory with final errors of 8 mm and 17 mm that correspond to relative errors of 4.1% and 8.9%, respectively, when normalized by the total insertion depth (190 mm). For this trajectory, the flexure-tip model is substantially more accurate than the kinked bevel-tip model, with an improvement in error of 47.1%.

The distinguishing factor between flexure-tip needles and all other steerable needles is the flexure hinge that can bend continuously until it reaches its hard-stop. Fig. 2.9(d) show the flexure angle θ between the needle axis $\boldsymbol{z_n}$ and the tip axis $\boldsymbol{z_t}$ as a function of time. In the first trajectory shown, the flexure-hinge hits the hard-stop at approximately 9.5 s with a limiting angle of $\theta_{\text{max}} = 0.56$ rad after traveling 61.8 mm. In the second trajectory, the flexure-hinge never reaches its hard-stop. Comparing Figs. 2.9(a) and 2.9(d) shows that the flexure angle increases while the rotation velocity of the needle is held at 0 rad/s and rapidly decreases when the needle is rotated. This effect was observed in [6] and is a unique property of needles with flexure tips. In general, the flexure-tip model follows the same behavior as the actual needle.

In [6], Swaney et al. report that flexure-tip needles tend to straighten their flexure hinge when continuously rotated. This is advantageous as the flexure-tip needle can be steered along a straight path by continuous rotation without substantially damaging tissue.

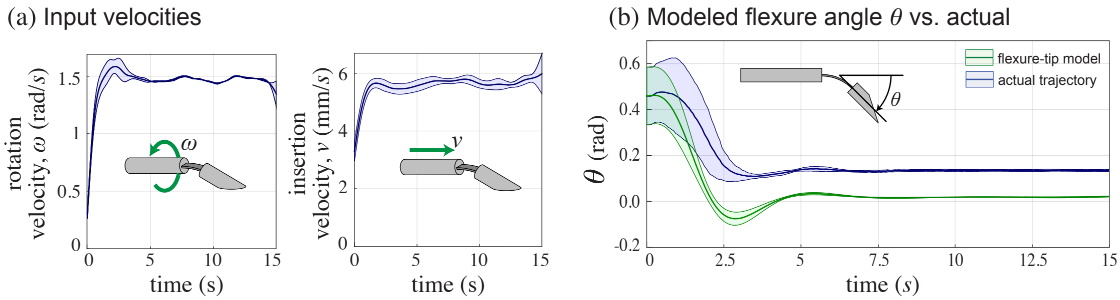

Figure 2.10: When a deflected flexure-tip needle (i.e., the flexure is already bent) is inserted and rotated with constant velocity into tissue, the flexure angle between the tip and the needle shaft decreases toward zero as shown here. This effect enables straight trajectories with reduced tissue damage as described in [6].

Fig. 2.10 demonstrates the flexure-tip needle's tendency to straighten the hinge by plotting the flexure angle when the needle is rotated at a constant target angular velocity of 1.5 rad/s and inserted at a constant velocity of 5.5 mm/s as plotted in Fig. 2.10(a). Fig. 2.10(b) shows that the flexure angle rapidly drops to a steady-state angle of 0.15 rad after 7.5 s. This behavior is also predicted by the flexure-tip model as shown in Fig. 2.10(b). The error between the model and actual approaches a steady state of 0.11 rad after 7.5 s. We expect that some of the steady-state error can be attributed to misalignment of the distal-most sensor inside the flexure tip.

2.7 Discussion

The flexure-tip needle presented in this chapter solves the problem of existing high curvature steerable needles cutting helical paths through tissue during rotation. It also addresses the difficulty with using existing high curvature steerable needles through a coaxial introducer needle. These goals are accomplished through the use of geometry and mechanics to inform the design of the flexure joint. One additional benefit of the flexure-tip design is that the needle curvature can be controlled using duty cycling, which is one possible control strategy for steerable needles. The model developed in this chapter for predicting the behavior of flexure-tip needles provides insight into the kinematics of the needle design, and can be directly applied to existing motion planners [78, 79], potentially improving the accuracy of motion planning results when using the flexure-tip needle as in [61, 79]. The question of when to use the flexure-tip needle model with these motion planners is an interesting one.

Fig. 2.9 shows that a simplified kinked bevel-tip model can predict a flexure-tip needle's actual behavior some of the time (e.g., when inserting the needle with little to no rotation velocity as in the first trajectory). The key contribution of the flexure-tip model presented in Sec. 2.5 is to predict the transient behavior of the flexure tip when the flexure angle is within the hard-stop. We expect that the kinked bevel-tip and flexure-tip models predicted the needle's actual behavior equally well for the first trajectory of Fig. 2.9 because the needle's configuration is within the transient regime for a much smaller amount of time compared to the second trajectory (the flexure angle does not reach the hard-stop limit during the entirety of the second trajectory). Since the flexure-tip model presented in Sec. 2.5 is more complex than the standard unicycle/bicycle models, determining when a simpler model could be used to predict a flexure-tip needle's behavior is an important consideration. This is especially true for motion planning applications where the model is heavily used and complexity matters [78, 79]. In general, a simple model can be used when the flexure-tip needle is expected to spend little time in the transient regime, otherwise the full flexure-tip model will be substantially more accurate.

The kinematic model developed here for the flexure-tip needle provides a good approximation of the behavior of the needle during insertion, although several unmodeled effects likely influence the overall accuracy of the model. For example, the model does not account for buckling of the cutout flexure joint. Buckling of the flexure can change the stiffness of the flexure joint and potentially lead to plastic deformation of the flexure joint, creating a bias in the needle trajectory. However, the use of nitinol wires to create the flexure joint as in Sec. 2.3 will likely remove this unmodeled effect. Manufacturing tolerances, whether the width and depth of the flexure cutout or the alignment and spacing of the nitinol wires used to make the flexure joint, will also affect the trajectory of the needle in tissue. Regardless of the flexure-tip needle design used, there are clinical questions that should also be investigated for the flexure-tip needle.

While we note that initial anecdotal phantom tissue histological images provided in this chapter show little apparent tissue damage when using the flexure-tip needle, more in-depth histological evaluations in living biological tissues are needed to quantitatively verify reduced tissue damage. It will also be useful to verify that the tissue damage incurred by any of these needle tip designs (including the kinked bevel-tip needle) is clinically significant. To adapt this needle to carry specific interventional payloads (e.g., biopsy, therapy delivery, brachytherapy, and others), similar to prior bevel-tip steerable needles, the flexure-tip needle can serve as a guide-wire to the region of interest, with a sheath advanced over the needle after the tip has reached the desired location. This concept is experimentally shown in Sec. 4.7. We hope that the reduced tissue damage of the flexure-tip needle and the ability to use the needle as a guide-wire for accurate targeting will help to facilitate clinical translation of flexible tip-steerable needles sooner rather than later. Toward this end, we have engaged in numerous discussions with medical device companies and are in active discussions with a large medical device company to translate the flexure-tip needle to clinical use. Some results from this commercialization effort are presented below.

We envision that the flexure-tip needle could be deployed by hand in a clinical setting to correct for tip error due to misalignment or deflection of the needle during insertion. Toward clinical adoption and commercialization of the flexure-tip needle, we have built multiple variations of the flexure-tip needle to test the performance of the needles under various conditions and in various tissue mediums. We have built flexure-tip needles with stainless steel hypodermic tubing in place of nitinol for the needle shaft, showing that the stainless steel still provides appreciable curvature with the benefit of reduced cost. We have also built flexure-tip needles with different numbers of nitinol flexure wires, and have even used a thin piece of nitinol strip to make the flexure in order to show how the curvature

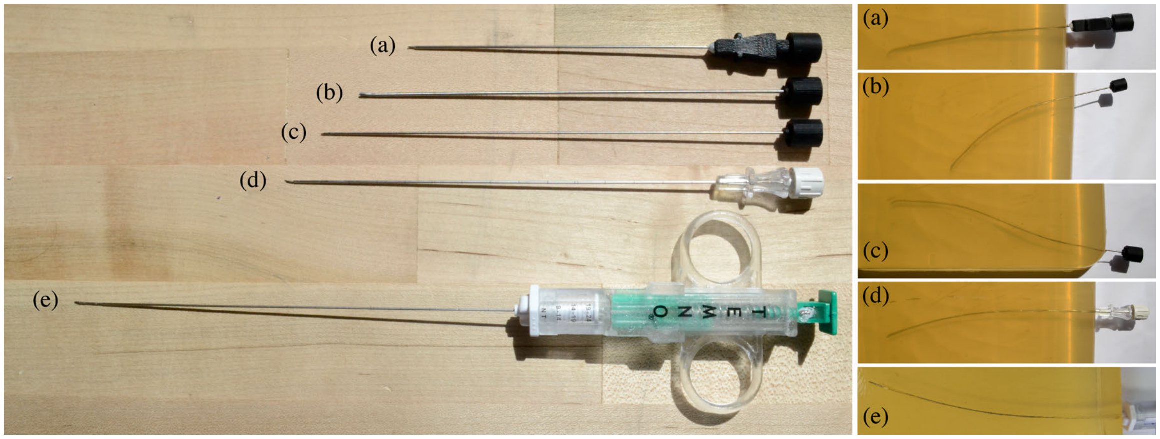

Figure 2.11: Multiple variations of the flexure-tip needle and corresponding insertions into a gelatin phantom. Note that needle paths shown to the right were all achieved by inserting the needle by hand, one of the deployment methods envisioned for clinical use. (a) 19 gauge stainless steel coaxial needle with a 21 gauge flexure-tip stylet. The flexure-tip stylet is made using a nitinol shaft, and three 0.125 mm nitinol wires make up the flexure joint. (b) 18 gauge nitinol shaft flexure-tip needle with a three wire flexure joint. (c) 20 gauge nitinol shaft flexure-tip needle with a two wire flexure joint. (d) 19 gauge stainless steel coaxial needle with a 21 gauge flexure-tip stylet made with a stainless steel shaft and a three wire flexure joint. (e) Flexure-tip incorporated into a clinical core biopsy gun. The flexure-tip is made with a three wire flexure joint.

of the needle can be altered by changing the geometry of the flexure. Lastly, we have integrated the flexure-tip needle into clinical biopsy needle systems. We built a flexure-tip needle that could pass through a coaxial introducer needle, and were able to vary the maximum bend angle of the flexure-tip by changing the length of the needle tip exposed from the introducer needle. This approach may be useful for correcting for misalignment or errors when targeting locations using standard tri-bevel needles that are intended to go straight and cannot steer. We also displayed the ability to steer core biopsy needles by adding a flexure-tip needle onto the end of a core biopsy needle gun. This collection of needles, built to illustrate the clinical application and usefulness of the flexure-tip needle, can be seen in Fig. 2.11.

Chapter 3

Miniature Wrists for Surgical Robots

3.1 Chapter Overview

Existing needle-sized surgical tools have limited tip dexterity due to the small diameter of the tools and rigid tool shafts. Our goal is to create a device that increases the dexterity of needle-sized tools while using a simple actuation scheme and a straightforward method for integration with existing tools. If given the ability to navigate around sharp corners in the anatomy, physicians could perform procedures that are not even attempted today with existing rigid needle-sized tools. This chapter presents a miniature wrist that can be integrated into needle-sized surgical instruments and provides dexterity to the tip of needle-sized surgical tools. The wrist consists of a nitinol tube with asymmetric cutouts that is actuated by a single tendon to provide significant distal curvature. We derive and experimentally validate kinematic and static models for the wrist, and describe several prototype wrists, illustrating the straightforward fabrication and scalability of the design. We also experimentally investigate fatigue life and the concept of tip-first bending. The work described in this Chapter is in review in the ASME Journal of Medical Devices [58] and was presented at the International Conference on Robotics and Automation in 2015 [77]. We have also filed a patent application for the wrist design.

3.2 Introduction

Minimally invasive surgery is constantly being redefined by surgeons and engineers as surgical devices continue to decrease in size. With smaller devices come benefits such as reduced scarring and patient pain, and needle-sized devices have even been used to perform near scarless procedures [80] and present exciting opportunities for use in the pediatric population [81]. However, as the diameter of these devices decrease, it becomes increasingly difficult to create dexterous surgical instruments. Consequently, existing needle-sized devices have a limited number of degrees of freedom, preventing them from turning sharp corners in the anatomy as would be encountered at the skull base [82], in the middle ear [83], and in the ankle [84]. Additionally, the lack of a wrist on needle-sized devices greatly limits the ability of surgeons to perform other dexterous tasks, such as suturing and tissue resection. Lastly, the small size of the tools make it difficult to use complex mechanisms or actuation schemes in the tool design. Therefore, the goal of this work is to create a device that provides additional degrees of freedom and dexterity to needle-sized surgical tools while employing a simple actuation scheme and straightforward integration with existing needle-sized tools.

There have been a number of different wrist designs presented in the literature, including designs based on traditional mechanical linkages such as ball joints [85], universal joints [86], cables and pulleys [87, 88, 89], lead screws [90, 91], serial chains in parallel [92], and flexures [8, 93]. The outer diameter of these designs range from 2.4 to 15 mm. While it may be possible to downscale each of these designs to some extent, continuum structures are often more easily miniaturized than mechanical linkages.

Multiple forms of continuum wrists and dexterous structures have also been designed, including a unique cable-ring design [9], a rolling variable neutral-line mechanism [94], interlocking fiber designs [31, 95], a flexible multi-backbone design [40], a compliant rolling-contact design [96], and a flexible tubular nitinol structure [41], among others. For a thorough review of joints used in existing bendable surgical instruments, see [38]. In general, designs with fewer components have shown better scalability, and thus designs that involve machining the wrist into the shaft of the manipulator itself are appealing.

Manufacturing a region of compliant bending in nitinol tubing has been investigated by several groups. Kutzer et al. created a 6-mm tool for arthroscopy that used rectangular, symmetric cutouts [45]. Wei et al. used triangular cuts that were made in nitinol tube to create a similar manipulator [97]. A 10-mm tool used for endoscopic camera steering was developed by Fischer et al. [10]. Various finite element analyses were undertaken by several groups to aid the design of compliant bending regions in nitinol tubes [98, 99, 100]. Catheters with bendable nitinol tips were made by both Haga et al. and Bell et al. [46, 47], and a steerable needle tip was created using a machined nitinol tube by Ryu et al. [101].

In this work, we have created a miniature wrist for needle-sized surgical instruments that is made using asymmetric, rectangular cutouts in a nitinol tube, forming a compliant bending region that is actuated with a single tendon. The wrist can be outfitted with various surgical end effectors for delivering treatment in tight spaces (see Fig. 3.1). Our wrist most closely resembles the catheter and needle designs of [46, 47, 101], but operates by a simpler principle and can bend more tightly. Our wrist is straightforward to manufacture and does not employ the intricate spring cutout design nor hydraulic actuation of the active catheter of [46], it is small enough for use on needle-sized devices and does not require a nitinol restoring spring like the active catheter design of [47], and it is able to achieve a larger deflection over a smaller radius of curvature compared with the active needle design of [101]. Our wrist is actuated with a single tendon and can be prototyped using inexpensive manufacturing methods. The design is scalable, and most importantly, the wrist can be easily integrated into needle-sized surgical tools. One example of such a tool is the concentric tube robot.

Concentric tube robots are needle-sized robotic manipulators that are comprised of a series of precurved, superelastic nitinol tubes, often less than 2 mm in diameter, that are often designed for medical applications [102]. The tubes are independently translated and rotated with respect to one another, creating a controllable tentacle-like motion of the manipulator. Mechanics-based models of concentric tube robots have been derived [103, 104], and these devices have been investigated for use in prostate removal [105], cardiac applications [106], endonasal skull base surgery [107], and prostate brachytherapy [108]. Providing needle-sized instruments such as the concentric tube robot with a wrist may enable new surgical approaches and techniques that are currently impossible with existing rigid needle-sized

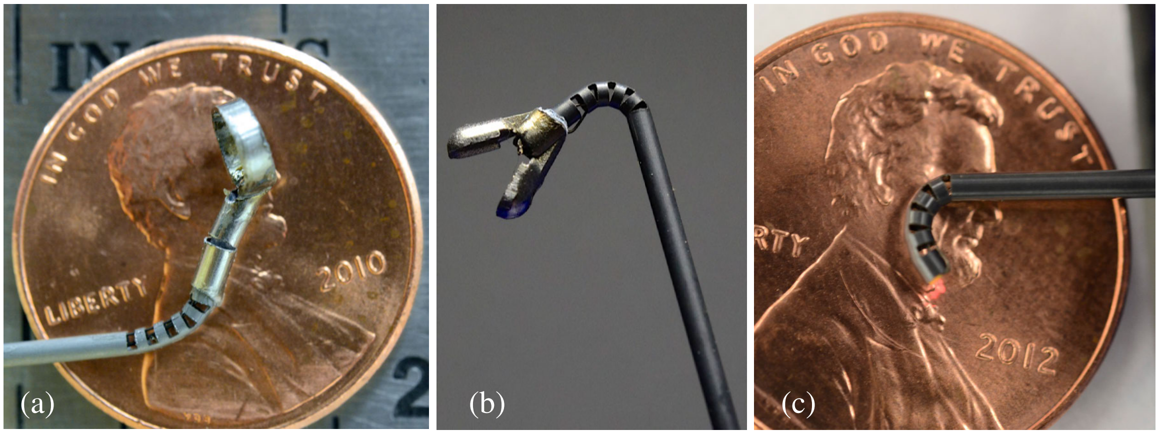

Figure 3.1: Our wrist can be outfitted with various surgical tools. (a) A curette is attached to the end of the wrist and is affixed to a wire that runs the length of the tube, allowing for rotation of the curette. (b) A gripper is shown attached to the wrist. Note that this gripper was modified from a commercial biopsy tool and is unactuated, but is shown here for illustrative purposes. (c) A laser fiber is deployed through the wrist, illustrating the use of the wrist to aim a laser.

tools.

The contributions of this chapter include the derivation and validation of kinematic and statics models for asymmetric cutout wrists, a low-cost manufacturing process, a design method to achieve preferential bending of the wrist, and experimental validation of the fatigue life and scalability of the wrist. A preliminary version of some results in this manuscript can be found in [77]. Additions and enhancements in this archival manuscript include model validation using a scaled micro-wrist, a method for designing the wrist geometry to achieve tip-first bending of the wrist, a new tendon-attachment design, and fatigue testing of the wrist.

3.3 Design Concept

The wrist is composed of a series of asymmetric cuts made into a nitinol tube (see Fig. 3.1). The cutouts selectively modify the bending stiffness along the tube tip and enable actuation of the wrist using a single tendon. While symmetric cutouts have been investigated in a variety of devices [10, 45, 98], the asymmetric cutout geometry offers several advantages over the symmetric cutout design (Fig. 3.2). Using an asymmetric cutout cre-

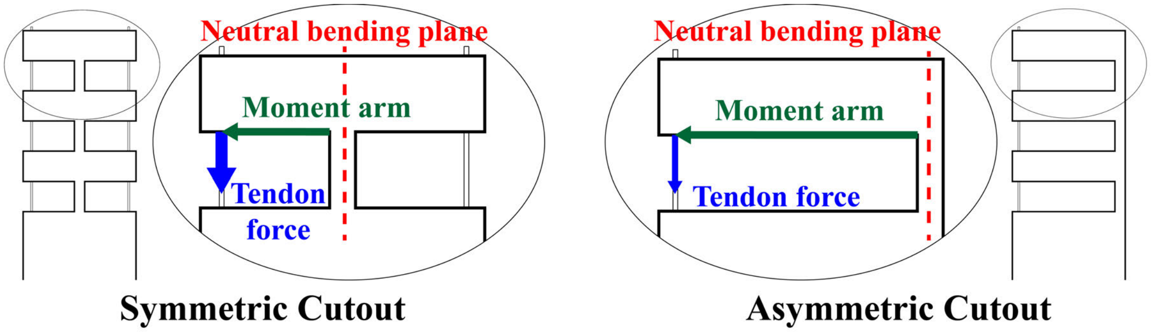

Figure 3.2: The difference between a symmetric cutout design (left) and an asymmetric design (right) is shown. Note the significantly longer moment arm and reduced tendon force required to actuate the asymmetric design.

ates a larger moment arm between the tendon and the neutral bending plane, resulting in a lower actuation force requirement. Additionally, actuation of the asymmetric design requires only one tendon, simplifying the tendon routing compared with symmetric designs and improving scalability of the design. Lastly, the offset neutral bending plane of the asymmetric design results in a tighter radius of curvature about the centerline of the wrist. While the asymmetric design can only bend in one direction, this is not a major concern so long as the entire device can be rotated.

Another key feature of our miniature wrist is the ease of integration with needle-sized tools, which is achieved by machining the wrist directly into the needle shaft itself. This prevents the need to affix the wrist onto the end of a millimeter scale tube using adhesives or other mechanical fasteners. Other wrist designs require a connection between the wrist and the tool shaft (see [90, 93], among others), which could ultimately prove problematic at the millimeter scale, where there is often insufficient surface area for adhesives and mechanical fasteners are not available.

3.4 Kinematic Model

To model the kinematics of the wrist, we first consider a single cutout. We assume that all bending takes place in the cutout sections, and that these sections deform in circular

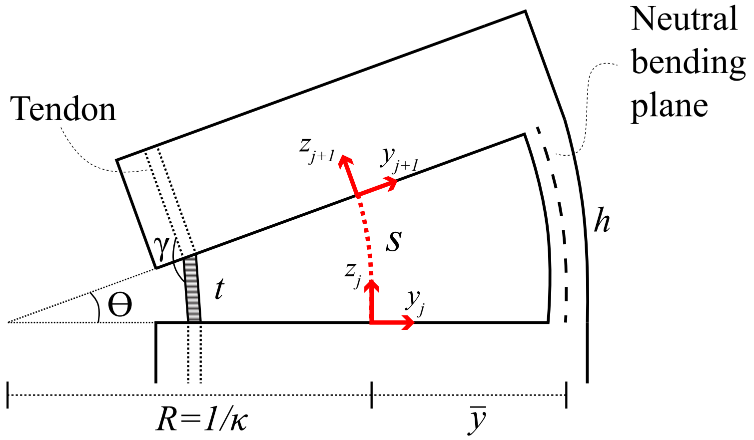

Figure 3.3: Arc parameters and relevant kinematic values for a single cutout are shown. Cut height is denoted by h while the chord, t, followed by the tendon is equal to $h-\Delta l$, where Δl is the tendon displacement. The angle γ defines the angle the tendon must navigate at each corner and is used to calculate the friction on the tendon in Section 3.5.

arcs. Following [109], we map tendon displacement (actuator space) to arc parameters (configuration space), and then we map arc parameters to task space. The arc parameters we seek are curvature (κ) and arc length (s), as shown in Fig. 3.3, and we begin by finding the neutral bending plane of the cutout.

The neutral bending plane is the region of a member that experiences no longitudinal strain during bending. For our wrist, the neutral bending plane, $\bar{y}$, intersects the centroids of the axial cross sections of the cutout portions of the tube (see section view A-A in Fig. 3.4). The location of the neutral bending plane, $\bar{y}$, in the cutout portion of the wrist largely determines the actuator space to configuration space mapping of the wrist. Its location is dependent on the depth of cut g and the inner and outer radii of the tube (r_i and r_o shown in Fig. 3.4) and is given by:

$$\bar{y} = \frac{\bar{y}_o A_o - \bar{y}_i A_i}{A_o - A_i} \tag{3.1}$$

where A_o and A_i are the areas defined in Figure 3.4, $\bar{y}_o$ and $\bar{y}_i$ are their respective centroids,

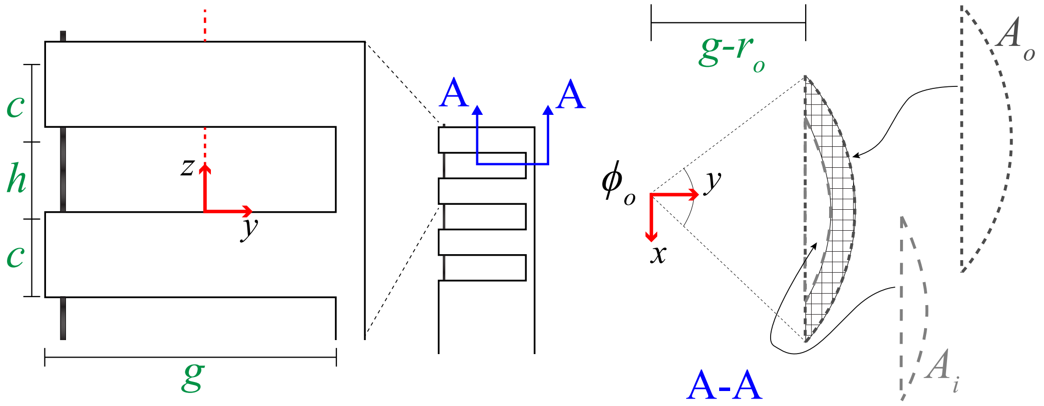

Figure 3.4: The geometric parameters that the designer is free to choose include the uncut section height c, the cutout height h, the cut depth g, and the outer and inner tube radius r_o and r_i. Section view A-A illustrates the areas A_i and A_o used to calculate the neutral bending plane location.

and the angles ϕ_o and ϕ_i are the central angles of areas A_o and A_i. They are given by:

$$\begin{aligned} \bar{y}_o &= \frac{4r_o \sin^3(\frac{1}{2}\phi_o)}{3(\phi_o - \sin\phi_o)} & \bar{y}_i &= \frac{4r_i \sin^3(\frac{1}{2}\phi_i)}{3(\phi_i - \sin\phi_i)} \\ A_o &= \frac{r_o^2(\phi_o - \sin(\phi_o))}{2} & A_i &= \frac{r_i^2(\phi_i - \sin(\phi_i))}{2} \\ \phi_o &= 2\arccos((g-r_o)/r_o) & \phi_i &= 2\arccos((g-r_o)/r_i) \end{aligned} \tag{3.2}$$

which are valid for cuts that are at least as deep as the outer radius of the tube.

The mapping from curvature to tendon displacement Δl can now be found using $\bar{y}$, the chord function, and arc geometry (see Fig. 3.3):

$$\begin{gathered} \Delta l = h - t \\ \Delta l = h - 2\left(\frac{1}{\kappa} - r_i\right)\sin\left(\frac{\kappa h}{2(1+\bar{y}\kappa)}\right) \end{gathered} \tag{3.3}$$

Since we want the mapping of tendon displacement to curvature, we need to invert (3.3). Since it has no analytic inverse, numerical techniques can be used, or, for small angles, we can use a first-order approximation to yield κ, and then solve for the arc s:

$$\kappa \approx \frac{\Delta l}{h(r_i + \bar{y}) - \Delta l\,\bar{y}} \tag{3.4}$$

$$s = \frac{h}{1 + \bar{y}\kappa} \tag{3.5}$$

Once the arc parameters κ and s are known, the homogeneous transformation between frames j and $j+1$ (as defined in Fig. 3.3) can be found using:

$$T_j^{j+1} = \begin{bmatrix} 1 & 0 & 0 & 0 \\ 0 & \cos(\kappa s) & -\sin(\kappa s) & (\cos(\kappa s) - 1)/\kappa \\ 0 & \sin(\kappa s) & \cos(\kappa s) & \sin(\kappa s)/\kappa \\ 0 & 0 & 0 & 1 \end{bmatrix} \tag{3.6}$$

Due to the rectangular cutout geometry of the wrist, the kinematic transformation from the base of the wrist to the tip is obtained by repeatedly applying the transformation (3.6) in conjunction with translations along the z_{j+1} axis to account for the uncut portions of the wrist that do not bend. In addition, the angle of rotation of each section can be found explicitly as:

$$\theta_j(\kappa) = \left(\frac{h}{1 + \bar{y}\kappa}\right)\kappa \tag{3.7}$$

And thus the maximum angle of rotation for a single cutout is given by:

$$\theta_{j,max} = \theta_j(1/r_o) = \frac{h}{r_o + \bar{y}} \tag{3.8}$$

Two important wrist characteristics, maximum bending angle and minimum radius of curvature (an approximation of a circular arc passing through the fully deflected wrist), as shown in Fig. 3.5, can be calculated as:

$$\theta_{max} = \sum_{j=0}^{n} \theta_{j,max} = n\frac{h}{r_o + \bar{y}} \tag{3.9}$$

$$\rho_{min} \approx r_o + \frac{(n-1)c}{\theta_{max}} \tag{3.10}$$

The wrist kinematics are experimentally validated in Section 3.6.2.

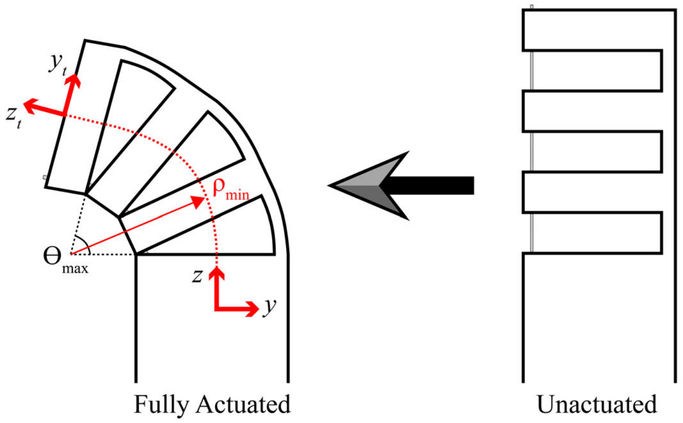

Figure 3.5: Wrist schematic showing wrist going from unactuated to fully actuated with kinematic frames defined. The maximum bending angle and minimum radius of curvature are both labeled.

3.5 Statics Model

In order to model the static behavior of the wrist, we begin by looking at the strain in the deformed, cutout sections. Based on the constant curvature assumption, strain along the length of the wrist varies in a cross section of the portion of the tube in bending according to:

$$\varepsilon(y,\kappa) = \frac{\kappa(y-\bar{y})}{1+\bar{y}\kappa} \tag{3.11}$$

and thus is linearly distributed about the neutral bending plane. This assumed relationship between the geometry and the material deformation allows for a simple computation of the strain energy, after which we use Castigliano's first theorem to determine the reaction force at the tendon. In general, the behavior of nitinol under applied stresses is complex and highly nonlinear, and depends on thermomechanical history [110]. In this work we assume a simplified material model that represents the stress-strain behavior of nitinol as a piecewise linear stress-strain curve, so that the stress may be written as a function of strain as:

$$\sigma(\varepsilon) = \begin{cases} \sigma_{lp} & \varepsilon < \sigma_{lp}/E \\ E\varepsilon & \sigma_{lp}/E \leq \varepsilon \leq \sigma_{up}/E \\ \sigma_{up} & \varepsilon > \sigma_{up}/E \end{cases} \tag{3.12}$$

where σ_{lp} is the lower plateau stress (corresponding to compression), σ_{up} is the upper plateau stress (corresponding to tension), and E is Young's modulus. Since we are modeling the material deformation as one-dimensional stretching and compression of axial fibers, the strain energy density is the area under the stress-strain curve, given by the integral:

$$W(\varepsilon) = \int_0^{\varepsilon} \sigma(e)\, de \tag{3.13}$$

The total strain energy stored in the wrist as a function of the curvature κ of a single cutout is given by:

$$U(\kappa) = n \int_{V_c} W(\varepsilon(y,\kappa))\, dV \tag{3.14}$$

where V_c is the volume defined by the "Top View Cut" cross section of Fig. 3.4 and cutout height h. We use Castigliano's first theorem to find the relationship between rotation θ of the wrist and force F applied by the tendon to the wrist tip:

$$\frac{\partial U(\kappa)}{\partial \theta} = M = FL \tag{3.15}$$

where L is the moment arm length and $\theta = ns\kappa$. When the tendon is looped around the top flexure as shown in Fig. 3.4, the moment arm has length $L = \left(\frac{r_o + r_i}{2}\right) + \bar{y}$.

Due to friction, the force the tendon applies to the tip of the wrist will be less than the actuator force applied to the tendon. Friction between the tendon and the tube wall becomes increasingly significant as cut height and angle of bending increase. To model this effect, we first find the angle γ (shown in Fig. 3.3) that the tendon is required to navigate at a single corner of a cutout section at a given angle of deflection. We assume that the friction that occurs at these corners dominates friction elsewhere along the tendon path. Writing the static balance equations for a single corner, with μ_s as the static friction coefficient, we find that:

$$F = \eta F_{\text{tendon}} = \frac{\sin(\gamma/2) - \mu_s \cos(\gamma/2)}{\sin(\gamma/2) + \mu_s \cos(\gamma/2)} F_{\text{tendon}} \tag{3.16}$$

where $\eta < 1$ accounts for the force lost due to friction at a corner. We can substitute (3.16) into (3.15) to yield:

$$F_{\text{tendon}} = \frac{1}{\eta^{2n} L} \frac{\partial U(\kappa)}{\partial \theta} \tag{3.17}$$

where $2n$ is included to account for the two corners encountered at each cutout. This expression can be evaluated numerically using a finite difference method to relate F_{tendon} and θ. This statics model is experimentally validated in Section 3.6.2.

3.6 Wrist Fabrication and Testing

For the prototype shown in Fig. 3.6, a nitinol tube with an outer diameter (OD) of 1.16 mm and an inner diameter (ID) of 0.86 mm was used. The cut depth selected for this prototype was $g = 0.965$ mm, which corresponds to a maximum outer-fiber strain of approximately 10.4% [1]. We selected a cut height of $h = 0.51$ mm, spacing between cuts of $c = 0.51$ mm, and $n = 5$ cuts in order to achieve at least 90° of bending. These choices resulted in a wrist with a maximum angle of rotation θ_{max} of 138 ° and a minimum radius of curvature ρ_{min} of 1.42 mm. This wrist was used to validate the kinematic and statics models below, and the wrist was fabricated using a computer numerical control (CNC) milling process.

To create the wrist using CNC milling we first make a fixture (Fig. 3.7) by machining a slot into an aluminum block. The slot width and depth equaled the OD of the nitinol tube. We used a MicroProto Systems MicroMill 2000 CNC mill (a small, relatively low-

---

[1] Note that this is slightly higher than the 8-10% recoverable strain typically quoted for nitinol, but that we have found it to work well in practice, since only a small amount of the material at the outermost edge of the wrist undergoes this strain, and then only at maximum articulation.

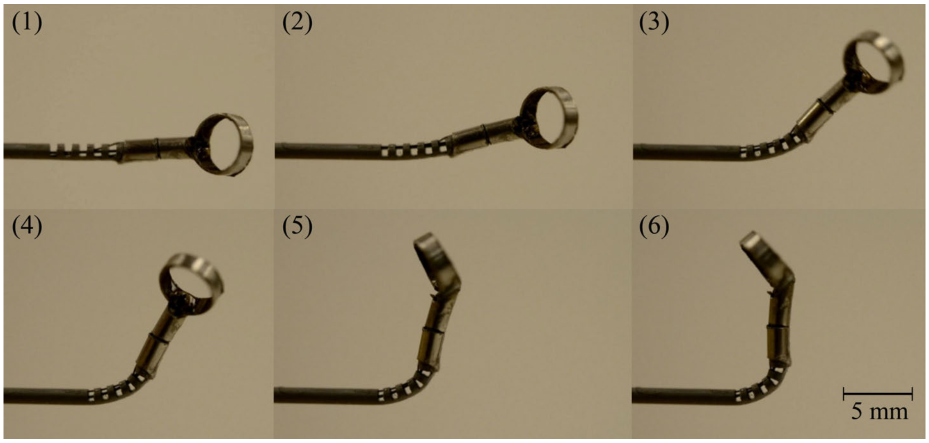

Figure 3.6: A wrist with a curette at the tip is shown bending from 0 to 90°. The sequence order is in the top left of each image. Note that the curette is also being rotated while the wrist is actuated.

cost tabletop CNC) to end mill the slot. The nitinol tube was attached to the fixture using cyanoacrylate adhesive. After creating the fixture, the cutouts in the nitinol tube were machined with the same CNC machine and aluminum titanium nitride coated, two flute, carbide, long flute square end mills. An example of a wrist made with this process can be seen in Fig. 3.6 and a detailed view of the wrist (after removal of the chips) showing the surface finish can be seen in Fig. 3.8(a).

We also fabricated wrists with wire electrical discharge machining (EDM) that are nearly identical to the CNC wrists, with the main exception being the rounded corners found on the wire EDM wrist cutouts (see Fig. 3.8(b)). These rounded corners are created by the wire that makes the cutouts, and the radius of these rounded corners is determined by the diameter of EDM wire used. From a basic strength of materials standpoint, the rounded corners should result in lower stress concentrations during actuation in comparison to the square cutout design. However, the heat of the wire EDM process may induce unwanted material characteristics into the wrist. A comparison of the fatigue life for the CNC wrist and the wire EDM wrist is performed in Section 3.6.3.

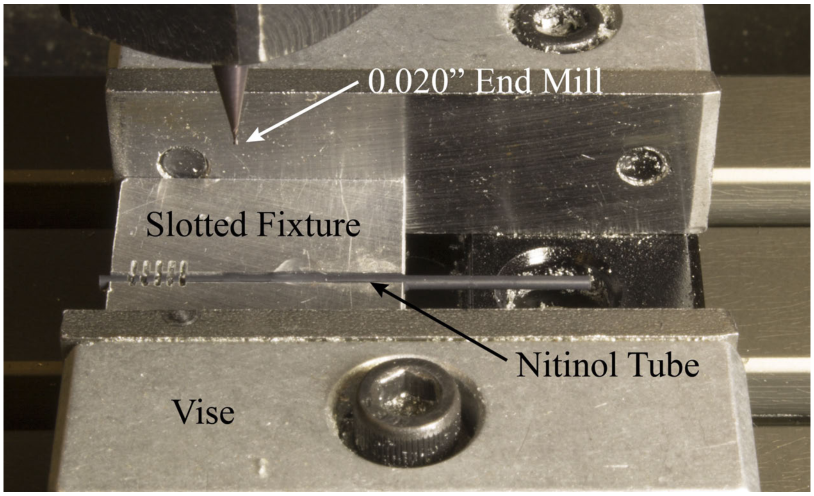

Figure 3.7: The fixturing setup used for the CNC manufacturing process. The slotted aluminum fixture used to make the wrists, with a nitinol tube glued into the fixture, is held in place by the CNC vise.

3.6.1 Tendon Attachment Methods

Actuation of the wrist is performed with a single tendon, and we have explored several tendon attachment methods to rigidly hold the tendon at the tip of the wrist. First, the tendon was looped around the tip of the wrist and passed through the most distal cutout and back to the base of the wrist [77]. A knot at the end of the tendon wire was also used (see Fig. 3.13). The method used for the work presented here was to secure the tendon to an end cap that was located at the tip of the wrist (see Fig. 3.9). The end cap has two

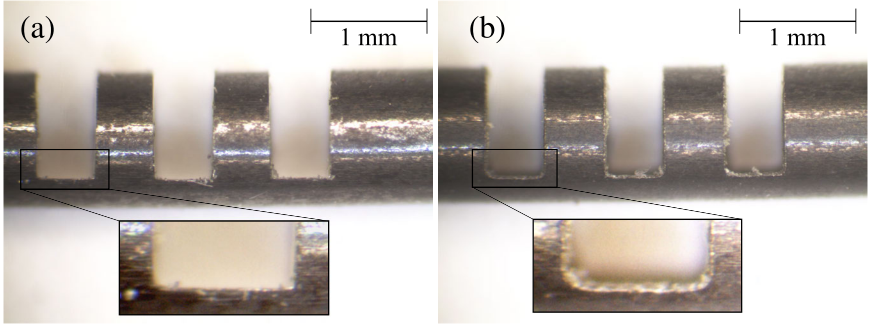

Figure 3.8: (a) Shown is a detailed view of the wrist manufactured using the low-cost CNC milling method. Note the square corners of the cutout made by the square end mill. (b) This wrist was manufactured using wire EDM, and the rounded corners caused by the wire can be seen clearly in the inset.

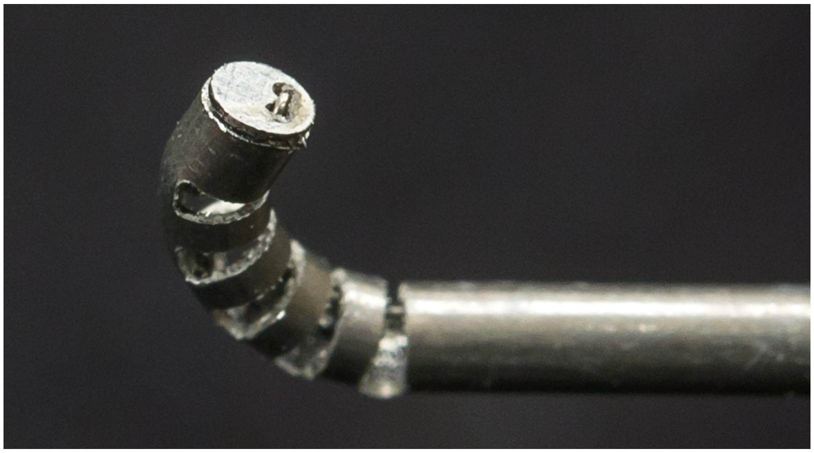

Figure 3.9: The use of an end cap to attach the tendon to the tip of the wrist is shown. This is the tendon attachment method used in this work.

holes in it, located at the outer wall of the tube, and the tendon is looped through one hole and back through the other before being terminated in the tip of the wrist. This sharp bend in the tendon plus the friction between the tendon and the end cap rigidly hold the tendon in place. This method helps to reduce the frictional effects on the tendon, ultimately lowering the actuation forces required to articulate the wrist compared with the looping tendon attachment method [77]. It also results in full articulation of the wrist, since none of the cutouts are held open by the looped wire as in [77]. Lastly, the use of a single tendon increases the available space inside the tube for additional wires to actuate an end effector or perform a task.

3.6.2 Model Validation

We performed an experiment to explore the accuracy of both the kinematic (3.6) and statics (3.17) relationship concurrently. A linear slide (Velmex A2512Q2-S2.5) with 0.01 mm resolution was used to displace the tendon and a force sensor (ATI Nano 17) with 3.125 mN resolution measured the force required to actuate the wrist. The force sensor was mounted to the linear slide, and a collet holder attached to the end of the slide held the wrist. An acrylic plate was mounted to the front of the force sensor, and the tendon was fixed to

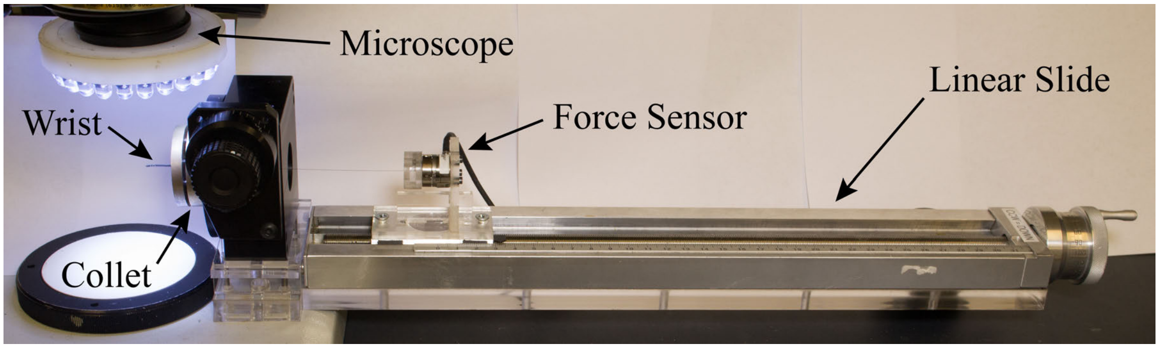

Figure 3.10: The experimental setup used for the kinematics and statics experiment is shown. The wrist was placed directly below a microscope and was held in place using a collet. The tendon was then affixed to a force sensor that was mounted to a linear slide. This allowed for simultaneous collection of force and displacement data.

this plate. The tendon was fixed at the end of the wrist using the end cap. The wrist was deflected by increments of 0.2 mm in tendon displacement, and a microscope with camera attachment captured an image of the deflected wrist at each point (see Fig. 3.10). Each image was processed manually in order to determine the tip position of the wrist, and comparison with the kinematic model is shown in Fig. 3.11.

The experimental comparison with the statics model is shown in Fig. 3.12. For the material properties, note that nitinol has an asymmetric stress strain relationship in tension and compression. We assume plateau stresses of $\sigma_{lp} = -750\,\text{MPa}$ and $\sigma_{up} = 500\,\text{MPa}$ and a Young's modulus of $E = 60\,\text{GPa}$, which fall within ranges reported by the manufacturer and in the literature [110, 111]. A coefficient of friction of 0.2 was selected to account for the frictional losses experienced by the tendon when passing over the sharp corners of the cutouts. Using a sensitivity analysis, it was determined that the statics model is most sensitive to the cut depth, with a 1% change in the cut depth resulting in an over 11% change in the required actuation force. Conversely, a 1% change to Young's modulus, the plateau stresses, and the coefficient of friction each resulted in less than a 1% change in the required actuation force. Due to the sensitivity of the model to cut depth and uncertainty in machining tolerances, we fit the cut depth to the model. The fitted cut depth used for the model shown in Fig. 3.12 is 0.988 mm, which provided the best agreement with the

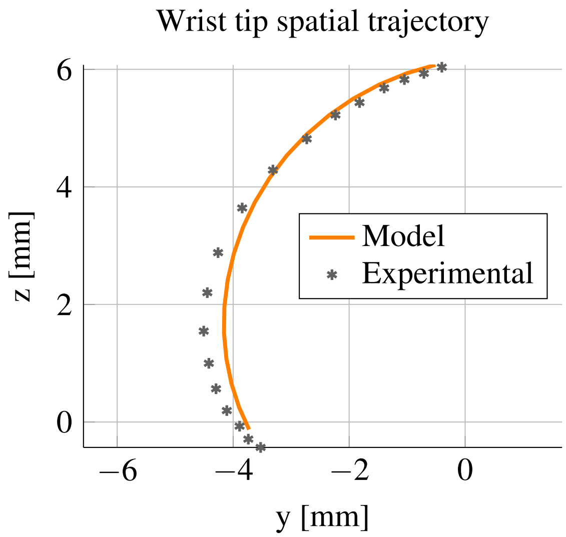

Figure 3.11: The kinematic model predicted and experimental wrist tip spatial trajectory is shown. The wrist starts at top of the figure and rotates counterclockwise from 0 to 140°. These results show that the constant curvature assumption is a reasonable approximation for this geometry, since the wrist tip closely follows the path predicted by the model. It also validates the predicted maximum angle of rotation (138 °) of the wrist.

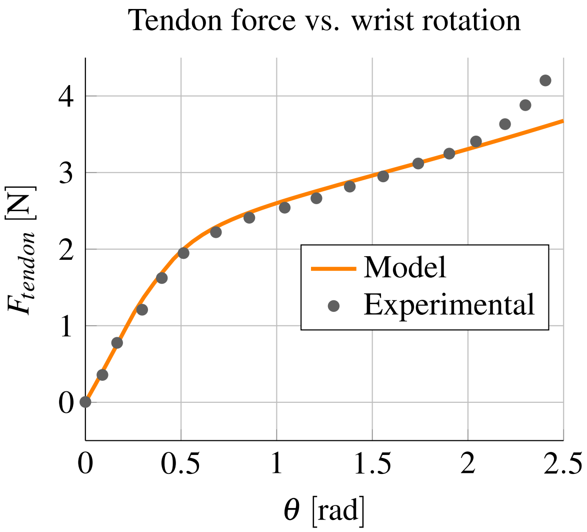

Figure 3.12: The statics model predicted and experimental results shown here correspond to the tendon force required to actuate the wrist. Note that the model captures the superelastic material behavior, as seen by the change in slope at about $\theta = 0.5$ rad.

experimental data. Note that the superelastic, nonlinear behavior of the material is clearly captured by the model. The tail at the end of the experimental data likely corresponds to elastic deformation of the portion of the nitinol tube that has transformed into martensite

[112], which is not captured by the model.

3.6.3 Fatigue Test

We performed an experiment to test the fatigue life of the wrist to ensure that the design would be safe for use in surgical applications, where the wrist may be deflected hundreds of times during a procedure. In order to test the fatigue life, we built a motorized setup that would repeatedly actuate the wrist between 0 and 90 ° of bending while simultaneously measuring the actuation force of the tendon in order to determine when the wrist broke. The CNC wrist failed after a total of 8397 cycles, while the wire EDM wrist failed after a total of 8121 cycles. We also fatigue tested the CNC tip-first bending wrist described in Section 3.7.2, which broke after 5858 cycles (note that the cutout geometry of this wrist resulted in a maximum articulation angle of 84°). Given that the wrist is intended to be used as a disposable or limited use instrument (similar to the da Vinci tools), the number of cycles to failure is more than adequate to provide a reasonable factor of safety.

3.7 Scalability and Tip-First Bending

Two benefits of the wrist design presented in this work are the ease with which it can be scaled down due to the limited number of mechanical components and simple actuation scheme, and the ability to selectively alter the stiffness of the device along its length.

3.7.1 Scalability of Wrist

By creating the wrist from a single nitinol tube and actuating the wrist with a single tendon, it can theoretically be scaled down to the smallest diameter nitinol tube available (0.178 mm as of this writing [113]). One surgical application for such a small wristed tool is retinal surgery, where the tools used are often less than 0.5 mm in diameter [114]. The physicians often must choose between straight and pre-bent tools for retinal surgery, and

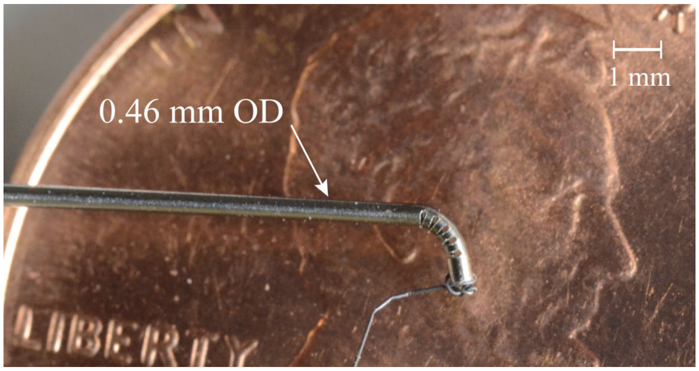

Figure 3.13: A 0.46 mm OD wrist was made using wire EDM manufacturing, and is shown being deflected to approximately 90°. It is overlaid here on a penny to provide a sense of scale. For this photograph, the tendon was tied at the end of the wrist since the end caps made for the 1.16 mm wrist prototype were much larger than the 0.46 mm tube.

thus the ability to selectively deflect the tool would be beneficial. To validate the scalability of our design, we manufactured a micro-wrist from a 0.46 mm OD, 0.28 mm ID nitinol tube using wire EDM machining (see Fig. 3.13). The wrist was designed using 5 cutouts with a 0.33 mm depth of cut, a 0.15 mm cut height, and a 0.15 mm spacing between cuts. We experimentally tested the wrist using the same procedure as described in Section 3.6.2 and compared the motion of the wrist and the force required to actuate it with the models of (3.6) and (3.17). The nitinol properties used were the same as in Section 3.6.2, and the depth of cut was again fit to the data to provide the best agreement. The experimental results can be seen in Figs. 3.14 and 3.15, and indicate that our model can be used for varying wrist geometries.

3.7.2 Tip-First Bending of the Wrist

The ability to bend the tip section first is often desirable when space is limited, as it allows for the tightest radius of curvature for each bending angle. This motion, in which the most distal cutout bends first, followed by the next most distal cutout, and so on, is opposite to the performance of most other tendon-actuated devices, such as steerable catheters. With our wrist, we are able to create tip-first bending by varying the cut height of each cutout

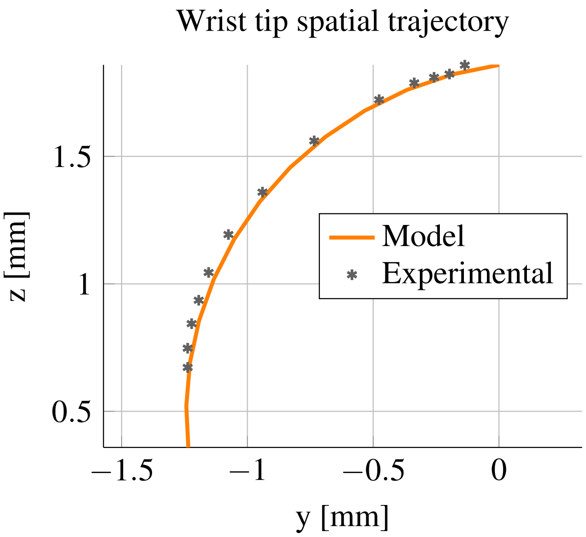

Figure 3.14: The kinematic model is validated for the sub-millimetric wrist (0.46 mm OD). These results again indicate that the constant curvature assumption is a reasonable approximation. Close inspection of the wrist at high articulation reveals that the small cutouts are not closing fully, preventing the wrist from reaching the full articulation predicted by the model.

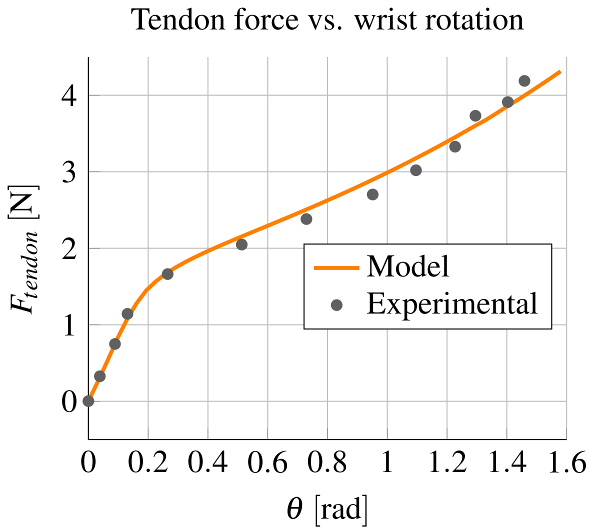

Figure 3.15: The statics model is also validated for the sub-millimetric wrist (0.46 mm OD).

such that the distal-most cutout has the deepest cut depth and thus the lowest actuation force, and the more proximal cutouts have an increasingly shallower depth of cut.

In order to achieve tip-first bending, we first select the number of cutouts n and cut height h of the cutouts in order to specify the bending radius of the wrist. We then determine the cut depth for the most proximal cutout, as we want this cutout to require the greatest actuation force and bend last. The cut depth of the proximal cutout is chosen such that the uncut region experiences the largest allowable material strain at full bending, given by $\varepsilon_{max} = \varepsilon(r_o, 1/r_o) = \frac{r_o - \bar{y}}{r_o + \bar{y}}$. We use this equation along with Eqs. (3.1) and (3.2) to determine the maximum allowable cut depth for the proximal section, g_p. We then select the cut depth of the most distal cutout to be $g_d = r_o + r_i$, which corresponds to the lowest allowable actuation force and material strain. Lastly, we linearly select the remaining cut depths using $g_i = \frac{g_d - g_p}{n-1}$, where g_i corresponds to the increase in cut depth of each remaining cutout, starting from the most proximal cutout and moving to the most distal cutout.

Tip-first bending can be seen in Fig. 3.16, where the proximal cutout had a depth of 0.965 mm, the middle cutout had a depth of 0.985 mm, and the distal cutout had a depth of 1.005 mm. The nitinol tube used to make this wrist had an OD of 1.16 mm and an ID of 0.86 mm. The wrist was manufactured using the CNC method described in Section 3.6.

3.8 Discussion

The aim of this work was to provide additional degrees of freedom and dexterity to needle-diameter surgical tools while incorporating a simple actuation scheme and integration with existing tools. The wrist presented in this chapter accomplishes these goals. The wrist provides increased distal dexterity through the use of asymmetric cutouts in a nitinol tube, it is actuated using a single tendon, and the wrist is manufactured into the tool shaft

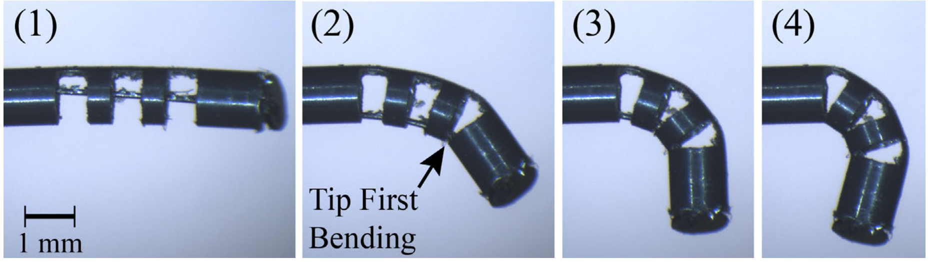

Figure 3.16: This sequence shows the wrist bending from the tip first. In order to accomplish this behavior, the wrist is manufactured such that the most distal cutout has the deepest cut depth, and each sequential cutout is shallower than the cutout before it. This lowers the required actuation force for the most distal cutout, and results in the behavior seen here.

itself making integration with current rigid needlescopic tools straightforward. The modeling results predict the behavior of the device and enable design of the wrist for specific surgical tasks. The wrist is straightforward and low-cost to manufacture, and the design is scalable. The wrist design presented here may enable surgical approaches that are currently impossible using existing rigid needlescopic tools.

Despite the simplicity of the design, there remains a large design space for varying the wrist performance. In this work, we restrict our attention to analyzing rectangular-shaped cutouts, which can be inexpensively manufactured using conventional micro-milling techniques. Using a rectangular cutout profile, the designer is able to select the height, depth, and spacing between the cuts, in addition to the number of cutouts and the outer and inner radii of the tube. Using the models and design principles in this work, the user can create a wrist that has desired performance characteristics such as minimum radius of curvature, maximum bending angle, and maximum tendon actuation force.

The two most important features of the wrist are the tube radii and the depth of cut, as they determine the location of the neutral bending plane, which consequently affects the kinematics, the strain in the portion of nitinol in bending, and the actuation force. The cut height is not as critical as the cut depth at determining the wrist performance, but it does affect the bending radius of the wrist and care must be taken not to make the cut height too large, or else the risk of buckling will increase and the constant curvature assumption will no longer hold. Decreasing the spacing between the cuts decreases the radius of curvature of the wrist, so one should select the smallest spacing that is able to withstand the required actuation forces without breaking. The use of non-uniform cut depths also affects the performance of the wrist, as illustrated in Sec. 3.7.2, and this capability may prove useful for certain anatomical scenarios or tasks. While it is not possible with the tip-first bending design to prevent some actuation of the proximal sections, the method for tip-first bending described in Sec. 3.7.2 provides a good approximation for tip-first bending of the wrist.

A potential source of error in the models is the implicit assumption in (3.11) that cross sections do not deform during bending, which is a common assumption in beam bending analysis. However, because the wrist will ultimately be controlled under direct visual feedback by the physician, these uncaptured effects can easily be corrected by the human-in-the-loop. This also holds true for any discrepancies between the kinematic model and the experimental data. Furthermore, the fact that the experimental actuation force at extreme rotation angles is higher than the model prediction allows for a simple maximum force limit for safety.

One interesting observation from the fatigue test is that the CNC machined wrist had more cycles to failure than the wire EDM wrist. Given the rounded corners of the wire EDM cutout, one might expect these rounded corners to improve the fatigue life of the wrist, but the opposite was shown here. One possible reason for this may be additional heating of the nitinol tube due to the wire EDM manufacturing process, which could alter the material properties of the nitinol and change the performance of the wrist. Additional fatigue tests can help investigate the difference between the number of cycles to failure for the two manufacturing methods. It is also worth noting that the coefficient of friction, an unknown parameter that was selected for agreement between the model and the experimental data, depends on factors such as surface finish and geometry.

In this chapter, a needle-sized wrist that increases the dexterity of needle-sized tools while using a simple actuation scheme and a straightforward method for integration with existing tools was described. The wrist consists of a nitinol tube with asymmetric cutouts that is actuated by a single tendon in order to provide significant distal curvature. Kinematic and statics models were derived and experimentally validated, and several prototypes of the wrist were presented and tested. The additional dexterity provided by the needle-sized wrist may one day enable surgeons to perform new scarless procedures while also navigating and operating around sharp corners in the anatomy.

Chapter 4

Toward Transoral Peripheral Lung Access:
Combining Continuum Robots and Steerable Needles

4.1 Chapter Overview

Lung cancer is the most deadly form of cancer in part because of the challenges associated with accessing nodules for diagnosis and therapy. The two main approaches for accessing suspicious nodules today are a percutaneous needle approach and a transoral bronchoscopic approach. While the percutaneous needle approach is accurate, it has a high risk of lung collapse. Therefore, transoral access is preferred due to the lower risk of lung collapse; however, many sites are currently unreachable transorally due to limitations with current bronchoscopic instruments. What is needed is a system that provides the safety of a transoral approach with the efficacy of a percutaneous approach. In order to directly address the problem of safely and accurately accessing lung nodules throughout the lung, we have developed a transoral robotic image-guided system. The system uses a bronchoscope to navigate in the airway and bronchial tubes to a site near the desired target, a concentric tube robot to move through the bronchial wall and aim at the target, and the dexterous flexure-tip needle developed in Chapter 2 to accurately maneuver through lung tissue to the target under closed-loop control. In this chapter, we illustrate the workflow of our system and show accurate targeting in phantom experiments. Ex vivo porcine lung experiments show that the flexure-tip steerable needle can be tuned to achieve appreciable curvature in lung tissue. Lastly, we present targeting results with our system using two scenarios based on patient cases. In these experiments, phantoms were created from patient-specific computed tomography (CT) information and our system was used to target the locations of suspicious nodules, illustrating the ability of our system to accurately reach sites that are traditionally inaccessible transorally. The results found in Chapter 4 are in press in the

Journal of Medical Robotics Research [61] and have been presented at the IEEE International Conference on Robotics and Automation in 2015 [115]. The system shows promise at accessing hard or impossible to reach nodules for biopsy, and we believe treatment may one day be delivered concurrently with diagnosis using our system.

4.2 Introduction

More lives are lost to lung cancer in the US than any other type of cancer (≈160,000 in 2014) [48], and early diagnosis is critical to survival. Patients diagnosed with lung cancer in Stage I have an 88% 10-year survival rate [116], while Stage III or IV patients have only a 15% 5-year survival rate [117]. In order to obtain a definitive diagnosis, a biopsy is required for suspicious nodules identified in CT scans. Unfortunately, nodules (which may or may not be cancerous) often develop in the peripheral regions of the lung and are difficult to access for biopsy, leaving some patients with no safe option for definitive diagnosis.

The two most common biopsy procedures used to attempt to reach these suspicious nodules are a percutaneous approach and a transoral bronchoscopic approach. Percutaneous transthoracic needle biopsy is a well-established method with high diagnostic yield for large nodules, but it requires puncturing the pleura (the membrane surrounding the lung). Thus, it carries a significant risk of pneumothorax (lung collapse), a severe and possibly deadly complication that develops in up to 25% of percutaneous biopsies [118]. Other reported complications include pulmonary hemorrhage, pleuritic chest pain, and vasovagal reaction [119]. In addition to these complications, percutaneous biopsy has a low diagnostic yield (<52%) for small nodules under 1.5 cm in diameter [120].

In contrast to percutaneous needle biopsy, bronchoscopic approaches are less invasive, carry a significantly lower risk of pneumothorax (bronchoscopes do not puncture the pleura), and may be the only biopsy option for patients with co-morbidities such as chronic obstructive pulmonary disease. Bronchoscopes are standard medical devices that are deployed transorally. They are typically made with a flexible shaft and a tendon-driven tip that bends when the tendons are actuated using levers on the handle, steering the tip of the bronchoscope [121]. The main drawback of bronchoscopic biopsy is that the bronchoscope can only move through the lung's bronchial tree, and even then, only in the larger bronchi due to the bronchoscope's diameter. This limits the number of nodules that can be biopsied to those within the larger bronchi or in close proximity to them. Furthermore, the diagnostic yield of bronchoscopy falls off significantly the further the nodule is located from the entrance to the lung (82%, 61%, and 53% for central, intermediate, and peripheral nodules, respectively), and the diagnostic yield for small nodules (<2cm) is only 23% [122]. Although bronchoscopic biopsy is safer and less invasive for the patient, these limitations curb the use of bronchoscopy and make it clear that a better transoral approach is needed.

Recently, groups have augmented bronchoscopes with image-guidance, attempting to improve bronchoscopic biopsy (see [123] for a review). The three main approaches are virtual bronchoscopy, eletromagnetic (EM) guidance, and endobronchial ultrasound (EBUS). Virtual bronchoscopy displays a virtual model of the airway that is segmented from preoperative CT images and registered to the live image feed of the bronchoscope, enabling navigational cues to be overlaid on the model [124]. However, even with the benefit of navigational guidance, this approach presents some of the same access limitations as traditional bronchoscopy, notably the inability to travel outside of the bronchi. In EM guidance, small magnetically-tracked instruments are deployed through the bronchoscope and travel further through the bronchial tree than standard bronchoscopes [51, 52]. Nonetheless, these devices are still only intended to move through the bronchial tree and access nodules that are located within the bronchi or in close proximity to them. Furthermore, the diagnostic yield of these systems is only 63%–74% for nodules averaging 2.3 cm [125, 126, 127, 128] (it is also worth noting that these statistics do not include nodules for which no attempt is made due to difficulty of access). One group has recently used a bronchoscopically deployed needle and tunneling sheath under fluoroscopic guidance to create a path to nodules located outside of the bronchial tree [129]. However, the authors note that the device is limited to nodules that are reachable by an obstacle-free (i.e., avoiding critical blood vessels and other sensitive structures) straight-line path. Another promising emerging technology is EBUS in which ultrasound is used to either locally guide the placement of a guide sheath for biopsy [130] or provide image feedback for the deployment of a straight needle from the tip of a bronchoscope [123]. Since our system can, in principle, be used with any guidance modality that can provide the locations of both the target and needle tip, it could potentially be used in conjunction with EBUS in the future to provide steerability to EBUS-guided needles.

Our robotic solution for a better transoral lung system uses concentric tube robots and bevel steered needles to increase the capabilities of standard bronchoscopes (see Fig. 4.1). Concentric tube robots are made from a series of precurved, superelastic tubes that translate and rotate inside one another to create curvilinear motion. Concentric tube devices were some of the first devices made from nitinol during the 1980s [131]. Originally thought of exclusively as needles, in 2006 they were proposed as needle-scale manipulators [132, 133], kicking off a period of active modeling research that resulted in the model typically used today [103, 104]. These robots have been applied in a variety of surgical contexts including endonasal surgery [107], cardiac procedures [106], prostate resection and brachytherapy [105, 134], and retinal vein cannulation [135]. In the lung, there has been work done on planning obstacle-free paths through the bronchi using only concentric tube robots [136]. It has also been shown that concentric tube robots can augment the dexterity of both rigid [105] and flexible [137] endoscopes. In our system, we use this added dexterity to orient and deploy a bevel-tip steerable needle.

Bevel steered needles are made using a flexible needle shaft and an asymmetric tip that causes the needle to bend in a controllable fashion upon insertion into tissue [32]. The field of needle steering has been active for over ten years and has seen numerous advancements including motion controllers, motion planning, and needle tip design (see [138] and [139] for reviews). With our system, we use bevel-tip needle steering for its

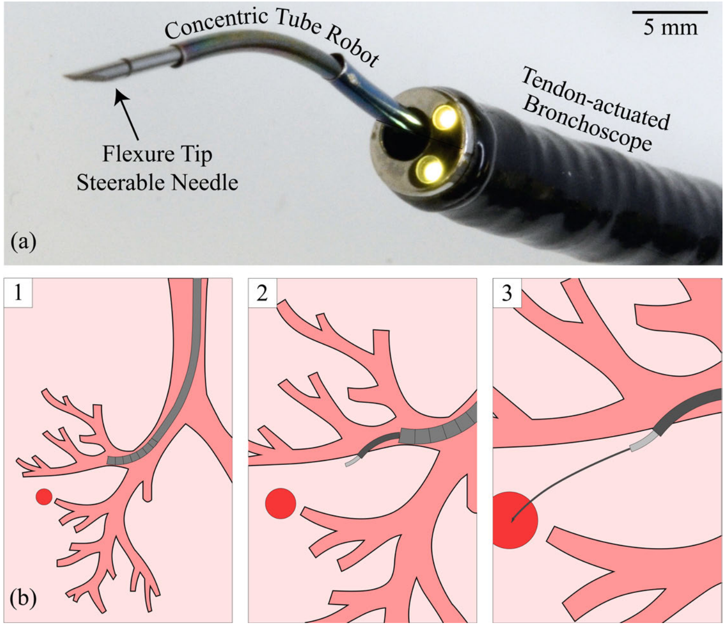

Figure 4.1: (a) Our system combines a tendon-actuated bronchoscope, a concentric tube robot, and a flexure-tip steerable needle to reach locations throughout the lung transorally. (b) The deployment steps for our combined system involve 1) deploying the bronchoscope to a desired site in the bronchial tree, 2) deploying the concentric-tube robot from the bronchoscope working channel to the bronchial wall, piercing through the wall, and entering the lung parenchyma, and 3) steering the flexure-tip needle to the target under closed-loop control.

simplicity and feasibility when deployed through a long, thin pathway. We also incorporate the flexure-tip needle [6] developed in Chapter 2 due to its ability to achieve high curvature while reducing tissue damage when compared to other high-curvature tip designs (e.g., kinked bevel-tip needles [6]). The flexure-tip needle can also deploy through a narrow working channel, something that is difficult or impossible for kinked bevel-tip needles.

This chapter makes a number of contributions to the state of the art. Perhaps most important is our overall system concept in which three kinds of continuum devices are unified to provide a way to access the peripheral lung transorally. This is the first system where concentric tube robots have been used to deploy bevel-tip steerable needles, two ideas that have previously been studied extensively individually. It is also the first system to physically deploy concentric tube robots from a bronchoscope, which is needed to enable practical application of prior simulation and planning algorithms for concentric tube robots in the lung [140, 141]. Experimental contributions include validating that the sliding mode controller of [142] works with the flexure-tip needle of [6] (the controller had previously been used only with traditional bevel-tip needles), and experiments validating aspects of our system using anatomical patient data and ex vivo tissue. Preliminary versions of some results described in this manuscript have appeared previously in conference form [143, 59, 115]. Here, we provide an archival unification of these results, and extend them with additional phantom targeting experiments (Section 4.6.1), a new ex vivo bronchial puncture experiment (Section 4.6.2), a demonstration that a flexure-tip needle can achieve appreciable curvature in ex vivo lung tissue (Section 4.6.3), and a new set of phantom experiments replicating real patient cases (Section 4.6.4).

4.3 System Overview and Workflow

Our system (Fig. 4.1(a)) aims to expand the capabilities of a transoral approach by adding the ability to reach nodules located far from the bronchi through the integration of a concentric tube robot and a bevel-tip steerable needle with a standard tendon-actuated bronchoscope. In our system, the physician first inserts a tendon-actuated bronchoscope to an accessible location en route to the nodule. A concentric tube robot then deploys through the bronchoscope and passes through the bronchial wall, providing access to nodules located in the lung parenchyma (the tissue surrounding the bronchi). Lastly, a steerable needle deploys through the concentric tube robot and drives through the lung tissue to the nodule. Our system will enable access to nodules located in the parenchyma of the lung with less risk of pneumothorax, since the approach does not involve crossing the pleura surrounding the lung. A prototype of our system is shown in Fig. 4.2 and the deployment of the three stages of the device is illustrated in Fig. 4.3. The intended insertion workflow is detailed below:

(1) The surgeon deploys the bronchoscope transorally using standard practices. An Olympus BF 1T30 (Olympus, USA) bronchoscope was used for this work.

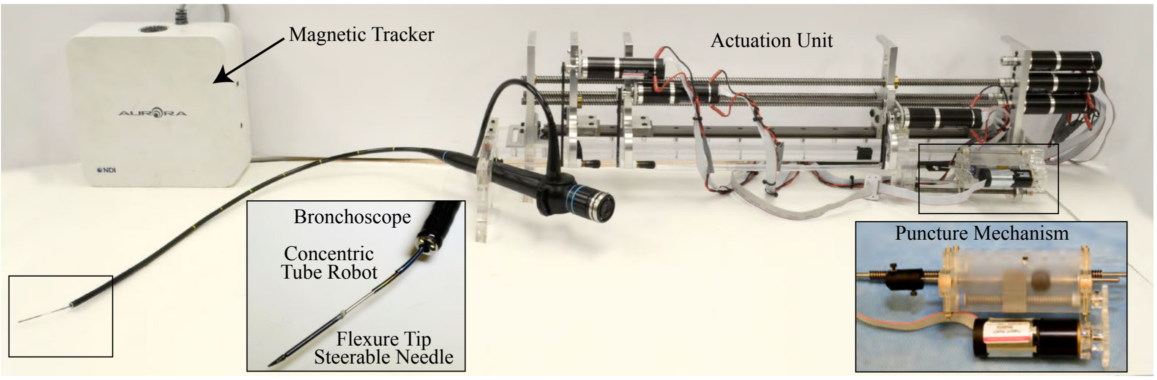

Figure 4.2: The components of the three-stage steering system developed in this work are shown. The system combines a tendon-actuated flexible bronchoscope with a concentric tube robot and a flexure-tip steerable needle to provide transoral access to the peripheral lung. The actuation unit controls the concentric tube robot and steerable needle (see [14] for details on a similar actuation unit), and the piercing mechanism provides access to the lung parenchyma from the bronchial tree. Closed-loop feedback is provided by a magnetic tracking system.

(2) The concentric tube robot extends from the tip of the bronchoscope and moves toward the bronchial wall.

(3) A sharp nitinol wire, which we will henceforth refer to as the "piercing needle," deploys through the concentric tube robot and creates an opening in the bronchial wall using a spring-loaded piercing mechanism. The concentric tube robot is advanced over the piercing needle and through the bronchial wall, and the piercing needle is then removed.

(4) The concentric tube robot aims its tip approximately toward the target nodule.

(5) The steerable needle deploys through the concentric tube robot and is guided under closed-loop control to the desired target.

(6) The surgeon advances a coaxial access sheath through the bronchoscope and over the concentric tube robot and steerable needle, creating an access channel to the target through which a biopsy can be collected or a therapeutic agent can be injected.

We foresee this surgical workflow being performed with the help of image-guidance in a future clinical version of the system described in this chapter. There are two potential

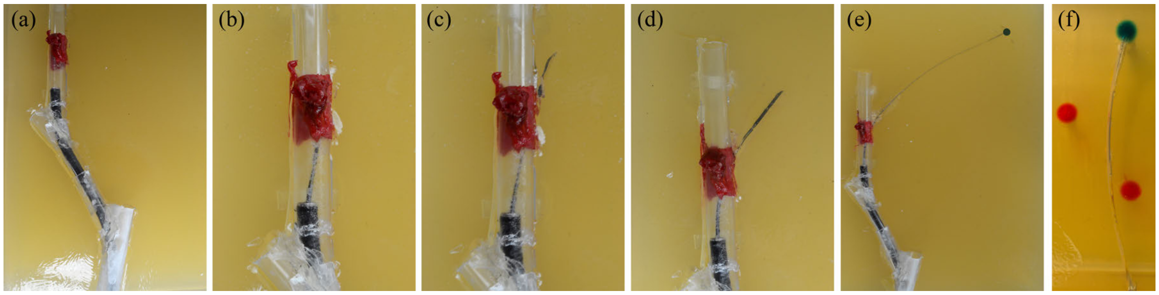

Figure 4.3: Pictures of the deployment steps for our lung system are shown. (a) The bronchoscope is deployed transorally into the bronchial tree. (b) Second, the concentric tube robot extends from the tip of the bronchoscope to the desired location for the opening in the bronchial wall. (c) The piercing needle then deploys through the concentric tube robot and creates the opening in the bronchial wall. (d) The concentric tube robot advances over the piercing needle and through the bronchial wall and aims in the direction of the target. (e) Next, the piercing needle is removed and the steerable needle is deployed from the concentric tube robot to the target. (f) Lastly, an access sheath is passed over the concentric tube robot and steerable needle to the target, allowing for biopsy through the sheath (see Section 4.7 for more details on the access sheath).

imaging approaches that could be used. The first involves taking a preoperative scan of the lung that will be used to identify the target nodule and plan the location of the opening in the bronchial wall and the desired needle path. This preoperative information would then be coupled with intraoperative magnetic tracking feedback for closed-loop control. This approach will require registration between the preoperative and intraoperative data, which is already done in current image-guided lung systems [51, 52]. The other potential approach is to perform the whole deployment with intraoperative imaging such as real-time CT (CT Fluoroscopy) or MRI. In addition to visualizing the system and target during the procedure, this approach would also allow us to see obstacles and critical structures along the deployment path in real time. We believe that our system could be used with either of these imaging approaches. We will now discuss in more detail the devices that are deployed from the bronchoscope and enable our system to reach nodules located in the parenchyma without puncturing the pleura.

4.4 Concentric Tube Robot Subsystem

After the bronchoscope is guided by the physician to the desired site in the bronchial tree (step 1 in Sec. 4.3), the concentric tube robot is deployed out from the bronchoscope tool port. We utilize the concentric tube robot for three important purposes in our system. First, the concentric tube robot enables our system to approach the bronchial wall in a direction as close to perpendicular as possible, aiding with piercing the bronchial wall (step 2 in Sec. 4.3). Second, the concentric tube robot is used to deliver a piercing needle to the bronchial wall (step 3 in Sec. 4.3), creating an access port in the wall for our system to travel through. Lastly, the concentric tube robot is used to align the steerable needle such that the target nodule lies within the reachable workspace of the needle (step 4 in Sec. 4.3). The position of the concentric tube robot can be tracked using the same magnetic tracking coil in the steerable needle since the needle is inside the concentric tubes. The geometric parameters of the concentric tube robot used in this work can be found in Table 4.1. Each tube is comprised of a straight section followed by a precurved section at the distal end of the tube. For each tube, the length of each section and the radius of curvature of the precurved section is provided in Table 4.1.

Table 4.1: Concentric Tube Robot Parameters

	Outer Tube	Inner Tube
Outside Diameter (mm)	1.38	1.14
Inside Diameter (mm)	1.29	0.97
Radius of Curvature (mm)	25.4	17.8
Curved Length (mm)	55	27
Straight Length (mm)	735	833

4.4.1 Deploying from the Bronchoscope to the Bronchial Wall

The added dexterity of the concentric tube robot coupled with the tendon-actuated bronchoscope helps bring the piercing needle from the bronchoscope tip to the bronchial wall

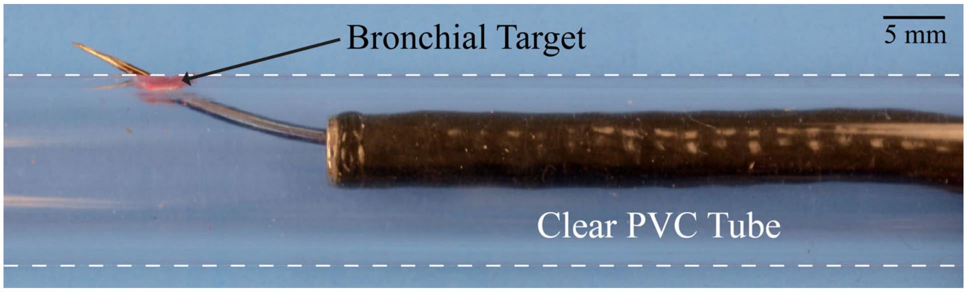

Figure 4.4: The concentric tube robot coupled with the tendon-actuated bronchoscope provide flexibility in selecting the position and orientation of the bronchial wall opening. This added dexterity also assists with orienting the initial pose of the steerable needle. Here, the bronchoscope and concentric tube robot are deployed in a clear PVC tube to a desired bronchial target on the wall of the tube.

(step 2 in Sec. 4.3). In order to assist with creating the opening in the bronchial wall using the piercing needle, it is useful to approach the wall in as nearly a perpendicular direction as possible. We use the concentric tube robot to accomplish this (see Fig. 4.4 for an example). The kinematics used to guide the concentric tube robot are given in [103, 104]. Depending on the desired location of the bronchial wall opening and desired orientation, the physician may choose to deploy one or both concentric tubes from the bronchoscope to the bronchial wall.

4.4.2 Piercing the Bronchial Wall

After reaching the desired site in the bronchial wall with the concentric tube robot, the piercing needle (a 0.78 mm diameter nitinol wire with a sharp conical tip) is deployed through the concentric tube robot (step 3 in Sec. 4.3). Due to the muscular tissue and cartilage rings that make up the bronchi, an impulse is needed to pierce the wall. In order to deliver this impulse to the piercing needle, a spring-loaded piercing mechanism was designed and is shown in Fig. 4.5. It should be noted that creating a hole in the bronchial wall for parenchyma access and nodule targeting has been shown to be safe in initial human trials [129], and that the piercing depth of our mechanism can be set according to the physician's depth specifications to prevent piercing too deep. Upon piercing the bronchial

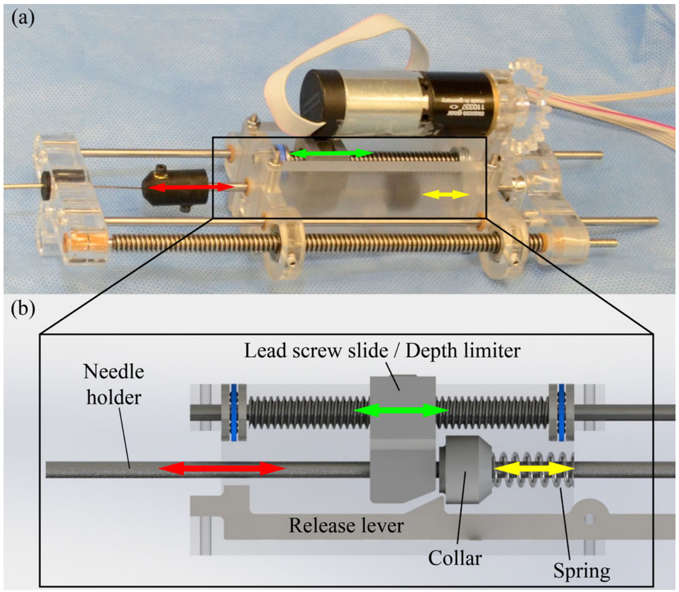

Figure 4.5: (a) View of the piercing mechanism used to impart a rapid motion to the piercing needle that creates a needle-sized port in the bronchial wall. (b) In the piercing mechanism, the lead screw slide compresses a spring until the collar is secured by the release lever. Upon triggering the release lever, the needle holder is propelled forward until it contacts the lead screw slide, controlling the depth of the piercing needle.

wall, the concentric tube robot is advanced over the piercing needle and through the opening in the bronchial wall. The piercing needle is then removed, and the concentric tube robot can now deploy the steerable needle to the target.

4.4.3 Aiming the Steerable Needle

The concentric tube robot (and potentially the tendon-actuated bronchoscope, if additional dexterity is needed) now orient the initial pose of the steerable needle that passes through the inner concentric tube toward the target (step 4 in Sec. 4.3). The ideal alignment of the steerable needle is pointing directly toward the nodule, as this provides both the minimum length to the target and the maximum steerability to correct for disturbances and avoid obstacles along the path. If obstacles prevent this ideal path, the concentric tube robot can position and orient the initial alignment of the steerable needle such that the target still lies within the “trumpet shaped” workspace of the steerable needle. The needle

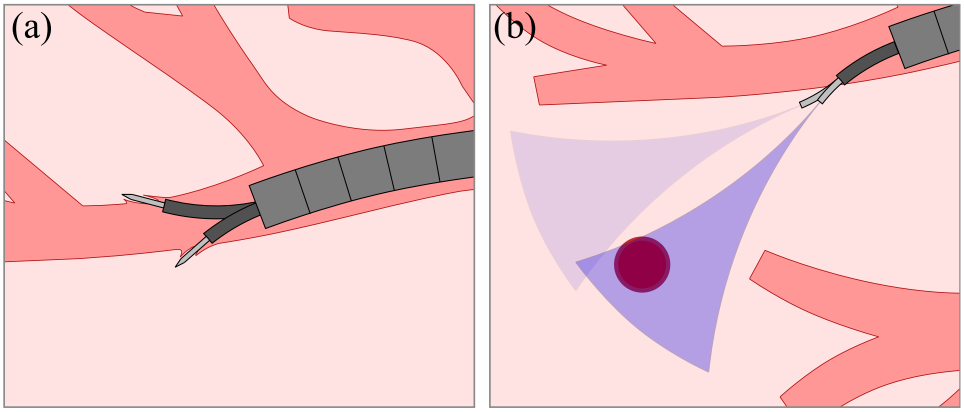

Figure 4.6: (a) The flexibility provided by the concentric tube robot and tendon-actuated bronchoscope when selecting the position and orientation of the bronchial wall opening and initial pose of the steerable needle is illustrated. (b) The concentric tube robot is useful for directing the steerable needle so that the target nodule is within the needle's reachable workspace. An example of adjusting the inner-most concentric tube to redirect the initial alignment of the needle in order to reach the target is illustrated.

can then drive to the target while steering to avoid obstacles along the way. An illustration of aligning a bevel steered needle with a concentric tube robot can be seen in Fig. 4.6. Now that the steerable needle is aligned toward the target, our system delivers the steerable needle to the target using the methods described in Section 4.5.

4.4.4 Non-annular Concentric Tubes

One challenge when deploying the concentric tube robot through the bronchoscope is the torsional windup experienced by the tubes, which can lead to elastic instabilities, and limit the tubes' workspace [144, 145]. However, we have described how one can eliminate the possibility of elastic instability using non-annular (e.g., oval or hexagonal cross-section) concentric tube profiles to lock the relative rotation of the tubes with respect to one another (see Fig. 4.7 and [59] for more details). By locking the relative rotation of the tubes, the tubes can be deployed toward the target nodule without the risk of elastic instability, and without the workspace reductions imposed by it.

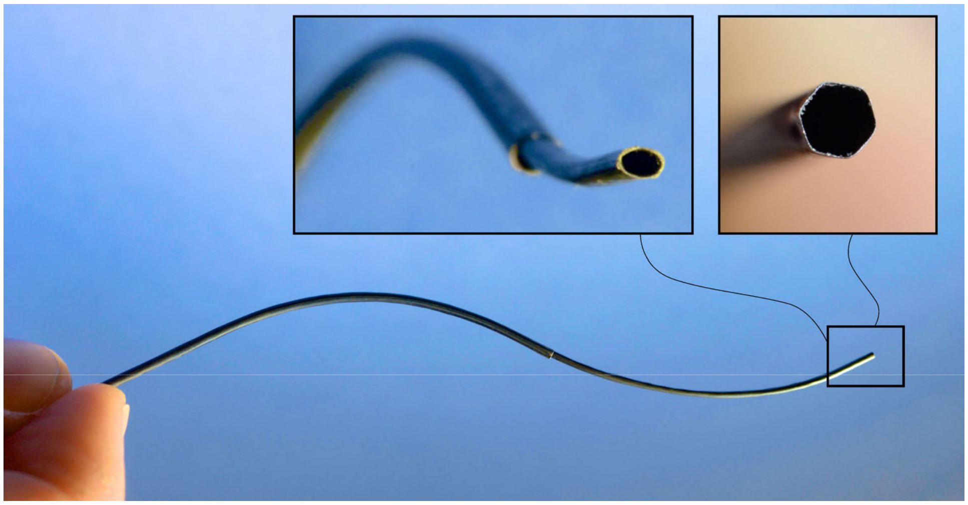

Figure 4.7: The use of non-annular concentric tubes prevents torsional windup along the long transmission lengths of the concentric tube robot by locking the relative rotation of the tubes, thereby preventing elastic instability of the robot.

4.5 Steerable Needle Subsystem

The steerable needle used in our system is the dexterous flexure-tip needle developed in Chapter 2 that consists of a beveled needle tip, a flexible needle shaft, and a flexure joint (see Fig. 4.1b and [6] for further information on this tip design). All three components are made from nitinol. When inserted into tissue, the asymmetric bevel-tip creates a force that bends the flexure and causes the needle to travel in a curved trajectory through the tissue. When no load is applied to the tip, the flexure joint straightens and the needle can easily pass through the concentric tube robot. The flexure joint also straightens when axially rotated while in tissue, minimizing tissue damage when a straight trajectory is implemented via continuous axial rotation during insertion.

The flexure-tip needle we used in our system and for the phantom and anatomical validation experiments in Secs. 4.6.1 and 4.6.4 has a needle shaft with an outside diameter (OD) of 0.8 mm and an inside diameter (ID) of 0.6 mm. The bevel-tip has an OD of 1.16 mm in order to house a six degree-of-freedom magnetic tracking sensor (NDI Aurora, Canada). The bevel tip itself has a length of 4 mm and a bevel angle of 15°. The flexure joint is comprised of three 0.125 mm diameter nitinol wires positioned side by side within the needle shaft (see [6] for additional illustrations of the flexure joint), and the maximum angle the flexure tip can bend is 20°. The length of the entire needle is 1.21 m.

In order to accurately deliver the steerable needle through the parenchyma to the target, we use the sliding mode controller developed by Rucker et al. [142]. Magnetic tracking sensors provide closed-loop feedback of the needle tip pose to the controller. In [142], the controller was validated in the context of reaching target points, trajectory following, and targeting objects that are moving or deforming within the tissue, perhaps due to respiration. In [142], the controller was tested with a traditional bevel-tip needle, so a novel contribution of the experiments in this chapter is verifying that the controller also works for the high curvature and tissue-sparing flexure-tip needle design.

4.6 Experiments

In this section, we validate our robotic solution through a series of experiments. The first set of experiments we performed tested the ability of our system to maneuver in a bronchial tree and deploy the concentric tube robot from the bronchoscope. We then validated the use of the sliding mode controller with the flexure-tip steerable needle and tested the accuracy of our system at delivering the steerable needle to a selected target in a phantom model. After testing the basic deployment concept and targeting accuracy of our system, we experimented with our system in biological and anatomical models to verify use of the system when interacting with realistic tissue and anatomy.

4.6.1 System Feasibility & Accuracy Experiments

In order to test the ability of our system to maneuver in the bronchi and deploy the concentric tube robot, we constructed a phantom bronchial tree model using PVC plastic tubes. Each successive bronchial tube is smaller than the one it extends from, mimicking the structure of the human bronchi. An access hole was cut into the side of the PVC

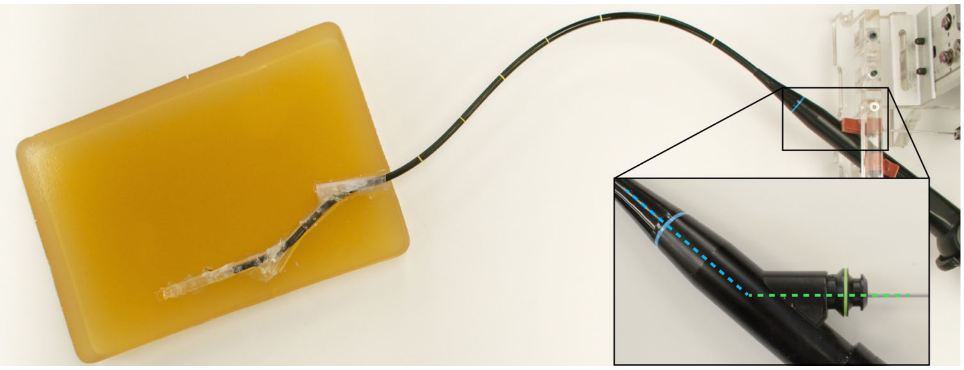

Figure 4.8: The experimental setup used for the system feasibility and accuracy experiments as described in Sec. 4.6.1 consisted of a phantom bronchial tree (made from plastic tubes) that was embedded in phantom parenchyma (gelatin). The inset shows the bronchoscope handle and the sharp bend in the working channel, which is discussed further in Sec. 4.7.

in the third bronchial tube to allow the concentric tubes and steerable needle to exit the phantom. The bronchial tree model was then embedded in gelatin to simulate the support structure of the lung, including the parenchyma (see Fig. 4.8 for experimental setup). The gelatin was made from 10% by weight Knox gelatin (Kraft Foods Global, Inc., USA). The bronchoscope, with the concentric tube robot passing through the working channel, was then deployed through the phantom bronchial tree to a site roughly 1 cm from the access hole. The concentic tube robot was then extended from the bronchoscope up to the gelatin, confirming the system's ability to deploy a concentric tube robot through the flexible bronchoscope as described in Sec. 4.3.

After deploying the bronchoscope and concentric tube robot through the phantom bronchial tree, we validated the use of the sliding mode controller with the flexure-tip steerable needle described in Sec. 4.5, testing the accuracy of our system at delivering the steerable needle to a selected target. The flexure-tip needle with the six degree-of-freedom tracking coil embedded in its tip was loaded into the system, passing through the concentric tube robot and bronchoscope. The concentric tube robot was positioned in the gelatin such that the steerable needle was aiming in the general direction of the target. The flexure-tip steerable needle was then controlled through the gelatin to the target using the sliding mode controller with magnetic tracker feedback. A total of 21 targeting experiments were

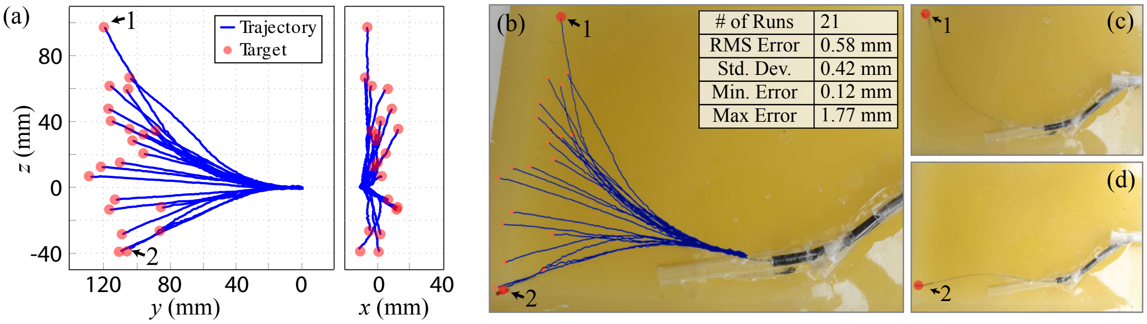

# of Runs	21
RMS Error	0.58 mm
Std. Dev.	0.42 mm
Min. Error	0.12 mm
Max Error	1.77 mm

Figure 4.9: (a) Phantom targeting experimental results of 21 insertions as described in Sec. 4.6.1. (b) The 21 targeting trials are overlaid on the experimental setup. Trials 1 and 2 are explicitly shown in (c) and (d).

performed. The targeting results can be seen in Fig. 4.9.

4.6.2 Bronchial Wall Piercing of ex vivo Porcine Tissue

In order to verify the ability of our piercing mechanism to perform its intended task, we excised a section of bronchial tube from a porcine lung ($\approx$ 1.50 mm wall thickness) and affixed the tissue sample over the access hole in the plastic phantom bronchial tree using cyanoacrylate glue. The bronchoscope and concentric tube robot were deployed to the bronchial wall as described in Section 4.3, and the piercing mechanism then fired the piercing needle to create an access hole in the bronchial tissue. The result of this experiment can be seen in Fig. 4.10(a). Various thicknesses (between 1.15-2.5 mm wall thickness) of in situ porcine lung bronchi were successfully pierced (see Fig. 4.10(b) for an example).

4.6.3 Needle Deflection in ex vivo Porcine Tissue

Another important feature of our system is the ability to steer the flexure-tip needle through the parenchyma. It is commonly assumed in the bevel-tip needle steering literature that one can match needle properties (bevel angle, shaft stiffness, etc.) to any biological tissue of interest in order to achieve appreciable curvature. While examples do exist of needles that have achieved appreciable curvature in brain [146], liver [7], kidney [7], and

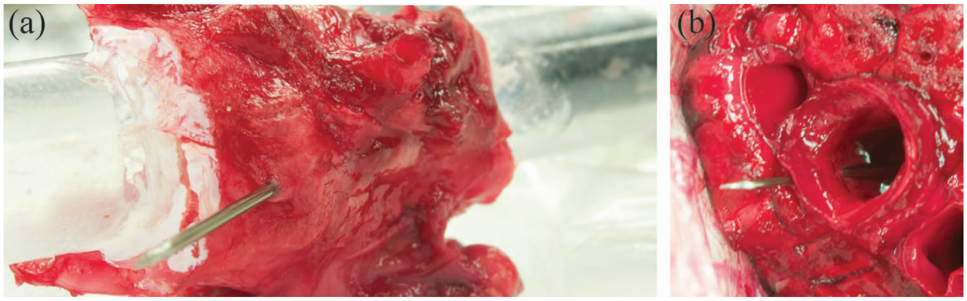

Figure 4.10: (a) Ex vivo porcine bronchial tissue was wrapped around a PVC tube representing a bronchial tube. The piercing mechanism was used to fire the piercing needle through the tissue, as shown here. This created a port in the bronchial wall for the concentric tube robot and steerable needle to deploy through. (b) The piercing mechanism was also tested in whole samples of porcine lung, shown here.

muscle [32], designing a needle for a new tissue type is not trivial. It requires substantial iterative experimentation, since curvature is sensitive to a variety of needle design parameters. Thus, rather than leave to future work verification that a needle design exists that can achieve appreciable curvature in lung, we set out to find a needle design that could achieve curvatures that provide a reasonable needle workspace (see Fig. 4.6(b)).

To confirm that we can design such a flexure-tip needle, we performed a series of open-loop ex vivo experiments. In the first set of experiments, we constructed two pre-bent nitinol needles (i.e. needles where the flexure hinge has been replaced by a permanent bend [7]) with fixed tip angles of 25° and 45° (the 45° needle is shown in Fig. 4.11(a)). Each needle was inserted into the porcine lung sample five times. The measured radius of curvature (RC) and standard deviation (SD) are reported in Table 4.2(a). The results indicate that a tip angle of 45° produces a smaller radius of curvature than the same needle with 25°.

Using the results of the pre-bent needles as a coarse guide, we constructed two new flexure-tip needles with varying geometry (see Figs. 4.11(b) and 4.11(c)) that each had a maximum flexure angle of 45°. These new needles employed the same basic flexure design as the needle used in Secs. 4.6.1 and 4.6.4, but with different needle parameters (e.g., number of flexure wires and tip diameter) selected for lung tissue, in contrast to the gelatin

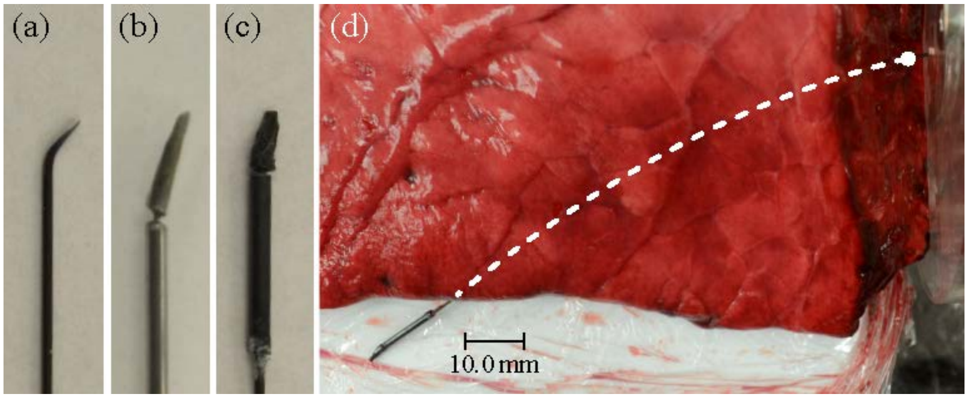

Figure 4.11: The three needles used for the ex vivo porcine lung insertion experiments with results presented in Table 4.2. (a) The 45° pre-bent needle. (b,c) The two flexure-tip needles. The flexure-tip needle shown in (c) produced paths with the smallest radius of curvature, and a representative path generated by the same needle is shown in (d).

(a) Pre-bent Needle (Fig. 4.11(a))

Wire Dia.	Tip Angle	Tip Len.	RC	SD
0.558 mm	25°	2.9 mm	733.4 mm	109.2 mm
0.558 mm	45°	2.9 mm	268.1 mm	164.6 mm

(b) Flexure-tip Tube Needle 1 (Fig. 4.11(b))

Tube O.D.	Tube I.D.	Tip Len.	RC	SD
0.8 mm	0.6 mm	4.2 mm	717.5 mm	243.2 mm
Bev. Angle	Max Angle	Flex. Wires		
10°	45°	3		

(c) Flexure-tip Wire Needle 1 (Fig. 4.11(c))

Wire Dia.	Tip Dia.	Tip Len.	RC	SD
0.51 mm	1.16 mm	3.0 mm	255.0 mm	66.2 mm
Bev. Angle	Max Angle	Flex. Wires		
30°	45°	2		

Table 4.2: Measured radius of curvature (*RC*) in porcine parenchyma. The average RC and standard deviation (*SD*) of $n = 5$ open-loop needle insertion trials into ex vivo porcine lung for (a) two pre-bent needles, and (b), (c) two flexure-tip needles (shown in Fig. 4.11). The wire diameter (*Wire Dia.*) measures the external diameter of the shaft wire, the bevel angle (*Bev. Angle*) measures the angle of the bevel tip relative to the longitudinal axis of the shaft, the tip length (*Tip Len.*) measures the length of the needle tip after the pre-bend in the shaft or the length of the flexure-tip after the flexure, the tip diameter measures the external diameter of the tip flexure joint assembly, the maximum angle (*Max Angle*) measures the maximum angle the flexure tip can deflect, and the number of flexure joint wires (*Flex. Wires*) describe the number of 0.125 mm diameter nitinol wires used to create the flexure joint.

used prior. The results of five open-loop insertion trials are presented in Table 4.2(b) and (c) for these flexure-tip needles. The smallest radius of curvature achieved in the porcine lung sample was 255.0 mm, which was obtained by the needle whose results are presented in Table 4.2(c) and shown in Fig. 4.11(c). A representative path produced by this needle is shown in Fig. 4.11(d).

4.6.4 Anatomical Case Studies

Lastly, to illustrate the benefits of our system at reaching targets that are difficult or impossible to reach transorally, we present two phantom models based on actual clinical cases of patients with suspicious lung nodules treated at Vanderbilt University Medical Center. Based on their experience, the clinicians in both cases determined that the nodules could not be safely reached via a transoral bronchoscopic approach. The decisions were made based on the location of the nodule, the condition of the patient, and other factors. De-identified CT scans of the patients were used to create phantom anatomical models. We segmented the bronchial tree and nodule for each patient, and plastic PVC phantom bronchial trees were created (in the same manner as Section 4.6.1) to approximately (as near as could be judged by eye, when hand-gluing tube sections together) replicate the geometry of the segmented bronchial structure. The bronchial phantoms were set in gelatin and three target locations were selected for each phantom. The target locations in the gelatin phantom were approximated using the relative location of the nodule centroid with respect to the bronchial tree in the CT scans. The two clinical scenarios are as follows.

Patient 1 - Centrally-located nodule

Patient 1 is a 72 year old former smoker with a right upper lobe nodule that was suspected of being malignant (see Fig. 4.12(a)). This patient underwent traditional bronchoscopy as well as a percutaneous CT-guided biopsy. Both attempts were unsuccessful at accurately reaching the nodule, since the nodule was located too far away from an access bronchial tube for bronchoscopy and was too deep for accurate localization using a percutaneous approach. This scenario motivates our system, since it can target nodules that are not

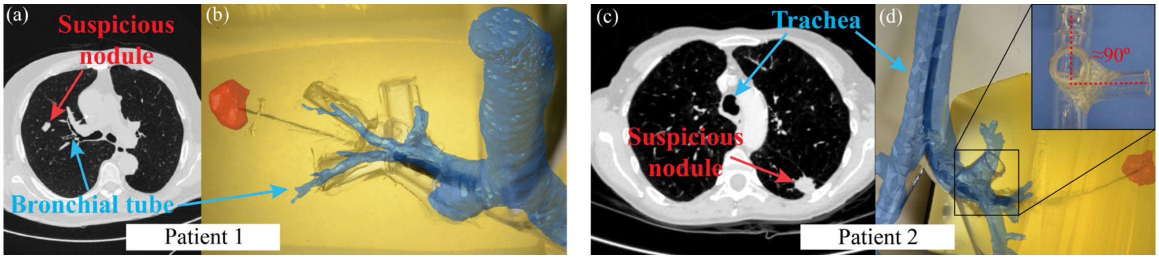

Figure 4.12: Patient case studies in which our proposed system would be particularly valuable. **Patient 1** (a) A suspicious nodule was located centrally in the lung, away from both the bronchial tree and the lung surface. We segmented the bronchial tree and the nodule, and built a phantom to model the anatomy. (b) The segmented anatomy is overlaid on the phantom model. In three trials, the nodule was targeted with an average of 1.33 mm tip error. **Patient 2** (c) A suspicious nodule was located in the periphery of the lung, far from the bronchial tree. The bronchial anatomy was segmented, and a phantom model built based on the anatomy. (d) The segmented model is overlaid on the phantom model, and in three trials the nodule was targeted with an average of 2.02 mm tip error. The inset shows the 90° bend in the bronchus that our system traversed.

immediately adjacent to an access bronchi without puncturing the pleura and the associated risk of pneumothorax. In our anatomical model, we targeted the phantom nodule location three times with an average tip error of 1.33 mm (see Fig. 4.12(b) for an experimental run).

Patient 2 - Peripherally located nodule

Patient 2 is a 68 year old current smoker with chronic obstructive pulmonary disease (COPD) and a suspicious pleural-based pulmonary nodule located in the periphery of the left lower lobe (see Fig. 4.12(c)). This nodule was not able to be accessed with a traditional bronchoscope because of its peripheral location in the lung. While this nodule was relatively easy to access using a percutaneous approach, the patient's COPD increases the risk of a biopsy-induced pneumothorax. In this scenario, it would be safer if the biopsy were performed with the bronchoscopic approach we propose, eliminating the need for a pleural puncture. Note that we selected this case as an example of one that would be challenging for our system, due to the 90° bend the bronchoscope was required to navigate (see Fig. 4.12(d)). Yet even in this challenging case, our system was able to target the phantom nodule three times with an average tip error of 2.02 mm.

4.7 Discussion

The robotic system and workflow presented in this chapter for targeting suspicious lung nodules provides the safety of a transoral approach with the efficacy of a percutaneous approach. Our system has the potential to save lives by enabling earlier stage diagnosis via accurate targeting and minimizing the risk of pneumothorax (lung collapse). While healthy patients usually recover from pneumothorax, it is a serious complication for all patients, and is potentially life threatening for patients with comorbidities or reduced lung function. We anticipate that our system will have a higher yield rate than existing percutaneous and transoral approaches because our biopsy needle is both steerable and controllable in a closed-loop manner, which we expect will result in more accurate targeting (which is particularly important for small nodules). Our approach also has an added benefit over current augmented bronchoscopic approaches in that we anticipate it will enable nodules that are in the periphery of the lung to be targeted transorally, thus broadening the reach of bronchoscopic methods. In this chapter we have demonstrated accurate targeting in gelatin phantoms, as well as successful piercing of porcine bronchial wall and needle deflection in porcine lung tissue. While this work aims to show the feasibility of our combined system and approach, there are also a number of challenges to overcome and opportunities for future research.

One challenge we encountered related to the process of inserting the concentric tube robot and steerable needle through the bronchoscope. The bronchoscope's working channel had a sharp bend in the handle, which makes it challenging to guide tubes through it (see inset in Fig. 4.8). To overcome this, we inserted a thin-walled polytetrafluoroethylene (PTFE) sheath through the working channel, and then inserted our concentric tube robot and steerable needle through this. Even with this sheath, the bend in the handle was sufficiently sharp that it caused mild plastic deformation of the tubes. Since this is only problematic if the deformation occurs at the tip of the tubes, we loaded the concentric tube robot and steerable needle from the tip of the bronchoscope before inserting it into the bronchial tree. In future work, it may be useful to partner with a bronchoscope manufacturer to create a bronchoscope with a straighter working channel to alleviate this challenge.

Since we ultimately intend to use a guide sheath passed over the concentric tube robot and steerable needle to perform a biopsy and/or deliver therapy, we can use the same PTFE guide sheath we passed through the bronchoscope for this purpose. Towards this end, we performed a simple validation experiment in which we passed a PTFE sheath over the flexure-tip steerable needle once it had reached the desired target site. We then removed the steerable needle, leaving the guide sheath in place, and inserted a flexible biopsy tool through the sheath to obtain core samples of the gelatin target. The result of this preliminary study can be seen in Figure 4.13.

Another more minor challenge we overcame in this research is that the concentric tube robot and steerable needle can stiffen the tip of the bronchoscope. Even though the tendons can overcome this and still deflect the tip, doing so will require more force on the bronchoscope control levers. Thus, so that the bronchoscope feels to the operator like it does in current clinical practice, we retracted the tubes and needle past the bending tip of the bronchoscope before deploying it through the bronchi. Also, due to the long length of the bronchoscope, our steerable needle shaft must be long (121 cm), and torsional windup due to friction between the tubes can become a problem. In order to alleviate this, we used a six degree-of-freedom magnetic tracking sensor, providing the full needle-tip pose to the sliding mode controller. This enables us to ignore the torsional windup of the needle shaft and gives us accurate steering results.

The system we present in this work utilizes the bronchoscope, concentric tube robot, and steerable needle to achieve accurate targeting. We note that in some instances under ideal conditions, it may be possible for the bronchoscope and steerable needle alone to accomplish the procedure. In anatomically favorable cases, one or both concentric tubes could potentially be removed, simplifying the system. Additionally, under ideal conditions, it may be possible to use the bronchoscope and the concentric tube robot to reach the target.

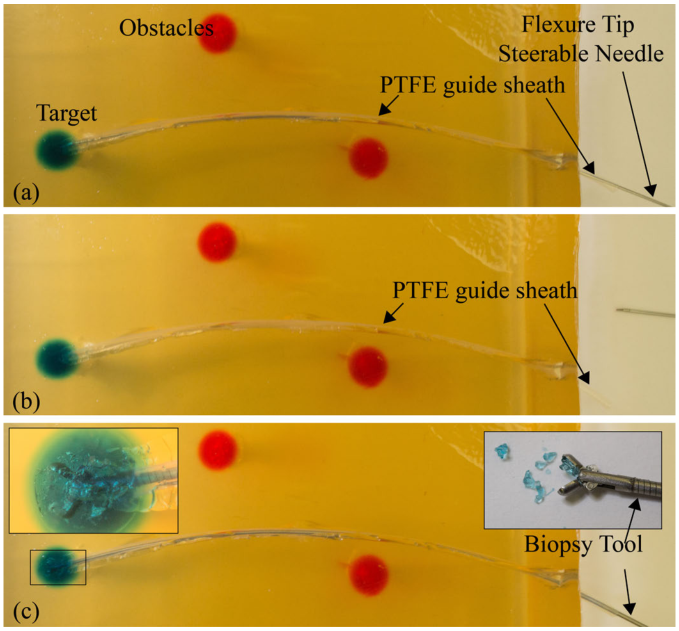

Figure 4.13: A preliminary investigation into the use of a guide sheath for biopsy is shown. (a) First, a PTFE guide sheath was passed over a flexure-tip steerable needle that had reached the target, (b) the needle was removed through the sheath, creating a path to the target, (c) then a flexible biopsy tool was inserted through the guide sheath and used to obtain core samples of the gelatin target.

While concentric tube robots have been shown to be able to achieve follow-the-leader deployment with appropriately selected tube precurvatures and deployment sequences [147], the long transmission lengths required to pass the concentric tube robot through the bronchoscope will make it difficult to keep the concentric tubes stable. Non-annular concentric tubes can help overcome this instability [59], but concentric tube robots deployed in a "follow-the-leader" manner may have trouble correcting for misalignment or unmodeled deflection of the tubes. Ultimately, the use of the bronchoscope, concentric tube robot, and steerable needle together provide redundancy that is useful for targeting nodules throughout the lung, especially in the presence of modeling uncertainty, tissue deformation, and breathing.

Chapter 5

An Endonasal Approach to Tumor Removal Using Concentric Tube Robots

5.1 Chapter Overview

Tumors located at the most inferior part of the skull, called the skull base, are common. In order to reach the skull base, the traditional approaches involve creating an invasive, traumatic opening in either the skull (transcranial) or the cheek bone (transfacial) in order to fully expose the surgical site. Due to the high risks associated with these invasive approaches, surgeons have developed a minimally invasive approach to the skull base. This state of the art approach, called the endoscopic endonasal approach, sees surgeons deploy an endoscope and multiple thin, rigid tools through the nostril to treat tumors at the skull base. Unfortunately, this approach is technically challenging with only a handful of centers of excellence practicing it, and the approach itself has limitations. This means that many patients still must go through traumatic transcranial or transfacial skull base surgery. Clearly, a better approach is needed that makes endonasal surgery the standard of care for accessing and treating skull base tumors. In order to accomplish this, the proposed system must be straightforward to operate, provide surgeons with the necessary surgical tools at the surgical site, and enable surgeons to remove clinically relevant amounts of tumor. Toward that end, we have developed a teleoperated robotic system that uses concentric tube robots to achieve these goals. In this work, we describe the medical motivation for an endonasal surgical robot featuring concentric tubes, illustrate our system concept of a teleoperated robot, and detail the evolution of the system. Two actuation units developed for manipulating the concentric tubes are presented, and custom end effectors that mimic existing skull base tools are developed. The system was experimentally tested to illustrate the ease of use and utility of the system with a laparoscopic training task, a phantom tumor resection experiment, and a cadaver study. Toward ensuring safe operation of our system in the skull, we have developed a novel system calibration method using collisions of the robot arms. This body of work represents the development of our endonasal surgical system beginning from initial concept to a physically realized system. The results presented in this Chapter have been published in the Journal of Neurological Surgery [148, 62] and IEEE Transactions on Mechatronics [107].

5.2 Introduction

As medical technology advances, surgical approaches to the skull base have become less invasive. Where once large, painful, and disfiguring routes (transfacial, translabial, and transseptal incisions) with extensive mucosal dissection were required to reach these areas, the enhanced view provided by rigid endoscopes and high-definition cameras has allowed surgeons to access the skull base via endonasal approaches [149, 150, 151, 152]. These approaches have improved visualization [149, 150, 153, 154, 155], decreased surgical morbidity [149, 156], decreased operative time [156, 157, 158], decreased intensive care unit and overall hospital length of stay [149, 153, 154, 155, 157], decreased complications [150, 156, 157, 158, 159, 160], and lessened the patient discomfort [149, 151, 153, 154, 155, 158, 161] associated with skull base surgery while maintaining a similar degree of resection and equal endocrinologic and visual outcomes [150, 155, 157, 162]. However, these transnasal endoscopic methods have their limitations. The surgery has many challenges due to the confined spaces involved, and the lack of dexterity (see [163, 164]) of current rigid surgical tools, which lack wrists or other means of controllable deflection. Furthermore, there is limited workspace within the nasal cavity, which multiple instruments must share without colliding and without obstructing one another, increasing the complexity of the procedure. Finally, rigid endoscopes, though available with various angled lenses [150, 154, 165] are still limited in their views and vantage points by their rigid and straight shafts [166].

To improve surgical dexterity and simplify the complexity of the procedure while maintaining noninvasive access to the skull base, we have developed a robotic system for transnasal endoscopic skull base surgery. Our system is motivated by a number of recent attempts to use the da Vinci system for surgical procedures in the head and neck [167, 168, 169], primarily using transoral access. The skull base has even been accessed transorally [170, 171]. However, use of the da Vinci to access the skull base through the mouth violates the "keyhole" principle in surgery (i.e. that the smallest and least invasive entry channel that permits adequate access should be employed), because the nose is the most direct and least invasive natural orifice through which skull base access is possible. Nevertheless, these results are a testament to the ingenuity of surgeons in adapting robots for applications never foreseen by robot designers. They also clearly underscore the need for new purpose-designed systems for accessing the skull base, such as the one we describe in this chapter.

There have been a number of robotic systems developed for natural orifice surgery (e.g. [172, 23, 173]) and single port abdominal surgery (e.g. [174, 175, 176]), but few systems have been specially designed for endonasal surgery. One possible reason for this is the limited workspace the nostril provides compared with other natural orifices such as the throat or single abdominal ports. Robotic systems have been used to aid with the initial bone drilling needed to reach the surgical site [177, 178, 179], where surgeons must drill through both the anterior and posterior walls of the sphenoid sinus in order to expose the surgical site. Additionally, others have used robots to assist with maneuvering the endoscope [55, 57], as the current endonasal approach requires an additional surgeon or resident to manipulate the scope during surgery. One group has also outfitted a 4 mm continuum robot with a chip-tip camera for steering through the sinus cavity for visual inspection [180]. All of these prior results are complementary to our current system, which is designed to be deployed after the access channel has been created by bone drilling or other manual procedures, and can work in conjunction with an endoscope or chip-tip camera.

For endonasal surgical robots, the limited space available in the nostril opening, combined with the need to work dexterously within the cavities in the head, implies that instrument shafts must be small in diameter while enabling dexterous motions of the instrument tips. These requirements are well suited for the use of concentric tube robots (see Fig. 5.1), which is why we selected this type of robot for our endonasal system. Concentric tube robots are needle-sized manipulators comprised of a series of nested, precurved tubes that translate and rotate inside one another to create tentacle-like motion of the manipulator [181, 182]. Mechanics-based models for them have been derived [103, 104], and these robots have been applied in a variety of surgical contexts including cardiac procedures [106], neurosurgery [183], lung interventions [61, 140], and retinal vein cannulation [135].

In our system, the surgeon controls the concentric tube robots using a master-slave teleoperation paradigm [184]. This approach allows the robotic system to handle complex tasks such as determining the rigid transformation that maps motion of the user interface to motion of the robot end effectors, freeing the surgeon from having to mentally reconstruct this transformation as is currently required with rigid tools viewed endoscopically. Our system aims to provide increased dexterity and better visualization to expand the role of transnasal endoscopic surgery to larger and more challenging lesions while simultaneously lowering the technical challenges on the surgeon associated with endoscopic endonasal surgery. In this chapter, we describe the system concept and motivation for our endonasal surgical robot. The development of two versions of our endonasal surgical robot is presented, in-

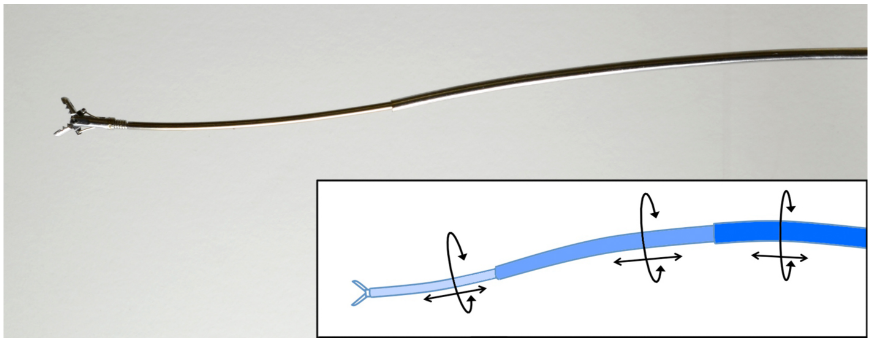

Figure 5.1: Photograph of a needle-diameter concentric tube robot with grasping forceps attached. The inset figure shows the six degrees of freedom of this robot arm. Our system introduces four of these robot arms through a single nostril for skull base surgery.

cluding workspace characterization, tube selection, actuation units, and end effector design. The system is experimentally tested using a number of tasks and the results are reported. Lastly, a system method for calibration of multiple concentric tube robots using collisions is developed.

5.3 Medical Motivation and System Concept

Tumors arising at the skull base are common. For example, pituitary tumors account for 15-20% of all primary brain tumors [54], but are fortunately almost always benign. The American Brain Tumor Association even states that 10-20% of the general population have a pituitary tumor [54], though many may not even realize it because these are slow-growing tumors. However, depending on their size and location, these tumors can cause headaches, visual impairment or loss, and hormonal abnormalaties, and surgical resection of the tumor in these cases is performed.

Endonasal skull base surgery requires tools that can work dexterously at the skull base, reaching around protrusions of bone, to access tumors and other structures. Existing surgical tools are rigid and straight, limiting their effectiveness and increasing the complexity of the procedure, while making minimally invasive endonasal access to certain other areas and tumors incredibly difficult. One such disease is tuberculum sellae meningiomas (see Fig. 5.2) which are located above and in front of the pituitary gland at the skull base. Only a few experimental procedures have been performed endonasally by expert surgeons in carefully selected patients [185]. If surgeons had access to more dexterous surgical tools and visualization, these tumors could potentially be removed endonasally, preventing the need for large traumatic incisions. We believe that the use of tentacle-like concentric tube robots will provide less invasive access to the skull base with increased dexterity at the surgical site.

Toward this end, we developed a robotic system conceptually similar to the da Vinci robot [184], in which the surgeon is seated at a master console, controlling a remote slave

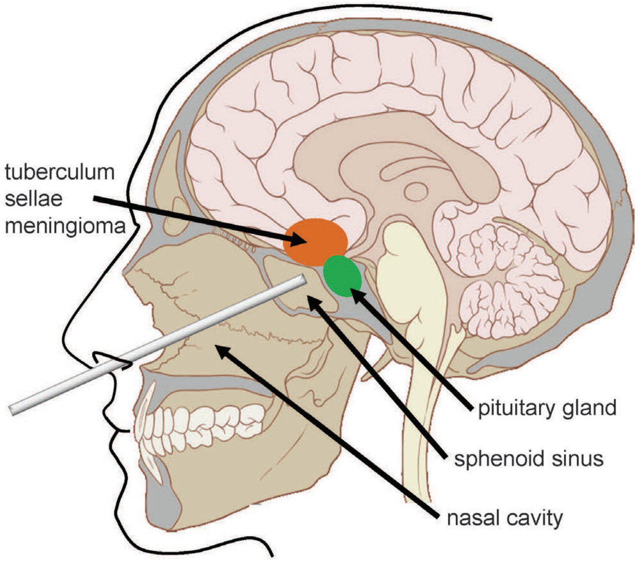

Figure 5.2: Endonasal approach to the pituitary gland using a straight tool. The nasal cavity has to be prepared in order to gain access through the sphenoid sinus. Regions where tuberculum sellae meningiomas occur are almost inaccessible endonasally with current surgical tools.

that manipulates instruments that enter the patient and perform surgery under physician control (see Figure 5.3). For endonasal skull base surgery, such a system requires a camera for visual feedback and one or more surgical instruments, as well as suction/irrigation. In our system, we chose to include a camera and three surgical instruments to enable simultaneous use of two surgical tools with suction/irrigation and a camera for visual guidance. All of these tools are mounted at the tip of concentric tube manipulators, including the camera, enabling the surgeon to control view angles and visualize areas that may be occluded from the view of a traditional straight endoscope.

In addition to providing enhanced surgical dexterity at the skull base, such a system can also assist with existing clinical challenges such as tool management, where surgeons must be careful not to collide the tools with one another when deployed through the nostril. Preventing inadvertent collisions between instruments (a.k.a. the “sword fighting” effect) could enable surgery to proceed more safely, smoothly, and rapidly. It would also reduce the surgeon’s cognitive load, enabling him/her to be concerned only with the tips of instruments, without having to maintain a mental 3D model of the entire shaft of all instruments

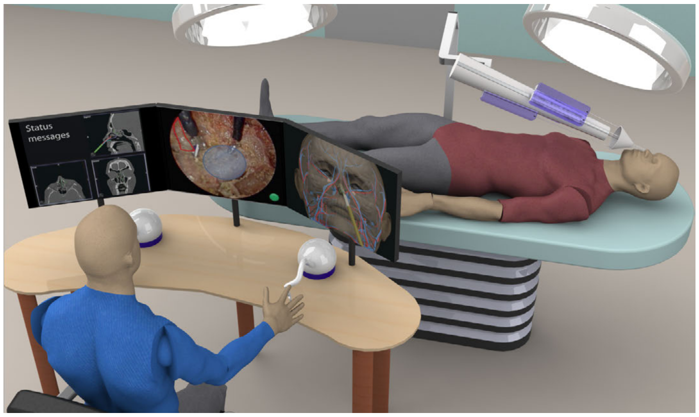

Figure 5.3: Conceptual drawing of the quadramanual system with a surgeon's console showing the tools in the skull base and the cannula paths through the nasal cavity.

at all times. The robotic system can also be integrated into existing image-guidance systems, often used in neurosurgical procedures, to assist the surgeon with localization and navigation [107]. Finally, a teleoperated robotic system can improve the ergonomics of the surgeon. Currently, surgeons must stand at the patient's side and lean over the operating table to manipulate multiple tools through the nostril, leading to fatigue and possibly long term neck and back problems. By moving the surgeon to a seated console, his or her ergonomics can be drastically improved and fatigue can be reduced.

5.4 System Design

The design of a concentric tube robotic system for endonasal skull base surgery includes many different considerations such as the available anatomical workspace and the design of the concentric tubes themselves, actuation of the tubes, how to deliver therapy with the tubes, among others. In this section, we look at the anatomical workspace available to the system, the actuation unit that controls the tubes, and the end effectors of the robot.

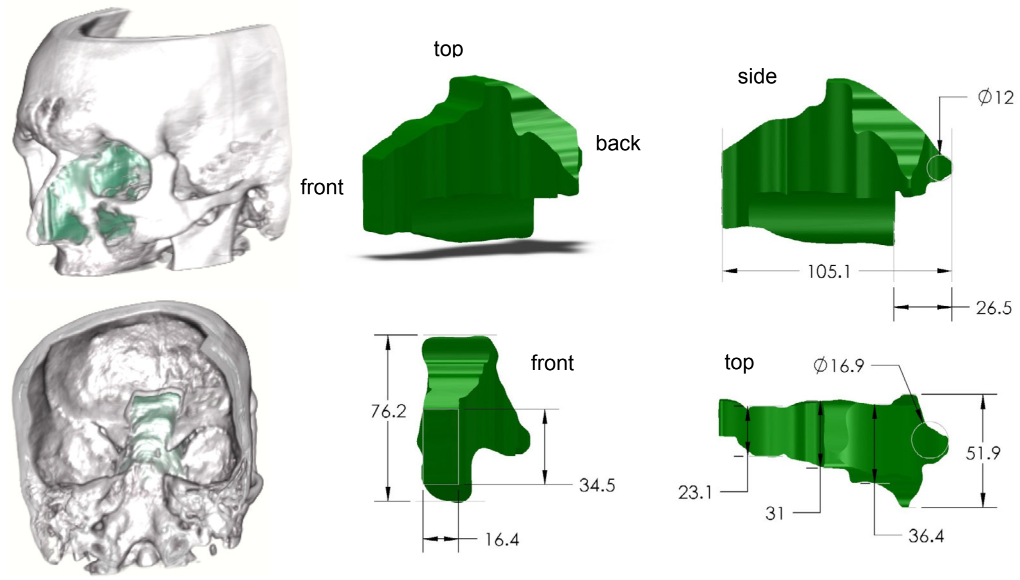

Figure 5.4: The maximum surgical workspace through a single nostril for endonasal skull base surgery of an average sized human is shown. All dimensions are in millimeters.

5.4.1 Workspace Characterization and Tube Design Considerations

In order to characterize the workspace available in pituitary surgery, in [186] we began by manually segmenting preoperative computed-tomography (CT) images of an average adult skull base surgery patient seen at the Vanderbilt University Medical Center. The results of this segmentation are shown in Fig. 5.4. The available space includes a nostril opening of approximately 16 mm x 35 mm, followed by a passage that grows larger as it approaches the pituitary gland at the rear of the workspace (past the sphenoid sinus). The total distance from the nostril entrance to the pituitary is approximately 100 mm. The anatomical site where pituitary tumor removal is performed, called the sella turcia, is roughly ellipsoidal with a 8.5 mm major radius and 6 mm minor radius for healthy patients, and is typically much larger for patients with a pituitary tumor.

The resulting volume of this segmentation can be seen in Fig. 5.4. This patient scan was selected by experienced physicians as a representative anatomical example. All surgical instruments must enter through the nostril opening, and they must be sufficiently long to access the rear wall of the cavity and remove tumor tissue there. The actuation unit

Table 5.1: Optimized tube parameters.

	Tube 1	Tube 2	Tube 3
Straight Length (mm)	100	120.9	164.4
Curved Length (mm)	0	60.2	60.6
Curvature (mm^{-1})	0	0.0084	0.0185
Inner Diameter (mm)	2.8	2.04	1.4
Outer Diameter (mm)	3.05	2.29	1.65

prototypes described in subsequent sections are designed such that travel lengths of each concentric tube manipulator can be adjusted without changing the overall design concept.

When selecting concentric tubes for use in a concentric tube robot, there are a number of parameters that can be customized to meet specific workspace and application requirements. Parameters that may be adjusted include the number of tubes, the tube diameters and stiffnesses, the precurved shape of each tube, the lengths of the tubes, and the material of the tubes. Changes in these parameters can drastically affect the overall workspace of the robot, and there has been recent work in task-specific design strategies (see [187] for a review). These tube parameters also affect the relative stability of the robot, and recent work has provided design constraints to prevent elastic instability throughout the workspace of the robot [144]. Additionally, the use of multiple sets of concentric tubes during a single procedure has been investigated [188]. By changing the tubes during a procedure, one can alter the workspace and performance of the system intraoperatively. To date, the tubes used to make concentric tube robots have been predominantly made from nitinol. However, there is preliminary work investigating the use of plastic tubes [189, 190]. For tube design of an endonasal system, an optimized set of tubes was found in [186] that provided the best coverage of the surgical site shown in Fig. 5.4. The set of optimized tube parameters is shown in Table 5.1.

With all of these tube parameter choices available, it is important to design the actuation units that control the tubes appropriately. The actuation units should provide good performance to the surgeon (e.g., responsive manipulation of the tubes) while being flexible enough to accommodate the wide variety of tube designs that may be selected. In the following section, we describe two prototype actuation units that were built for endonasal skull base surgery and allowed us to test our system concept in multiple environments with various concentric tube robot designs.

5.4.2 Actuation Unit Design

In the course of this work, we have designed and built two separate actuation units for controlling concentric tube robots. The first was a bimanual, or two arm, system that was our initial prototype for investigating the use of concentric tube robots in endonasal skull base surgery. The second was a quadramanual, or four arm, system aimed at providing all four surgical tools we envisioned using during the procedure through a single nostril at once. Both actuation units are described and shown below.

Bimanual System

We designed and built the robotic actuation unit shown in Fig. 5.5 to coordinate the motion of all the tubes (axial rotation and translation at tube bases). In order to actuate these degrees of freedom, there is an individual carrier for each tube which contains two encoded motors (RE 339152, Maxon USA). These were selected based on a desired maximum torque of 0.25 Nm and translational speed of 4 cm/s for teleoperation (torque and speed requirements were qualitatively determined). On a given carrier, translation is accomplished by one motor using a worm gear to spin a nut that rides on a stationary lead screw. The rotation mechanism on a given carrier also uses a worm gear to spin the spring collet used to grasp the base of its respective tube. Use of a collet closure system permits easy replacement of tubes or changes in tube diameters as needed.

The carriers are affixed to a Frelon self-lubricating guide block that rides on an aluminum guide rail. For each three tube robot, three carriers ride on a single guide rail, making up one actuation module. Based on the required workspace, a major design re-

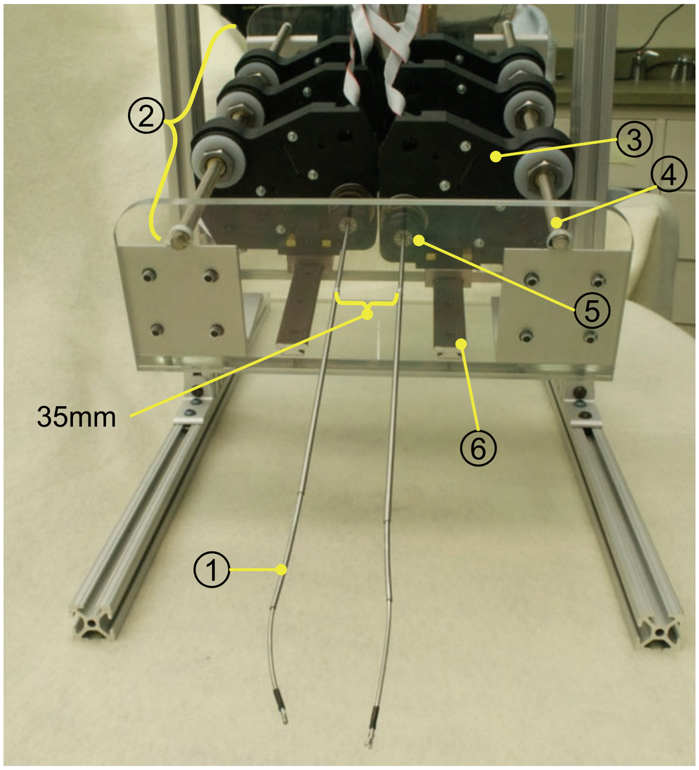

Figure 5.5: Prototype bimanual concentric tube actuation unit. (1) Concentric tube robot with gripper. (2) Actuation module for one concentric tube robot. (3) Carrier associated with one tube. (4) Lead screw for translation of the carriers. (5) Collet closure for grasping a tube. (6) Guide rail.

quirement for the prototype actuation unit is the dimension of 35 mm at the nostril entry, which restricts the maximum distance between the concentric tube robots. In this design, we have mirrored two modules and placed them next to each other, which locates the tubes 35 mm apart. The lengths of the lead screws and guide rail can be adjusted in order to accommodate longer relative travel lengths of the tubes.

Quadramanual System

In designing the quadramanual system, a key objective was to keep the base entry points of all four concentric tube manipulators within the envelope imposed by the nostril opening, similar to the design restraint placed on the bimanual system. The quadramanual system is capable of delivering up to four surgical instruments to the skull base through a single nostril. Each surgical instrument is delivered to the site via a manipulator module, with the module controlling a six degree of freedom concentric tube manipulator. The quadra-

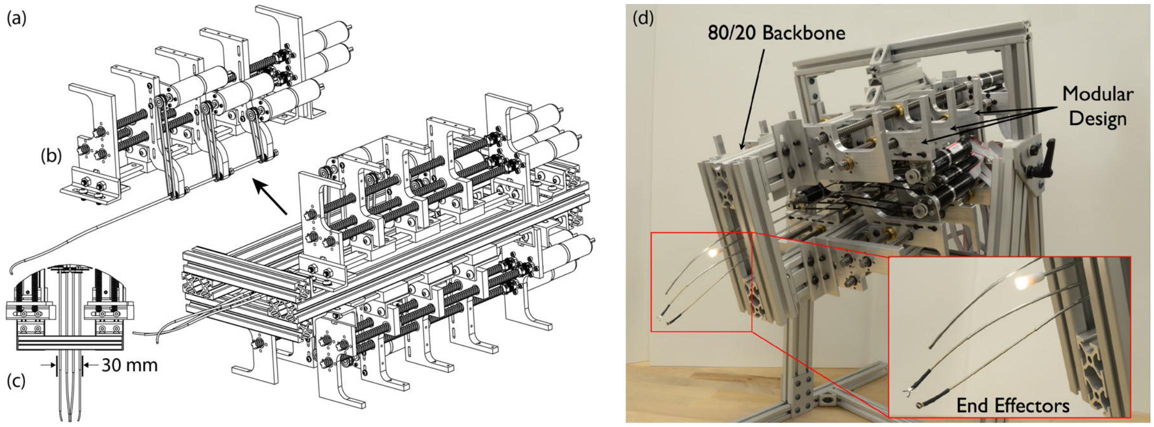

Figure 5.6: (a) CAD drawing of the quadramanual system with (b) one arm removed from the main body and (c) an overhead view of all tubes exiting the robot within the anatomical nostril constraint. (d) Photograph of the complete quadramanual actuation unit showing the modular design and 80/20 backbone. A close-up of the concentric tube robots shows the various end effectors we envision for our endonasal system (ring curette, gripper, suction, and chip tip camera with light source).

manual system consists of four copies of this manipulator module that are mirrored with respect to one another (see Fig. 5.6(a)), allowing the tube bases to exit the robot within the 16 mm by 35 mm opening.

The four manipulator modules are supported by a frame constructed from extruded aluminum (80/20 Inc., USA, shown in Fig. 5.6(d)). This frame serves the secondary purpose of providing a convenient method for mounting the robot to a support arm in the operating room. Since the individual extruded members use slotted connections, the clearances and alignment between manipulator modules can be easily adjusted. The modular nature of the design also allows for each manipulator module to be removed/replaced without having to disassemble the entire robot.

Each of the four manipulator modules contains three identical single-tube stages (Fig. 5.7). Each single-tube stage controls one tube in two degrees of freedom (axial translation and axial rotation). The single-tube stage translates via a captive acme nut that rides on a 3/8-8, 4-start acme lead screw actuated remotely by a DC motor (#339152, Maxon USA) with a 53:1 planetary gearhead. Rotation is accomplished by a motor-pulley-belt system mounted to the stage with an effective gear ratio of 689:17 ($\approx$40.53:1), with the same motor as-

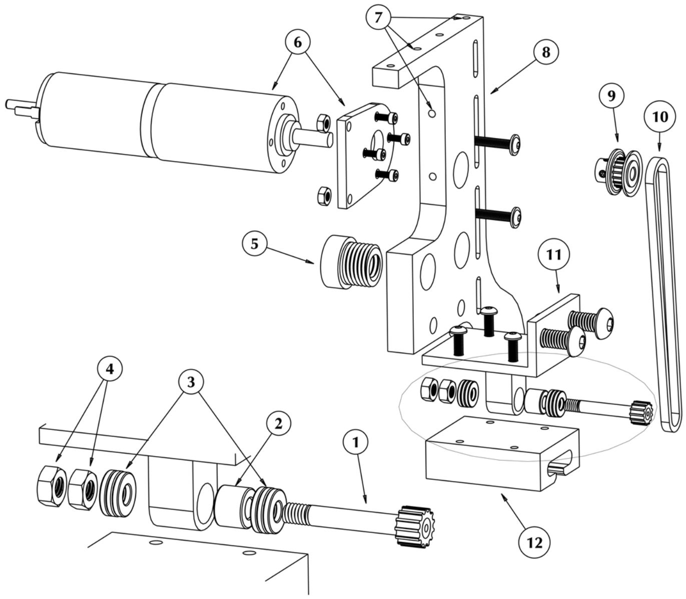

Figure 5.7: Single-tube stage assembly. Exploded view with (1) cannula holder assembly, (2) sleeve bearing, (3) thrust bearings, (4) jam nuts, (5) acme nut, (6) rotation motor and bracket, (7) cable carrier mounting holes, (8) cannula stage body, (9) motor timing pulley, (10) timing belt, (11) stage mounting bracket, and (12) carriage.

sembly being used to rotate the tube. These motors were selected because they provide an excellent power/volume ratio, and will be capable, over a wide range of possible tube designs, of drastically exceeding the design specifications. Each stage is mounted to a PTFE-lined sleeve-bearing, which rides on a shared track (i.e., all three single-tube stages in a given manipulator module share the same track).

Each single-tube stage is designed to accommodate a range of tube sizes. In previous concentric tube robot actuation units, adaptation to different size tubes was accomplished by a collet system, in which, if a new tube diameter was needed, one could replace a commercially available collet with another collet size [186]. While this tube gripping mechanism design is highly flexible, it requires the manipulator modules to hold their respective tubes at a distance of at least one collet diameter from one another. Since we wish to minimize this intra-manipulator distance, instead of collets, each tube was permanently bonded to a cylindrical brass housing (4 mm OD). Each brass housing was bonded to an aluminum pulley on one face, and threaded on the other to secure it to the single-tube stage

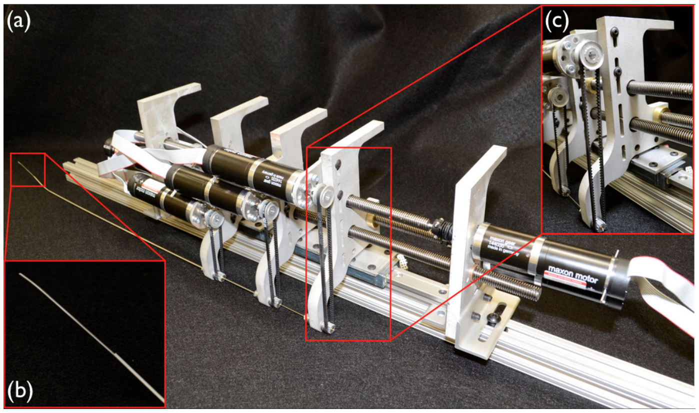

Figure 5.8: a) Photograph of a single manipulator module, b) a close up view of concentric tube robot tip and c) a single tube stage.

(Fig. 5.7). In the assembled device, the brass housing around the tube is supported inside a low-friction sleeve bearing, and secured axially against front and rear thrust bearings by two M4 jam nuts.

Up to three single-tube stages can be mounted on a single manipulator module in our current embodiment (Fig. 5.8). Staggering the motors on each single-tube stage in the three possible mounting locations in the lateral direction (with respect to the tube axis), implies that the minimum distance between stages is limited only by the thickness of the linear bearings that support the single-tube stage on the track. The front end plate on the single track assembly supports the three lead screws via bronze bushings. The lead screw motors (which accomplish translation of each single-tube stage) can be mounted to the front or rear end plates. As in the bimanual system, the lead screws and guide rails are the only components that need to be changed to alter the available travel of the single-tube stages. Each motor is coupled to a lead screw using a flexible coupling which supports axial and radial loads exerted on the screw.

5.4.3 End Effector Design

In our robotic endonasal skull base system, we have created several surgical end effectors that are deployed to the surgical site using concentric tube robots. Ring curettes (rings of metal for scraping away tumor material), are used most often and most extensively in endonasal tumor removal. Since pituitary tumors are soft (similar in consistency to brain tissue), and these rings are thin, yet not particularly sharp, they are useful for scraping away tumor tissue while sparing blood vessels or nerves they may inadvertently contact. The robotic ring curette we have created is similar to the Hardy transsphenoidal bayonet ring curette currently used in endonasal pituitary tumor removal, but with the ability to change the ring angle through rotation of the curette. This allows the surgeon to change the angle of approach of the curette without changing the shape of the entire robot backbone, something that is useful when operating around corners or in tight spaces. The robotic ring curette is shown in Fig. 5.9.

Another useful tool for endonasal skull base tumor removal is a camera to provide the surgeon with more dexterous visualization of the surgical site. Thus, we have attached a miniature chip-tip camera (Awaiba NanEye, Germany) to the end of a concentric tube robot to provide visualization to the system (see Fig. 5.10(a)). A rapid prototyped housing was created to hold the chip tip camera and two LEDs, providing illumination for the camera. While this camera was useful for illustrating the concept of attaching a camera to the end of a concentric tube robot, the picture quality provided by the camera would not be sufficient for surgical procedures. It will be useful moving forward to work directly with a CMOS camera manufacturer to integrate a high resolution camera into the concentric tube robot.

Lastly, the ability to move tissue out of the way and provide suction and/or irrigation

Figure 5.9: The ability to rotate the ring curette axially while the robot arm remains stationary is illustrated in this image via a semitransparent overlay of a second configuration of the curette.

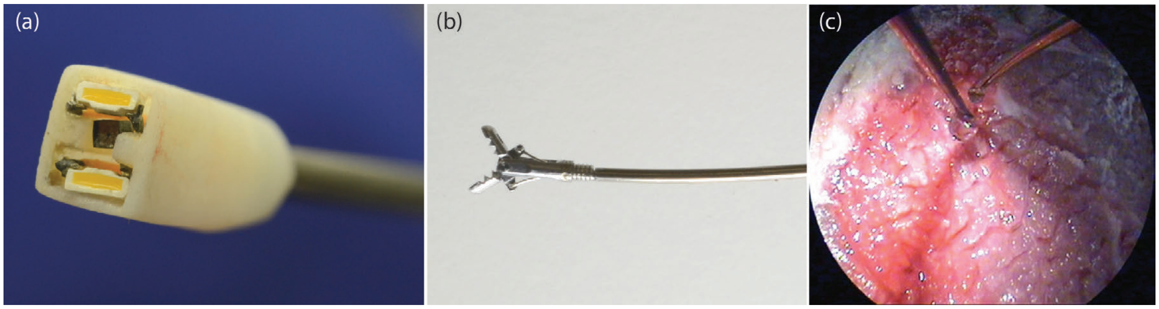

Figure 5.10: (a) A miniature chip tip camera was attached to a rapid prototyped housing along with two LED light sources to illustrate the use of a camera at the end of a concentric tube robot. (b) We utilize a miniature biopsy gripper located at the end of a concentric tube robot for retraction. (c) The concentric tube robot can also be used to provide suction and/or irrigation to the surgical site.

are important tasks for our system. We have integrated miniature biopsy grippers into the concentric tube robot to enable retraction capabilities. These miniature grippers are attached to the tip of the concentric tube robot and then actuated using a single push-pull wire from the back of the robot (see Fig. 5.10(b)). Due to the tubular structure of concentric tube robots, it is also possible to use the innermost tube of the robot itself to provide suction and/or irrigation. This is the principle concept behind a system developed for removing blood clots through suction [188], and we have also shown the use of concentric tube robots for providing irrigation to the surgical site (see Fig. 5.10(c)).

5.5 System Experiments

We have tested our robotic endonasal skull base system using various tasks and anatomical models. In the sections that follow, we detail experiments that were designed to test the usability and dexterity of our system, the utility of our system, and the feasibility of our system.

5.5.1 Pick and Place Task

The aim of this demonstration experiment was to test the ease of use and dexterity of the system by performing a standard laparoscopic task from the Fundamentals of Laparoscopic

Surgery Skill assessment and training program [191]. The goal was to pick up objects from one location and transfer them to another location using the gripper end-effector attached to the end of a concentric tube robot. The experimental setup used for this study is shown in Fig. 5.11. A peg board (100×64 mm) was rigidly attached in front of the robot and the pegs were arranged in a hexagon pattern on the left side of the board (horizontal distance 35 mm and vertical distance 17.3 mm between pegs) and in a rectangular pattern on the right side of the board (horizontal distance 30 mm and vertical distance 17.3 mm between pegs).

Teleoperative control of the robot was implemented as described in [107], such that the robot is able to move in a manner that, from the surgeons perspective, is similar to the da Vinci interface of Intuitive Surgical, Inc. (Sunnyvale, USA). In our system, the surgeon manipulates a user interface (Phantom Omni, Sensable, USA) that controls the position and orientation of the robot manipulator. The surgeon presses a button on the interface to "clutch in" and begin controlling the tip of the manipulator. The surgeon can "clutch out" by releasing the button to reposition his or her hands to a more comfortable position without moving the robot. Using software, we implemented motion scaling to scale down the ratio between the input device velocities and the tip velocities of the end effector, reducing the effects of hand tremor and enabling the surgeon to make more precise movements.

Prior to the experiment, users were given some time to maneuver the robot and establish their preferred motion scaling ratio. The user was then told to transfer the rings from the right side of the board to the left in whatever order he or she preferred. The performance metrics recorded were the number of successful ring transfers, the time taken, and the number of rings dropped. The experiment included a total of 10 participants, some of whom were expert users, others were novices, and two surgeons with moderate familiarity with the system. The results of the experiment are shown in Table 5.2. The mean task completion time of this experiment was 232.4 s with a standard deviation of 33.7 s over all trials, with only one novice user dropping any rings. It is interesting to note that the

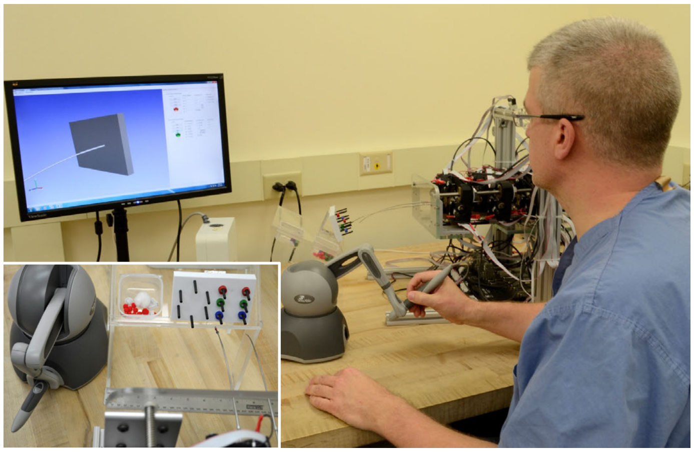

Figure 5.11: The experimental setup used for the pick and place task is shown. The goal was to transfer the six rings from the right side of the peg board to the left side as quickly as possible without dropping any rings.

Table 5.2: Results for transfer task user study.

	User	Time (s)	Drops
Novice	1	187	0
	2	275	2
	3	237	0
	4	241	0
Expert	5	261	0
	6	206	0
	7	270	0
	8	244	0
Surgeon	9	220	0
	10	183	0

novice group performed the task slightly faster on average than the expert group, although the difference is not statistically significant. This may indicate that the learning curve of the system is not steep.

5.5.2 Phantom Tumor Removal

We also tested our robotic endonasal skull base system by performing a phantom tumor removal. We constructed the phantom tumor material using SIM-TEST (Corbin, USA) mixed with water in a ratio of 1 part SIM-TEST to 5 parts water as was done in [148], where the phantom was shown to resemble a pituitary tumor in terms of consistency and required

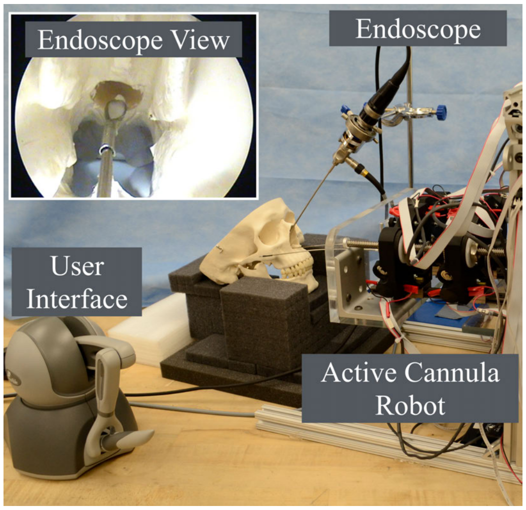

Figure 5.12: Experimental setup for phantom tumor resection experiments using the Phantom Omni user interface.

resection force. The phantom tumor was placed in the skull base of an anatomical skull model (# A20, American 3B Scientific, USA) that the surgeon prepared to closely replicate an enlarged sella as commonly found in pituitary tumor patients. The longitudinal axis of the prepared sella had a length of 3.18 cm, the vertical axis had a length of 2.11 cm, and the lateral axis had a length of 1.97 cm. The total volume of the sella cavity was 6.92 cm^3. The surgeon navigated the robot using a Phantom Omni input device through the nasal passage and was tasked with removing as much of the phantom tumor as possible, using only a standard straight rigid 4 mm endoscope with a view angle of 30 ° for visualization. Both the endoscope and the skull were fixed in place during the procedure (see Fig 5.12 for experimental setup). Manual suction was used to clean the curette from time to time but not to remove phantom tissue directly from within the sella.

The experienced skull base surgeon performed 20 removals of the phantom pituitary tumor using the robotic endonasal system. The percent removal for each trial was determined using the weight of the skull before and after the experiment. We also recorded the total time for each removal. Fig. 5.13 shows the percentage removal and time for each removal. The average percentage removal was 79.8 ± 5.9% and the average time to complete the

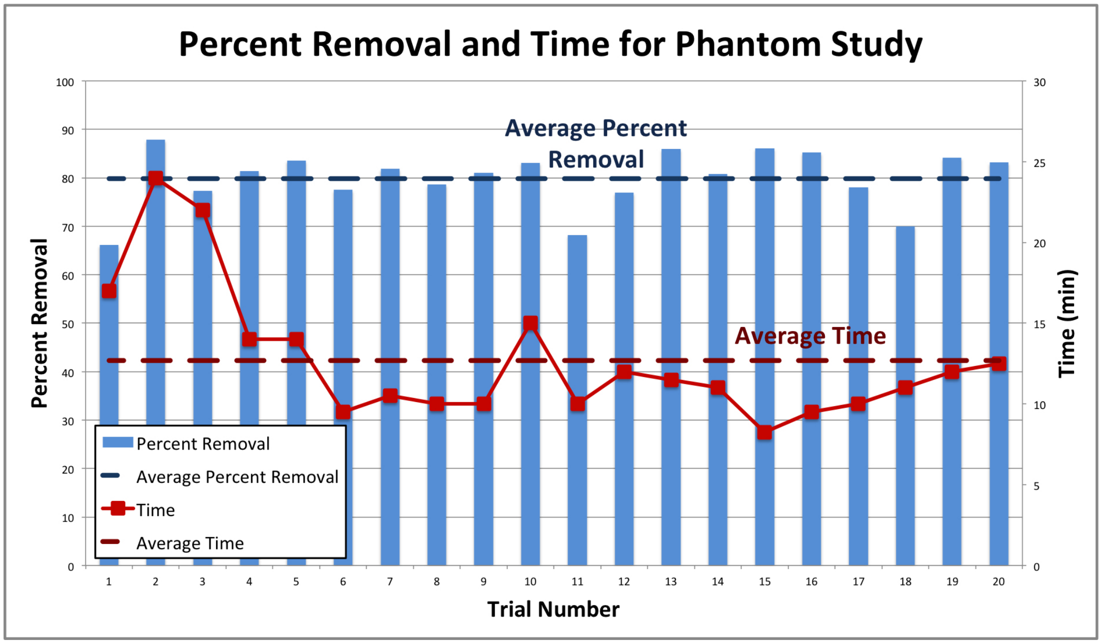

Figure 5.13: Percentage removal and time to complete removal are shown for all 20 removals using the Phantom Omni. The average percentage removal and average time for removal are overlaid on the data, and the trials are listed in order of completion.

removal was 12.5 ± 4.1 minutes, which is comparable to current removal percentage and procedure times (see Sec. 5.7 for additional details regarding clinical removal percentage and procedure time). A thin film of the phantom tumor that covered the surface of the sella was all that was typically left behind after each trial.

5.5.3 Wrist Integration with Endonasal System

One of the most useful features of the dexterous wrist presented in Chapter 3 is the ease with which it can be integrated into needle-sized tools and devices. In order to illustrate this principle, we integrate the wrist with the endonasal concentric tube robot system (see Fig. 5.14(a)) and validate the use of the wrist in this procedure by removing gelatin from a phantom skull base model using the same experimental setup described in [107]. An endoscope view of the wrist deflecting to deliver the phantom tumor to the suction device is shown in Fig. 5.14(b). This qualitative analysis illustrates the utility of the dexterous wrist for skull base applications.

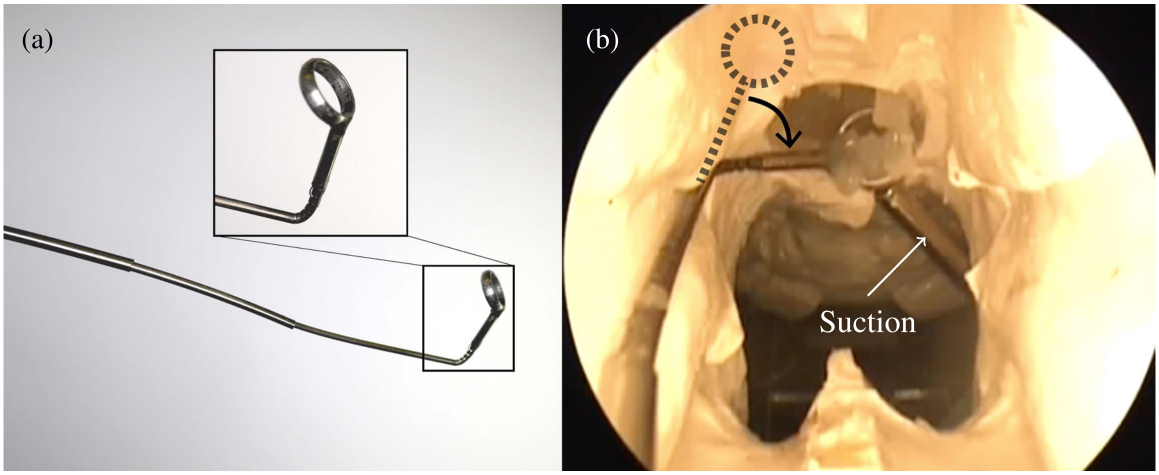

Figure 5.14: (a) Photograph of our wrist integrated directly into the inner-most tube of the concentric tube robot, with an inset showing a closer view of the wrist and surgical curette attached to the wrist. The diameter of the wrist is 1.16 mm. (b) Here, an endoscope view shows the concentric tube robot with integrated wrist being used to remove a gelatin tumor from a skull base phantom model.

5.5.4 Cadaver Workspace Study

To determine clinical feasibility we evaluated our system in a cadaver study. The nasal passages were surgically prepared, the sphenoid sinus exposed, and the anterior wall of the pituitary gland opened. The head was situated on the operating table in the typical position used in endonasal surgery. The robot was situated on the operating table at a relative angle of approximately 45 ° to the head (see Fig. 5.15(a) for the experimental setup). A straight rigid endoscope with 4 mm diameter and a view angle of 30 ° was manually

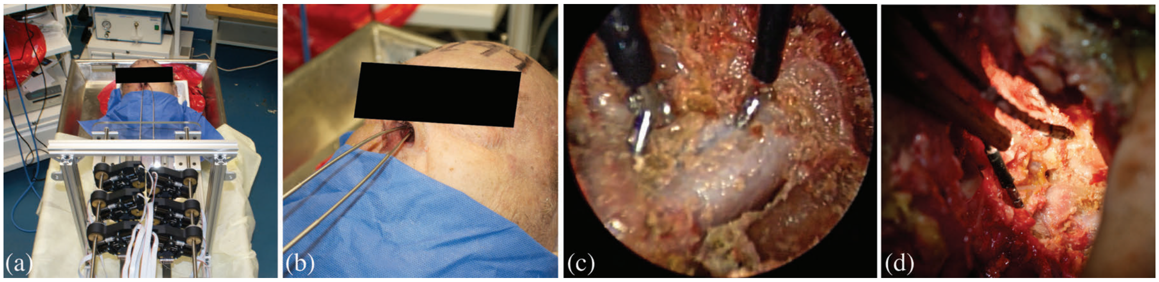
[redacted]
[redacted]

Figure 5.15: Proof of concept cadaver study. (a) System setup in cadaver head study. (b) The two concentric tube robots enter through one nostril. (c) Sagittal view onto surgical site. The endoscope and the two robot arms are shown approaching the frontal wall of the pituitary gland. (d) Intraoperative endoscope view onto the pituitary gland in cadaveric study.

inserted through the nostril and manually maintained in position. Both robotic arms were inserted through the right nostril (see Fig. 5.15(b)) and could reach the pituitary gland while maintaining maneuverability. Fig. 5.15(c) shows an intraoperative image of the endoscopic view onto the pituitary gland. In order to fully observe the instrument tips and endoscope, a dissection of the left facial compartment from the nasal septum was performed. The view inside the skull base was offered through the dissection. The sagittal view onto the surgical site is shown in Fig. 5.15(d).

5.6 System Calibration of Concentric Tube Robots using Collisions

The experiments described above indicate that our robotic endonasal system is a promising technology for providing surgeons with dexterous, minimally-invasive access to the skull base while reducing the technical complexity of the procedure. While our system performed well during the benchtop pick and place task and the phantom removals, neither scenario had any serious consequences for poor system accuracy. The cadaver workspace study, on the other hand, revealed just how little room for error there is when operating the system in the skull base. The carotid artery and optic nerves run directly through the skull base, and hitting either one of these can have severe consequences for the patient. This places a premium on a system that can accurately follow the surgeon's motions, and motivates the need for an accurate calibration of the system. Toward this end, we have developed a novel method for system calibration of concentric tube robots using collisions of the robot arms with themselves.

5.6.1 Introduction & Related Work

Parameter estimation for robots is crucial for accurate and safe operation. This is especially true of surgical robots given the critical structures they must maneuver around and within. Calibration of robots typically proceeds by comparing a parametric model to measurements of a physical system, where kinematic parameters in the model are then estimated using linear least squares (see [192] for an overview). The two main categories of kinematic calibration are open-loop and closed-loop calibrations. In open-loop calibration, an external measurement system (e.g., a camera or laser measurement system) provides the pose of the robot which is compared with the kinematic model. In closed-loop calibration, the robot is calibrated using a closed kinematic chain formed when the robot interacts with an object in the environment. There has been much work done in kinematic calibration of both serial robots (see [193, 194, 195], among others), and parallel robots (see [196, 197, 198], among others). However, research into calibration of continuum robots has been minimal. There are several examples of correcting continuum robot model errors using experimental data [199, 200, 201], and in a recent study, kinematic calibration was investigated on a bionic continuum manipulator that resembles an elephant trunk [202]. In [203], calibration of a concentric tube robot was performed using fiducial markers placed on the tubes and tracked with a stereo vision system. However, all of these approaches for calibration of continuum robots involve the use of costly and/or cumbersome external sensors and are infeasible to perform in the operating room prior to a procedure. If continuum robots are to see more use in the operating room, a straightforward and simple calibration procedure needs to be developed.

In this section, we develop a method to estimate model parameters for multiple continuum robots used cooperatively (we will explicitly be using two concentric tube robots). The novel idea we are proposing is system calibration of continuum robots by exploiting collisions with themselves. Concentric tube robots (and often continuum robots in general) are well-suited to calibration using collisions because 1) they are inherently flexible such that damage to the system is unlikely to occur when a collision is induced and 2) they have a circular cross section meaning the body of concentric tube robots can be well approximated by a simple swept volume in space, simplifying the analysis. We describe the theory behind kinematic calibration using collisions, and then show initial work in calibrating two concentric tube robots in simulation.

5.6.2 Kinematic Calibration

Kinematic calibration can be done for linear and nonlinear models, but since our system is nonlinear, we will only look at nonlinear model calibration. The description of nonlinear model calibration below is adapted from [204] and starts with a Nx1 vector of parameters that are to be calibrated $\boldsymbol{\phi} = [\phi_1, ...\phi_N]$. We take our nonlinear model:

$$\boldsymbol{y}^l = \boldsymbol{f}(\boldsymbol{u}^l, \boldsymbol{\phi}), \tag{5.1}$$

in which $\boldsymbol{u}^l = [u_1^l, ..., u_n^l]$ is the nx1 vector of input variables, $\boldsymbol{y}^l = [y_1^l, ..., y_M^l]$ is the Mx1 vector of output variables, and $l = 1, ..., P$ indicates a particular measurement out of the total number of measurements P. We absorb the input variables $\boldsymbol{u}^l$ into the nonlinear function $\boldsymbol{y}$ since the input variables can be considered as a number of constants. The model is linearized using a Taylor series expansion at the current parameter estimate $\boldsymbol{\phi}^k$:

$$\begin{aligned}
\boldsymbol{y}_m^l &= \boldsymbol{f}(\boldsymbol{\phi}^k + \Delta\boldsymbol{\phi}) \\
&= \boldsymbol{f}(\boldsymbol{\phi}^k) + \left.\frac{\partial \boldsymbol{f}(\boldsymbol{\phi})}{\partial \boldsymbol{\phi}}\right|_{\boldsymbol{\phi}=\boldsymbol{\phi}^k} \Delta\boldsymbol{\phi} + \text{ higher order terms} \\
&\approx \boldsymbol{f}(\boldsymbol{\phi}^k) + \boldsymbol{J}^l(\boldsymbol{\phi}^k)\Delta\boldsymbol{\phi}.
\end{aligned} \tag{5.2}$$

Here, $\boldsymbol{y}_m^l$ are the calculated model values of the output variables and $\boldsymbol{J}^l = \partial \boldsymbol{f}(\boldsymbol{\phi})/\partial \boldsymbol{\phi}$ is the Jacobian matrix relating changes in the parameters to changes in the output variables. We ignore higher order terms in the Taylor series and are left with the linearized form shown above. We now seek the parameter correction $\Delta\boldsymbol{\phi}$ that will cause our predicted model outputs $\boldsymbol{y}_m^l$ to equal our actual measurements $\boldsymbol{y}^l$. We establish an error vector $\Delta\boldsymbol{e}^l = \boldsymbol{y}^l - \boldsymbol{y}_m^l$ as the difference between the output measurements and the calculated model output using the current parameters $\boldsymbol{\phi}^k$, and the linearized equation (5.2) is then:

$$\Delta\boldsymbol{e}^l = \boldsymbol{J}^l(\boldsymbol{\phi}^k)\Delta\boldsymbol{\phi}.$$

If we take P measurements of $\boldsymbol{y}^l$ using different inputs $\boldsymbol{u}^l$, they can then be stacked to obtain the estimation form:

$$\Delta \boldsymbol{e} = \begin{bmatrix} \Delta \boldsymbol{e}^1 \\ \vdots \\ \Delta \boldsymbol{e}^P \end{bmatrix} = \begin{bmatrix} \boldsymbol{J}^1(\boldsymbol{\phi}^k)\Delta\boldsymbol{\phi} \\ \vdots \\ \boldsymbol{J}^P(\boldsymbol{\phi}^k)\Delta\boldsymbol{\phi} \end{bmatrix} = \begin{bmatrix} \boldsymbol{J}^1(\boldsymbol{\phi}^k) \\ \vdots \\ \boldsymbol{J}^P(\boldsymbol{\phi}^k) \end{bmatrix} \Delta\boldsymbol{\phi} = \boldsymbol{A}\Delta\boldsymbol{\phi}, \tag{5.3}$$

where $\boldsymbol{A}$ is the regressor matrix. The correction $\Delta\boldsymbol{\phi}$ to our model parameters is obtained by using ordinary least squares:

$$\Delta\boldsymbol{\phi} = (\boldsymbol{A}^\top \boldsymbol{A})^{-1}\boldsymbol{A}^\top \Delta\boldsymbol{e}. \tag{5.4}$$

We then iterate this process using a new parameter estimate:

$$\boldsymbol{\phi}^{k+1} = \boldsymbol{\phi}^k + \Delta\boldsymbol{\phi}. \tag{5.5}$$

This iteration continues until the change in the error vector $\Delta\boldsymbol{e}$ is below a certain threshold. To ensure good convergence, this method requires a sufficiently good initial guess of the parameters. The above method outlines the basic steps of nonlinear parameter estimation - below we describe our preliminary work using collisions and nonlinear parameter estimation to calibrate two concentric tube robot arms.

5.6.3 Calibration of Two Concentric Tube Robots Using Collisions

We will start by looking at the parameters we want to calibrate and the output data we assume we are able to measure with our system. In the work presented here, we perform calibration in simulation on a two arm, two tube per arm concentric tube robot system, similar to the system used in [205]. Table 5.3 lists the parameters we seek to calibrate and the system measurements we can take, which in our case are the arc lengths s_1 and s_2 along

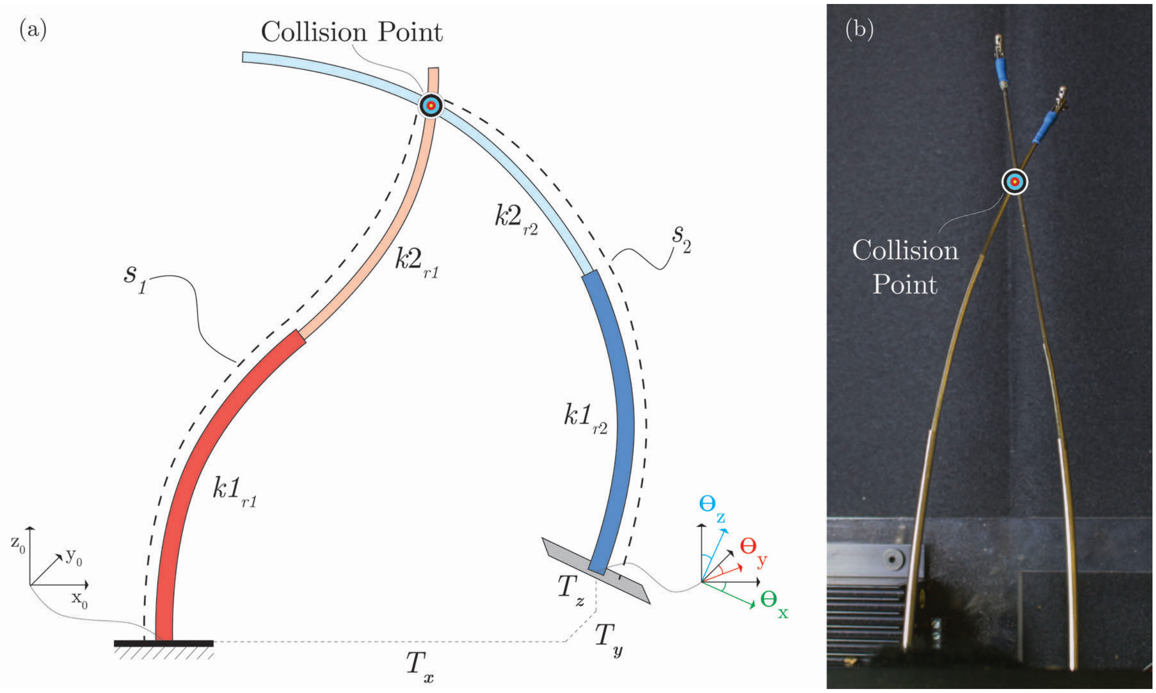

Figure 5.16: (a) An illustration of two concentric tube robots colliding is shown. We refer to the left robot as robot 1 and the right robot as robot 2 throughout. The parameters we seek to estimate $[T_x, T_y, T_z, \theta_x, \theta_y, \theta_z, k1_{r1}, k2_{r1}, k1_{r2}, k2_{r2}]$ in our simulation are shown here, as are the available output measurements $[s_1, s_2]$ of the system. (b) An example of a two arm concentric tube robot system colliding is shown.

the robot backbones to the point of a collision. We note that we are only using two scalar output measurements to calibrate the desired parameters, and that the curved portions of the tubes are circular. See Figure 5.16 for a drawing of a collided configuration of the system with the desired calibration parameters and the output measurements shown. We now look to the model (5.1) that describes the robot backbone positions as a function of the parameters $\boldsymbol{\phi}$ and known inputs $\boldsymbol{u}$, and allows us to determine the arc length collision point along each robot.

Concentric Tube Robot Model

The states of an unloaded concentric-tube robot vary along the backbone arc length s and are the twist angles of the tubes $\boldsymbol{\psi}(s)$ and their rate of change $\boldsymbol{\psi}(s)'$, the arc-length positions of the tube $\boldsymbol{\sigma}(s)$ relative to the tubes' proximal ends, and the backbone position $\boldsymbol{p}(s)$ and

Parameters Sought	
T_x	Translation in the x direction between the two robot origins
T_y	Translation in the y direction between the two robot origins
T_z	Translation in the z direction between the two robot origins
θ_x	Rotation angle of robot 2 origin around the x axis
θ_y	Rotation angle of robot 2 origin around the y axis
θ_z	Rotation angle of robot 2 origin around the z axis
$k1_{r1}$	Curvature of tube 1 for robot 1
$k2_{r1}$	Curvature of tube 2 for robot 1
$k1_{r2}$	Curvature of tube 1 for robot 2
$k2_{r2}$	Curvature of tube 2 for robot 2

Available Measurements	
s_1	Arc length along robot 1 backbone to collision point
s_2	Arc length along robot 2 backbone to collision point

Table 5.3: A description of the parameters we seek to estimate and the available output measurements is provided.

orientation $\boldsymbol{R}(s)$. The states are governed by the differential equation:

$$ {}^i\psi(s)'' = -\boldsymbol{g}(s)^{\top i}\boldsymbol{K}(s)(\partial\boldsymbol{R}({}^i\psi(s))^i\boldsymbol{k}\hat{\boldsymbol{\imath}} \tag{5.6} $$

$$ {}^i\sigma(s)' = 1 \tag{5.7} $$

$$ \boldsymbol{p}(s)' = \boldsymbol{R}(s)\hat{\boldsymbol{k}} \tag{5.8} $$

$$ \boldsymbol{R}(s)' = \boldsymbol{R}(s)\boldsymbol{S}(\boldsymbol{g}(s)) \tag{5.9} $$

where $'$ denotes the derivative with respect to arc length, $\boldsymbol{g}(s)$ is the frame-curvature, the stiffnesses of tube i are in ${}^i\boldsymbol{K}(s)$, the matrix $\partial\boldsymbol{R}({}^i\psi(s) = \partial\boldsymbol{R}({}^i\psi(s))/\partial^i\psi(s)$ where $\boldsymbol{R}({}^i\psi(s))$ is the z-axis rotation matrix, ${}^i\boldsymbol{k}$ is the precurvatuve of tube i and $\hat{\boldsymbol{\imath}}$ is a unit vector in the x direction, $\hat{\boldsymbol{k}}$ is a unit vector in the z direction, and $\boldsymbol{S}(\boldsymbol{g}(s))$ is the skew-symmetric cross-product matrix. The formulation of, and further details on, this model can be found in [181] and [103].

The inputs and boundary conditions for robot 1 are:

$$\boldsymbol{\psi}(0)=\boldsymbol{\alpha}_1,\qquad \boldsymbol{\sigma}(0)=\boldsymbol{\gamma}_1,\qquad \boldsymbol{p}(0)=\mathbf{0},\qquad \boldsymbol{R}(0)=\boldsymbol{I},\qquad \boldsymbol{\psi}(l_1)^{'}=\mathbf{0} \tag{5.10}$$

where $\boldsymbol{\alpha}_1$ and $\boldsymbol{\gamma}_1$ are the actuation-unit rotation angles and translations for robot 1, respectively, and l_1 is the length of robot 1. The inputs and boundary conditions for robot 2 are:

$$\boldsymbol{\psi}(0)=\boldsymbol{\alpha}_2,\quad \boldsymbol{\sigma}(0)=\boldsymbol{\gamma}_2,\quad \boldsymbol{p}(0)=\overline{\boldsymbol{T}},\quad \boldsymbol{R}(0)=\boldsymbol{R}(\theta_z,\theta_y,\theta_x),\quad \boldsymbol{\psi}(l_2)^{'}=\mathbf{0} \tag{5.11}$$

where $\boldsymbol{\alpha}_2$ and $\boldsymbol{\gamma}_2$ are the actuation-unit rotation angles and translations for robot 2, respectively, $\overline{\boldsymbol{T}}$ is the translation between the base frame of robot 1 and robot 2, $\boldsymbol{R}(\theta_z,\theta_y,\theta_x)$ is the fixed-angle rotation matrix around the z,y,x axes by $\theta_z,\theta_y,\theta_x$ respectively, and l_2 is the length of robot 2. We assume that when a tube is not physically present at an arc-length, it has infinite torsional stiffness and zero bending stiffness.

The differential equation (5.6)-(5.9) with boundary constraints, (5.10) and (5.11), for robot 1 and 2, respectively, can be solved using standard two-point boundary-value methods. The result is the backbone position and orientation as a function of arc length s, for robot 1 and 2, denoted as $\boldsymbol{p}_1(s)$ and $\boldsymbol{p}_2(s)$ and $\boldsymbol{R}_1(s)$ and $\boldsymbol{R}_2(s)$, respectively. The nonlinear model in the form of (5.1), that we are calibrating, is given by:

$$\boldsymbol{y}=\begin{bmatrix} s_1 \\ s_2 \end{bmatrix},\quad \text{s.t.}\quad \boldsymbol{p}_1(s_1)=\boldsymbol{p}_2(s_2) \tag{5.12}$$

where s_1 and s_2 are the arc lengths along the robot backbones to the collision point for robot 1 and 2, respectively.

Parameter Jacobian

In order to see how changes in the parameters affect the output measurements, we need to calculate the Jacobian $\boldsymbol{J}^l$ that relates individual changes in our parameters $\boldsymbol{\phi}$ to changes in s_1 and s_2. A central finite difference method is used to obtain $\boldsymbol{J}^l$, which is define as:

$$\boldsymbol{J}^l = \begin{bmatrix} \frac{\delta s_1}{\delta T_x} & \frac{\delta s_1}{\delta T_y} & \frac{\delta s_1}{\delta T_z} & \frac{\delta s_1}{\delta \theta_x} & \frac{\delta s_1}{\delta \theta_y} & \frac{\delta s_1}{\delta \theta_z} & \frac{\delta s_1}{\delta k1_{r1}} & \frac{\delta s_1}{\delta k2_{r1}} & \frac{\delta s_1}{\delta k1_{r2}} & \frac{\delta s_1}{\delta k2_{r2}} \\ \frac{\delta s_2}{\delta T_x} & \frac{\delta s_2}{\delta T_y} & \frac{\delta s_2}{\delta T_z} & \frac{\delta s_2}{\delta \theta_x} & \frac{\delta s_2}{\delta \theta_y} & \frac{\delta s_2}{\delta \theta_z} & \frac{\delta s_2}{\delta k1_{r1}} & \frac{\delta s_2}{\delta k2_{r1}} & \frac{\delta s_2}{\delta k1_{r2}} & \frac{\delta s_2}{\delta k2_{r2}} \end{bmatrix}$$

Since $\boldsymbol{J}^l$ relates changes in the parameters we seek to calibrate (see Table 5.3) to the output measurements s_1 and s_2, we have a short and wide matrix. This fact means that our system is never observable (i.e., there always exist changes to the parameters we are estimating that produce no change in the measured arc lengths to the collision point). In order to overcome this challenge, we obtain data from multiple collisions using different robot poses and stack the data in the same form as (5.3), where $\boldsymbol{A}$ is our regressor matrix that is comprised of P Jacobian matrices of the form $\boldsymbol{J}^l$, where P indicates the number of collision measurements. Because we are seeking to calibrate parameters with different units, it is also important to scale the parameters in order to improve the conditioning of the regressor $\boldsymbol{A}$, enable comparison of the singular values, and help avoid numerical problems.

5.6.4 Scaling of Parameters

In this work, we weight the parameters using column scaling [206] by specifying a diagonal matrix $\boldsymbol{H} = diag\begin{pmatrix} h_1 & h_2 & ... & h_N \end{pmatrix}$ where

$$h_j = \begin{cases} ||\boldsymbol{c}_j||^{-1} & \text{if } ||\boldsymbol{c}_j|| \neq 0 \\ 1 & \text{if } ||\boldsymbol{c}_j|| = 0 \end{cases}$$

in which $\boldsymbol{c}_j$ is the jth column of $\boldsymbol{A}$. We then reformulate (5.3) as

$$\Delta \boldsymbol{e} = \tilde{\boldsymbol{A}} \Delta \tilde{\boldsymbol{\phi}}$$

where $\tilde{\boldsymbol{A}} = \boldsymbol{A}\boldsymbol{H}$ and $\Delta\tilde{\boldsymbol{\phi}} = \boldsymbol{H}^{-1}\Delta\boldsymbol{\phi}$. This is our scaled regressor matrix, and we can use it to perform ordinary least squares (5.4) to solve for $\Delta\tilde{\boldsymbol{\phi}}$, which we use to solve for the correction to our parameter set $\Delta\boldsymbol{\phi} = \boldsymbol{H}\Delta\tilde{\boldsymbol{\phi}}$. The calibration is then iterated until the change in the error vector $\Delta\boldsymbol{e}$ is below a certain threshold using (5.5). We now present our simulation results for system calibration using collisions.

5.6.5 Simulation Results

In our simulations, we have two concentric tube robots whose shapes are determined with our concentric tube robot model and the actual parameter values of the system, and two pre-calibrated robots that use a set of initially erroneous estimated parameters (what we seek to calibrate) as inputs to the concentric tube robot model (see Table 5.4 for the actual and estimated parameters). We first generate a series of collisions by randomly generating an initial pose using the actual parameters of the robots, calculating the closest distance between the two robots, and using resolved-rates to drive these two points into a collided state. We record the arc lengths s_1 and s_2 to the collision point and inject Gaussian noise with a 3 mm standard deviation into these measurements. This process is iterated until $i = N_c$, where N_c is the number of desired collisions for our actual system.

Once we have this data set for our actual system $\boldsymbol{C_{actual}}$, we generate the configurations of our pre-calibrated system $\boldsymbol{C_{p-c}}$ using the same known actuator positions that caused collisions in the actual system. We determine the closest distance between the two pre-calibrated robots and record the arc length along each robot backbone to these points. We calculate the Jacobian that maps changes in $\boldsymbol{\phi}$ to changes in $\boldsymbol{C_{p-c}}$ for each of our collision points. We stack these Jacobians to form our regressor matrix, calculate the error vector between the two sets of collision points $\Delta\boldsymbol{e} = \boldsymbol{C_{actual}} - \boldsymbol{C_{p-c}}$, and scale the parameters with column scaling. We then use ordinary least squares to find $\Delta\boldsymbol{\phi}$ that minimizes the error $\Delta\boldsymbol{e}$. We add $\Delta\boldsymbol{\phi}$ to the parameter estimate $\boldsymbol{\phi}$, and iterate until the change in our error vector $\Delta\boldsymbol{e}$ is below a specified threshold (0.5×10^{-6} m for our simulations). We now have a set

	Guess	**Actual Parameters**	**Calibrated Parameters**
T_x (mm)	34.0	50.0	49.8
T_y(mm)	14.0	7.0	6.9
T_z(mm)	1.0	4.0	3.1
θ_x(deg)	0.6	0.0	-0.5
θ_y(deg)	-0.6	0.0	1.1
θ_z(deg)	0.7	0.0	-0.1
$k1_{r1}$(1/m)	25.4	24.0	23.7
$k2_{r1}$(1/m)	28.2	27.0	27.2
$k1_{r2}$(1/m)	20.2	21.0	20.6
$k2_{r2}$(1/m)	16.8	18.0	18.0

Table 5.4: The actual parameters of the system and the initial guesses of the pre-calibrated system and final parameters of our post-calibrated system are listed. 100 collisions were used to obtain these calibrated values and the calibration ran for 10 iterations. The final tip error for our system was 0.53 mm for robot 1 and 1.06 mm for robot 2 using these calibrated parameters. This corresponds to relative errors of 0.5% and 0.8%, respectively, when normalized by the total robot backbone lengths for this configuration (98.1 mm for robot 1 and 128.5 mm for robot 2).

of calibrated parameters that we can use in our model to most closely simulate the actual system given the measurement data available.

Performing a Calibration with 10 Parameters

We have performed a number of calibrations in simulation, and have shown that we can accurately calibrate 10 parameters of a two arm concentric tube robot using only collisions and measurements of the arc lengths s_1 and s_2 to the collision point (see Table 5.4 for calibrated parameters). We have shown that with added data (e.g., more collisions), we can decrease both the final tip error and condition number of our regressor matrix (see Fig. 5.17), leading to more accurate calibrations, as one would expect. The slight bumps in the mean tip error are likely due to the random nature of the collisions, which do not necessarily represent the set of optimal collision poses. Our best calibration resulted in a 0.53 mm tip error of robot 1 between the actual system and post-calibrated system and a 1.06 mm tip error of robot 2 between the actual system and post-calibrated system. This is a significant improvement over the original tip errors between the actual system and pre-

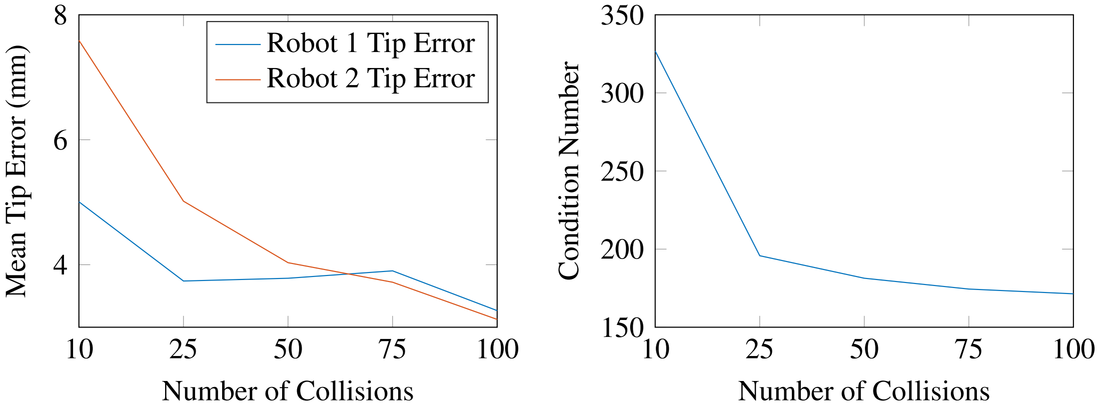

Figure 5.17: The calibrated norm tip error of robot 1 and robot 2 and the condition number of the regressor matrix is shown on the left and right, respectively, for an increasing number of collisions for calibration of the 10 parameters described in Table 5.3. For each group of collisions, we ran the simulation 25 times and took the mean of the norm tip error, which is what we report here. The norm tip error and condition number decrease with increasing number of collisions, as would be expected. The bumps in the plots are likely due to the random nature of the collisions.

calibrated system of 3.8 mm for robot 1 and 19.0 mm for robot 2 for this configuration, and represents a relative error of 0.5% and 0.8%, respectively, when normalized by the total robot backbone lengths (98.1 mm for robot 1 and 128.5 mm for robot 2). The before and after results of this calibration can be seen in Fig. 5.18. This calibration was performed with 100 collisions and ran for 10 iterations.

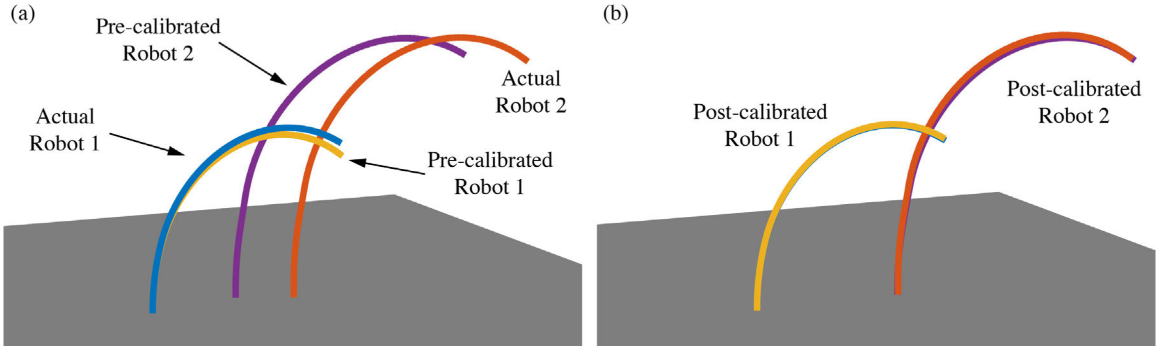

Figure 5.18: (a) This is an example configuration of the actual and pre-calibrated systems. The norm error between the tips of the actual and pre-calibrated robots is 3.8 mm for robot 1 and 19.0 mm for robot 2. (b) This shows the same configuration, but with the post-calibrated system plotted over the actual system. The norm error between the tips of the actual and post-calibrated robots is 0.53 mm for robot 1 and 1.06 mm for robot 2. This corresponds to relative errors of 0.5% and 0.8%, respectively, when normalized by the total robot backbone lengths for this configuration (98.1 mm for robot 1 and 128.5 mm for robot 2).

Performing a Calibration with 16 Parameters

In addition to calibrating for the 10 parameters shown in Table 5.3, we have also added 6 additional parameters to the calibration routine for a total of 16 parameters. The additional parameters are the total lengths of each tube as well as the straight lengths of the inner tubes. Together with the precurvature of the tube, these three numbers completely describe the shape of the tube. The straight length of the outer tube was unable to be calibrated due to the limits placed on the configurations used to create the collisions. When a random configuration was selected to create a collision, the actuator limits placed on the outer tubes meant that changing the straight lengths of the outer tubes would not change the arc lengths to the collision point s_1 and s_2 and thus the straight lengths of the outer tubes were not consistently identifiable. This illustrates the importance of selecting good configurations for calibration. The results of the calibration study for 16 parameters are shown in Fig. 5.19 and the best calibration we obtained resulted in a 0.6 mm tip error of robot 1 between the actual system and post-calibrated system and a 1.1 mm tip error of robot 2 between the actual system and post-calibrated system. This is an improvement over the original tip

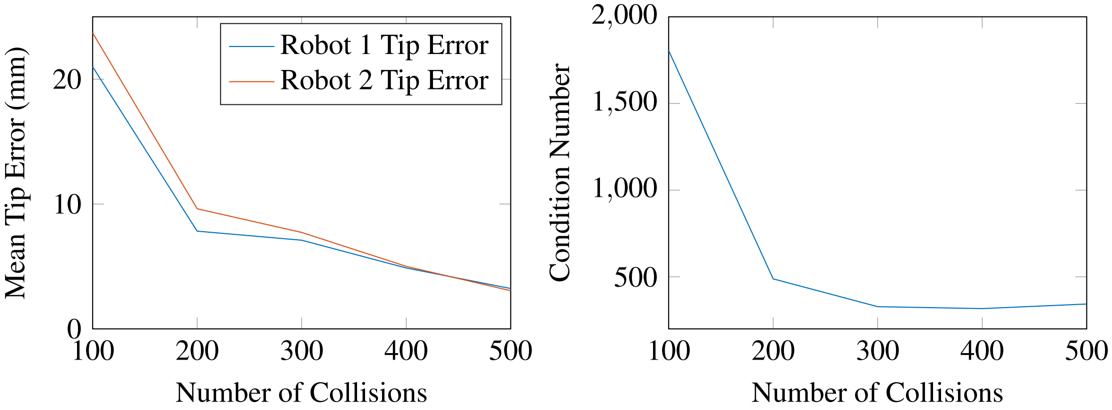

Figure 5.19: The calibrated norm tip error of robot 1 and robot 2 and the condition number of the regressor matrix is shown on the left and right, respectively, for an increasing number of collisions for calibration of the 10 parameters found in Table 5.3 and 6 additional parameters. The additional calibrated parameters are the total lengths of each tube as well as the straight lengths of the inner tubes. For each group of collisions, we ran the simulation 25 times and took the mean of the norm tip error, which is what we report here.

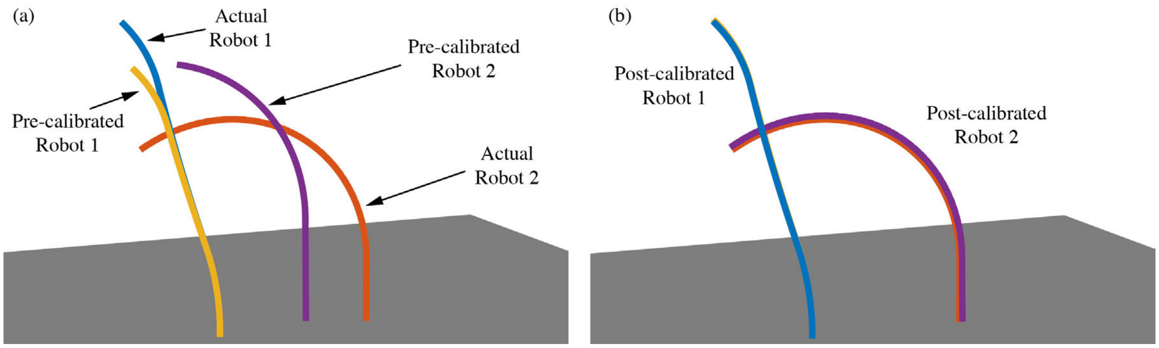

Figure 5.20: (a) This is an example configuration of the actual and pre-calibrated systems when 16 parameters are calibrated. The norm error between the tips of the actual and pre-calibrated robots is 14.0 mm for robot 1 and 28.9 mm for robot 2. (b) This shows the same configuration, but with the post-calibrated system plotted over the actual system. The norm error between the tips of the actual and post-calibrated robots is 0.6 mm for robot 1 and 1.1 mm for robot 2. This corresponds to relative errors of 0.6% and 1.0%, respectively, when normalized by the total robot backbone lengths for this configuration (98.2 mm for robot 1 and 111.8 mm for robot 2).

errors between the actual system and pre-calibrated system of 14.0 mm for robot 1 and 28.9 mm for robot 2 for this configuration, and represents a relative error of 0.6% and 1.0%, respectively, when normalized by the total robot backbone lengths (98.2 mm for robot 1 and 111.8 mm for robot 2). The before and after results of this calibration can be seen in Fig. 5.20, and this calibration was performed with 500 collisions and ran for 14 iterations.

Performing a Calibration with 10 Parameters using Round-trip Distance ($s_1 + s_2$)

Ultimately, our goal is to perform a system calibration using collisions by employing an electrical resistance measurement to record the arc length distance to the collision. Because an electrical resistance measurement at the collision point will only give us the total arc length from the base of robot 1 to the base of robot 2, we tested the calibration routine using a single output measurement ($s_1 + s_2$) for each collision to ensure that we could still obtain an accurate calibration. In addition to only measuring $s_1 + s_2$, we also added more noise into our measurement to account for the expected uncertainty in electrical resistance measurements by injecting Gaussian noise with a 6 mm standard deviation into the measurement of $s_1 + s_2$. The results of the calibration study for 10 parameters using

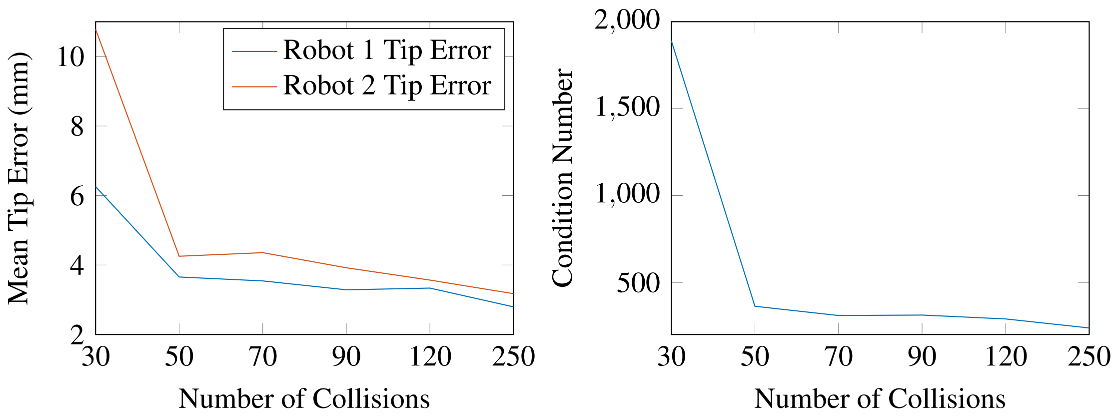

Figure 5.21: The calibrated norm tip error of robot 1 and robot 2 and the condition number of the regressor matrix is shown on the left and right, respectively, for the 10 parameter calibration using $s_1 + s_2$ as the output measurement. For each group of collisions, we ran the simulation 25 times and took the mean of the norm tip error, which is what we report here.

the measurement of $s_1 + s_2$ are shown in Fig. 5.21 and the best calibration we obtained resulted in a 0.38 mm tip error of robot 1 between the actual system and post-calibrated system and a 0.87 mm tip error of robot 2 between the actual system and post-calibrated system (see Fig. 5.22). This is an improvement over the original tip errors between the actual system and pre-calibrated system of 2.2 mm for robot 1 and 17.9 mm for robot 2 for this configuration, and represents a relative error of 0.6% and 0.9%, respectively, when normalized by the total robot backbone lengths (98.6 mm for robot 1 and 116.6 mm for robot 2). It should be noted that using $s_1 + s_2$ increased the number of collisions required, as each collision now provides less information for the calibration. The above calibration was achieved using 250 collisions and ran for 10 iterations.

5.7 Discussion

The high incidence of skull base tumors and the invasiveness of traditional transcranial and transfacial approaches provides strong medical motivation for an endonasal approach. The constrained nasal access path through which multiple rigid manual instruments must work makes the manual procedure challenging even for expert surgeons and time intensive

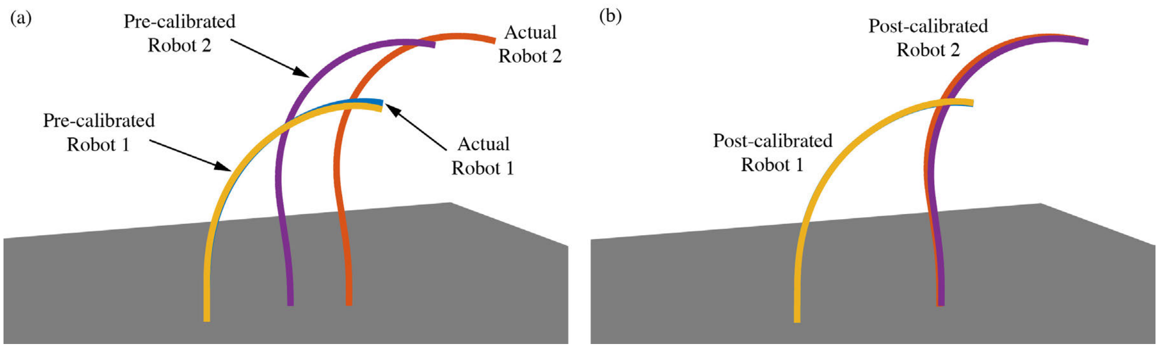

Figure 5.22: (a) This is an example configuration of the actual and pre-calibrated systems using $s_1 + s_2$ as the output measurement. The norm error between the tips of the actual and pre-calibrated robots is 2.2 mm for robot 1 and 17.9 mm for robot 2. (b) This shows the same configuration, but with the post-calibrated system plotted over the actual system. The norm error between the tips of the actual and post-calibrated robots is 0.38 mm for robot 1 and 0.87 mm for robot 2. This corresponds to relative errors of 0.6% and 0.9%, respectively, when normalized by the total robot backbone lengths for this configuration (98.6 mm for robot 1 and 116.6 mm for robot 2).

to learn, motivating a robotic approach. In this chapter, we set out to create a robotic system for endonasal skull base surgery that provided surgeons with dexterous, needle-sized surgical tools at the surgical site. The system presented herein accomplishes this goal, and is straightforward to operate while enabling removal of clinically relevant amounts of tumor. The system offers the promise of reaching locations inaccessible to straight tools and reduces the surgical complexity of the procedure by offloading some of the mental burden on the robotic system.

The requirements of the surgical environment (sterility, ease of use, safety, compactness, etc.) place stringent design requirements on continuum robot actuation systems. While we have designed robots for sterilizability, ease of use, and safety [188], the bimanual and quadramanual systems presented here were not designed with these considerations in mind. A design that considers these topics, along with a simple interface for quickly changing out tools, is in the process of being published. Examples do exist though of medical continuum robots designed with these considerations in mind, including a design that uses multiple backbones which can be actuated in both tension and compression. A compact actuation unit based on miniature DC motors and lead screws was designed to actuate the backbones [23]. This robot was designed for bimanual throat surgery, and a similar device has been constructed for bimanual single port abdominal surgery [207].

The phantom tumor removal results presented in this chapter demonstrate that our robotic endonasal system can provide many of the benefits of robotic surgery to endonasal pituitary tumor resection. In comparison with previous results [208], the addition of the robotic curette that allowed for axial rotation of the curette at the end of the robot enabled a shorter procedure duration and increased the average removal percentage. In this work, the average removal time of 12.5 minutes is clinically reasonable, and when taken in the context of the total time the surgeon spends operating during transnasal pituitary removal (average operating time of 117 minutes), it is a small percentage of the total time [209]. The removal data also suggests the presence of a short learning curve, demonstrated by the increased completion time needed in the first few trials. The 80% average tumor removal is a successful outcome and is comparable with current resection rates. In one study, the average volume reduction of the tumor following transnasal pituitary tumor resection was found to be 86% [210]. While this is higher than the average removal shown with our system, we note that our results are conservative because the experiment did not replicate the effects of hydrostatic pressure in the head, which in live patients exerts a force on the back of the tumor, tending to aid in removal.

Using methods similar to those previously presented [211], we are also interested in preventing unwanted tool collisions as well as collisions with bone or other critical anatomical structures, thus reducing some of the mental burden currently required by the surgeon when manipulating multiple tools through a single nostril. While preventing tool collisions is often viewed as a good thing, we have also presented the idea that system calibration using collisions could be useful to robotic surgical systems such as our endonasal robot. This work lays the foundation for further research into exploiting collisions to provide an accurate calibration to the overall system.

Toward this end, performing calibration via collisions, as presented above, on physical hardware would be beneficial to the project. One approach to performing calibration using collisions is to construct a circuit that measures the electrical resistivity of the tubes in order to record the total arc length along each robot backbone to a collision point. As shown in Sec. 5.6.3, calibration using collisions is able to be performed using the total arc length along each robot backbone to the collision point. Another calibration approach using collisions is to determine the exact moment when the robot arms collide and use statistical estimation to infer the current model shape of the robots and the most likely location of the collision point and arc lengths [212]. Rather than relying on electrical resistivity to measure the arc lengths (which could be noisy), this approach uses the certainty provided by a physical collision coupled with statistical estimation to obtain the arc lengths along the robot backbones to the collision point. Ultimately, the ability to calibrate concentric tube robot systems will play an important role in the success of these systems in the operating room.

Although this work focused on a robotic endonasal skull base system, there are also many other potential surgical applications for a teleoperated robotic device with dexterous needle-diameter manipulators, including the middle ear, throat, other neural spaces besides the skull base, and even in fetal surgery. Additionally, abdominal incisions less that 3 mm in diameter typically heal with no visible scarring whatsoever, meaning a concentric tube robot could essentially provide a “scar-less” surgical approach. The system presented in this work provides surgeons with dexterous, needle-sized surgical tools that are straightforward to operate and offload some of the mental burden onto the robotic system, reducing the surgical complexity of the procedure. Such a system provides patients with an alternative to the invasive surgical approaches that are often the only available option today.

Chapter 6

Future Work and Conclusions

This dissertation develops needle-sized dexterous mechanisms that combine flexures, geometry, and mechanics to enhance the dexterity of new minimally-invasive surgical robotic systems. The clinical challenges that motivated this work include accessing suspicious nodules deep within the lung through a transoral approach and enabling robotic transnasal skull base surgery to bring the benefits of robotic surgery to this difficult to reach location in the head. These novel minimally-invasive surgical systems together with the distal dexterity mechanisms provide the surgeon with new capabilities and access to previously unreachable locations in the body. Ultimately, it is hoped that the work presented here will one day benefit patients in the operating room. The chief contributions of this work are summarized below.

Design

In this dissertation, the basic concepts of mechanics and geometry are coupled to design novel distal dexterity mechanisms. Design examples found in this work are:

- A steerable needle that incorporates a flexure element located between the needle tip and shaft to provide high curvature and reduced tissue damage (Chapter 2, [6])
- A miniature wrist that is integrated into an elastic tube and uses cutout sections of tube to decrease bending stiffness and create a dexterous device (Chapter 3, [58])
- A non-annular concentric tube robot that uses geometry to enable previously unreachable robot configurations and prevent elastic instability (Chapter 4, [59])

Modeling

Kinematic and mechanics-based models that describe the behavior of the distal dexterity mechanisms are presented in this dissertation. They are:

- A model that describes the behavior of the flexure-tip needle and its trajectory through tissue (Chapter 2, [60])
- A model that incorporates the geometry of the wrist and describes the kinematic motion of the wrist as well as the forces required to actuate the wrist (Chapter 3, [58])

Systems

The distal dexterity mechanisms are then incorporated into two surgical robotic systems in this dissertation. They are:

- A system that provides transoral access to challenging or impossible to reach locations in the lung for biopsy of suspicious nodules (Chapter 4, [61])
- A system that enables a minimally-invasive robotic approach to endonasal tumor removal and delivers four concentric tube robot arms through a single nostril to the skull base under teleoperated surgeon control (Chapter 5, [62])

6.1 Future Work in Design and Modeling of Dexterous Mechanisms

The integration of flexures with needle-sized instruments through the informed use of geometry and mechanics enables new and dexterous devices to be created. These new minimally-invasive, dexterous surgical tools are able to operate in previously unreachable locations within the body. There are many avenues of future work for both of the dexterous mechanisms presented in this work. With regard to the flexure-tip steerable needle presented in Chapter 2, the next step in the evolution of the device is optimal design of the flexure joint for specific tissues and locations within the body. There are several parameters that need tuned (most notably flexure stiffness, but also shaft stiffness, bevel angle, etc.) to the desired tissue medium. While the flexure joint is presently designed such that the needle must be tuned to match the tissue properties, future investigation could yield a method for varying the stiffness of the flexure joint in real time to match the tissue as well.

One possible approach to achieving this type of control is to employ the cutout flexure-tip needle design presented in Sec. 2.6 and use a tendon attached to the bevel tip to actuate the flexure joint. A robotic system could be used to perform active stiffness control of the flexure joint with this design, potentially removing the need to tune the needle to the tissue. Further study into the tissue damage caused by steerable needles would also be beneficial to the research community. While the initial anecdotal phantom tissue histological images provided in Chapter 2 show little apparent tissue damage caused by the flexure-tip steerable needle, more in-depth histological evaluations in living biological tissues such as those performed in [7] are needed to quantitatively verify reduced tissue damage. It will also be useful to verify that the tissue damage incurred by these needle tip designs (including the kinked bevel-tip needle) is clinically significant.

Toward clinical adoption of the flexure-tip needle for error correction, the next step is to clinically validate the use of a guide sheath for delivering treatment. While the initial concept was shown in Chapter 4, a more rigorous experimental study of targeted insertions into realistic tissue and the use of a guide sheath for biopsy or therapy delivery would be beneficial to the project and the entire needle steering community. Lastly, additional study into the manual use of flexure-tip steerable needles would aid the commercialization and clinical adoption of the technology. Topics of investigation include handle design such that coupled rotation and insertion of the steerable needle is ergonomic and intuitive, the use of a tendon for active control of the flexure joint as discussed above, and targeting experiments with animal tissue under fluoroscopic guidance. The needle-sized wrist presented in Chapter 3 also has many opportunities for continued development.

Design choices for the needle-sized wrist provide ample opportunity for optimization with respect to specific clinical applications or tool requirements. The use of varying cut heights shown in Chapter 3 to achieve tip-first bending of the device is but one example of such an optimization. Changing the geometric shape and positioning of the cutouts will result in different performance of the device. One could investigate rotating the cutouts around the wrist to achieve a helical bending shape, placing the cutouts on two opposing sides of the tube to create a device that bends in an s-shape, or the use of non-rectangular cutouts [101]. Due to the high strains experienced in the wrist and the large deformations, the development of a more detailed mechanics model that accounts for material deformation (buckling) of the cutout regions of the tube may improve the accuracy of the model. One possible approach to modeling the material deformation of the wrist is to use finite element modeling. Although nitinol is nonlinear, some work has been done toward modeling it using finite element models [213]. Another interesting study would be a comparison of existing needle-sized surgical tools with the dexterous wrist for a particular clinical application. In such a comparison, the dexterous wrist could also be optimized for the required workspace anatomy and force/stiffness requirements of the procedure.

Regarding the use of the dexterous wrist with a concentric tube robot, the system now has redundant degrees of freedom that can be used to accomplish a secondary task such as obstacle avoidance. Additionally, when the wrist is directly integrated into the inner-most concentric tube in a robotic system such as the system presented in Chapter 5, coupling exists between actuation of the wrist and movement of the robot such that care must be taken if the wrist is to be actuated while leaving the tip of the robot stationary. Investigation into how best to use the redundant degrees of freedom of the system and the self-motion capabilities of wristed concentric tube robots is another great avenue for future work. In addition to these future developments for the flexure-tip steerable needle and the miniature wrist, the robotic systems presented in Chapters 4 and 5 also have opportunities for further study.

6.2 Future Work in Systems to Treat Lung and Brain Cancer

The next major study using the robotic transoral lung system presented in Chapter 4 is already underway, and it involves the integration of the system with an existing image-guidance system and testing with more anatomically realistic tissue [79]. Preliminary results are promising, with the system able to achieve less than 2 mm targeting error in inflated, ex vivo porcine lung using a motion planner for obstacle avoidance [79]. Further experiments will be necessary, including the use of perfused tissue and respiratory motion. The use of perfused porcine tissue will allow the flexure-tip steerable needle to be optimized for lung parenchyma. This is likely to result in a larger achievable workspace for the needle, thus enabling more complex motion planning problems to be investigated [140, 141]. Methods to compensate for respiratory motion using the robotic lung system should also be developed, as the system is ultimately intended for use on patients who are breathing on their own. Breathing compensation could be addressed with a robotic actuation mechanism that monitors the patient's chest and moves the entire system such that it is in sync with the chest wall. Another approach is to only advance the system when the patient is in a breath hold, essentially removing the effect of respiratory motion.

Another open area of research for the lung system involves optimizing the design of concentric tube robots based on anatomical constraints. There is a large design space available to concentric tube robots, and work is being done to answer the challenging question of optimal tube design [141, 187, 214, 215]. A critical avenue for future work with respect to the robotic lung system is the development of a new actuation unit. The current actuation unit was not designed with compactness in mind. The next version of the robotic actuation unit should be reduced in size such that it can be easily managed by the physician in the operating room. Although it is envisioned that the physician will deploy the bronchoscope manually in the system workflow, it may be useful to investigate roboticizing bronchoscope deployment in the future (see e.g. [43]), particularly if a robotic system can maneuver the scope more accurately and reliably than a human. However, it will likely be desirable from a clinical adoption and cost standpoint to rely solely on manual deployment which will minimally impact the established workflow of bronchoscopy. It is also worth noting that our system could be used in conjunction with virtual bronchoscopy [124] to assist the physician with manually navigating the bronchial tree, and this integration would be a worthwhile avenue of future research.

The robotic endonasal system developed in Chapter 5 also presents a number of areas for continued investigation, and some of these avenues are currently underway. First, a new actuation unit has been designed and is currently being assembled that considers the requirements of an operating room such as sterility and compactness. While we have designed robots for sterility and safety in the past [188], the new system must also consider interchangeability of the tools, positioning of the robot over the patient, and redundant sensing in the event of an emergency. These aspects will need to be integrated with the next version of the actuation unit. Another avenue for future work that would benefit not only our system but also any systems or tools developed for the skull base is the investigation of forces encountered during skull base procedures. In [148], we performed a preliminary study to look at the forces experienced by a surgical curette during endonasal pituitary tumor removal. An extension of this study could collect similar data for additional pituitary removal cases or investigate tool tip forces during various other endonasal procedures. Additionally, investigating the forces required to break different bony structures using cadaveric specimens would be useful. Such force information provides maximum limits for force application which can then be integrated into a robotic system such as ours or could be used for training the next generation of surgeons.

If this testing reveals that some areas of the skull base are sensitive to anatomical variation such that a safe operating threshold cannot be developed, the implementation of collision avoidance algorithms [211] or “no-fly zones” [216] can be integrated with the robotic system. There are also many open questions with regards to the optimal user interface for continuum robots. While touchless user interfaces have been shown to be one possibility for use with the robotic endonasal system [217], many other approaches and interfaces can be imagined, and a thorough investigation into the optimal user interface for continuum robots would be valuable. Experimentally, the next steps for the endonasal system are to conduct more rigorous cadaver studies using the newly designed quadramanual actuation unit with suction provided through one of the arms, allowing for complete removal of pituitary tumors with the system. While performing cadaver studies, it will also be useful to investigate robust calibration methods for use during a procedure, in addition to calibration of the system before beginning the operation. Toward this end, it would be good to investigate calibration using collisions on physical hardware using the new quadramanual system. In order to generate collisions on physical hardware, the same resolved-rates method used in Sec. 5.6.3 can be used, or the collisions can be induced by a user teleoperating the system. One approach to performing calibration using collisions is to construct a circuit that measures the electrical resistivity of the tubes in order to record the total arc length along each robot backbone to a collision point. As shown in Sec. 5.6.3, calibration is able to be performed using the total arc length along each robot backbone to the collision point. Another calibration approach using collisions is to determine the exact moment when the robot arms collide and use statistical estimation to infer the current model shape of the robots and the most likely location of the collision point and arc lengths [212]. Rather than relying on electrical resistivity to measure the arc lengths (which could be noisy), this approach uses the certainty provided by a physical collision coupled with statistical estimation to obtain the arc lengths along the robot backbones to the collision point. In the course of these experiments, calibration using collisions can be investigated in the presence of actuator uncertainty and uncertainty in the initial configuration of the robot. Finally, a more robust calibration can be generated by incorporating a priori parameter estimates [204].

6.3 Conclusion

In conclusion, the central objective in this dissertation is the use of mechanics and geometry to inform the design of novel, less invasive, surgical robots and tools. In this work, two dexterous needle-sized devices are developed and modeled using these principles, providing new capabilities to needle-sized surgical tools. The newly developed tools can then be integrated with surgical robotic systems, such as the robotic systems developed in this work for minimally-invasive treatment of lung and skull base cancers. The goal in developing these dexterous mechanisms and surgical robotic systems is to provide physicians with better minimally-invasive tools and systems in order to improve the treatment of their patients. As minimally-invasive surgery continues to redefine itself through the use of smaller and smaller incisions (and even natural orifices), highly dexterous surgical instruments and robots will almost certainly play an increasingly prominent role in the operating room. Though it remains to be seen what clinical applications will benefit the most from dexterous surgical tools such as concentric tube robots and steerable needles, it seems apparent that the operating room of the future will be quite different from the operating room of today.

BIBLIOGRAPHY

[1] E. Ayvali, C.-P. Liang, M. Ho, Y. Chen, and J. P. Desai. Towards a discretely actuated steerable cannula for diagnostic and therapeutic procedures. *International Journal of Robotics Research*, 31(5):588–603, 2012.

[2] N. J. van de Berg, J. Dankelman, and J. J. van den Dobbelsteen. Design of an actively controlled steerable needle with tendon actuation and fbg-based shape sensing. *Medical Engineering & Physics*, 37(6):617–622, 2015.

[3] Osseon. Osseoflex sn steerable needle, 2015.

[4] L. B. Kratchman, M. M. Rahman, J. R. Saunders, P. J. Swaney, and R. J. Webster III. Toward robotic needle steering in lung biopsy: a tendon-actuated approach. In *SPIE Medical Imaging*, pages 79641I–79641I. International Society for Optics and Photonics, 2011.

[5] N. Chentanez, R. Alterovitz, D. Ritchie, L. Cho, K. K. Hauser, K. Goldberg, J. R. Shewchuk, and J. F. O'Brien. Interactive Simulation of Surgical Needle Insertion and Steering. *ACM SIGGRAPH*, 28(3):1–10, 2009.

[6] P. J. Swaney, J. Burgner, H. B. Gilbert, and R. J. Webster III. A flexure-based steerable needle: high curvature with reduced tissue damage. *IEEE Transactions on Biomedical Engineering*, 60:906–909, 2013.

[7] A. Majewicz, S. Marra, M. van Vledder, M. Lin, M. Choti, D. Song, and A. Okamura. Behavior of tip-steerable needles in ex vivo and in vivo tissue. *IEEE Transactions on Biomedical Engineering*, 59(10):2705–2715, 2012.

[8] J. Arata, Y. Saito, and H. Fujimoto. Outer shell type 2 dof bending manipulator using spring-link mechanism for medical applications. In *IEEE International Conference on Robotics and Automation*, pages 1041–1046, 2010.

[9] P. Breedveld. Steerable laparoscopic cable-ring forceps. *Journal of Medical Devices*, 4(2):027518, 2010.

[10] H. Fischer, B. Vogel, W. Pfleging, and H. Besser. Flexible distal tip made of nitinol (NiTi) for a steerable endoscopic camera system. *Materials Science and Engineering: A*, 273:780–783, 1999.

[11] C. J. Walsh, N. C. Hanumara, A. H. Slocum, J.-A. Shepard, and R. Gupta. A patient-mounted, telerobotic tool for ct-guided percutaneous interventions. *Journal of Medical Devices*, 2(1):011007, 2008.

[12] E. Y. Hanna, C. Holsinger, F. DeMonte, and M. Kupferman. Robotic endoscopic surgery of the skull base: a novel surgical approach. *Archives of Otolaryngology–Head & Neck Surgery*, 133(12):1209–1214, 2007.

[13] P. Schuler, M. Scheithauer, N. Rotter, J. Veit, U. Duvvuri, and T. Hoffmann. A single-port operator-controlled flexible endoscope system for endoscopic skull base surgery. *HNO*, 63(3):189–194, 2015.

[14] P. J. Swaney, J. M. Croom, J. Burgner, H. B. Gilbert, D. C. Rucker, P. T. Russell III, K. D. Weaver, and R. J. Webster III. Design of a quadramanual robot for single-nostril skull base surgery. In *ASME Dynamic Systems and Control Conference*, pages 387–393, 2012.

[15] Y. S. Kwoh, J. Hou, E. A. Jonckheere, and S. Hayati. A robot with improved absolute positioning accuracy for CT guided stereotactic brain surgery. *IEEE Transactions on Biomedical Engineering*, 35(2):153–160, 1988.

[16] A. P. Schulz, K. Seide, C. Queitsch, A. von Haugwitz, J. Meiners, B. Kienast, M. Tarabolsi, M. Kammal, and C. Jürgens. Results of total hip replacement using the robodoc surgical assistant system: clinical outcome and evaluation of complications

for 97 procedures. *The International Journal of Medical Robotics and Computer Assisted Surgery*, 3(4):301–306, 2007.

[17] T. Varma, P. Eldridge, A. Forster, S. Fox, N. Fletcher, M. Steiger, P. Littlechild, P. Byrne, A. Sinnott, K. Tyler, et al. Use of the neuromate stereotactic robot in a frameless mode for movement disorder surgery. *Stereotactic and Functional Neurosurgery*, 80(1-4):132–135, 2003.

[18] V. Y. Reddy, P. Neuzil, Z. J. Malchano, R. Vijaykumar, R. Cury, S. Abbara, J. Weichet, C. D. McPherson, and J. N. Ruskin. View-synchronized robotic image-guided therapy for atrial fibrillation ablation experimental validation and clinical feasibility. *Circulation*, 115(21):2705–2714, 2007.

[19] M. Stark, T. Benhidjeb, S. Gidaro, and E. R. Morales. The future of telesurgery: a universal system with haptic sensation. *Journal of the Turkish German Gynecological Association*, 13(1):74, 2012.

[20] J.-U. Stolzenburg, T. Franz, P. Kallidonis, D. Minh, A. Dietel, J. Hicks, M. Nicolaus, A. Al-Aown, and E. Liatsikos. Comparison of the freehand® robotic camera holder with human assistants during endoscopic extraperitoneal radical prostatectomy. *BJU International*, 107(6):970–974, 2011.

[21] J. Bodner, H. Wykypiel, G. Wetscher, and T. Schmid. First experiences with the da vinci™ operating robot in thoracic surgery. *European Journal of Cardio-thoracic Surgery*, 25(5):844–851, 2004.

[22] D. Herron, M. Marohn, et al. A consensus document on robotic surgery. *Surgical Endoscopy*, 22(2):313–325, 2008.

[23] S. Hamid and N. Simaan. Design and synthesis of wire-actuated universal-joint wrists for surgical applications. In *IEEE International Conference on Robotics and Automation*, pages 1807–1813, 2009.

[24] P. Dario, C. Paggetti, N. Troisfontaine, E. Papa, T. Ciucci, M. C. Carrozza, and M. Marcacci. A miniature steerable end-effector for application in an integrated system for computer-assisted arthroscopy. In *IEEE International Conference on Robotics and Automation*, pages 1573–1579, 1997.

[25] J. Peirs, D. Reynaerts, H. Van Brussel, and G. De Gersem. Design of an Advanced Tool Guiding System for Robotic Surgery. In *IEEE International Conference on Robotics and Automation*, pages 2651–2656, 2003.

[26] N. Simaan, K. Xu, W. Wei, A. Kapoor, P. Kazanzides, P. Flint, and R. Taylor. Design and integration of a telerobotic system for minimally invasive surgery of the throat. *International Journal of Robotics Research*, 28:1134–1153, 2009.

[27] J. Ding, R. Goldman, K. Xu, P. Allen, D. Fowler, and N. Simaan. Design and coordination kinematics of an insertable robotic effectors platform for single-port access surgery. *IEEE/ASME Transactions on Mechatronics*, 18(5):1612–1624, 2013.

[28] T. Ota, A. Degani, D. Schwartzman, B. Zubiate, J. McGarvey, H. Choset, and M. A. Zenati. A highly articulated robotic surgical system for minimally invasive surgery. *The Annals of Thoracic Surgery*, 87(4):1253–1256, 2009.

[29] M. Mandapathil, U. Duvvuri, C. Güldner, A. Teymoortash, G. Lawson, and J. A. Werner. Transoral surgery for oropharyngeal tumors using the medrobotics® flex® system–a case report. *International Journal of Surgery Case Reports*, 10:173–175, 2015.

[30] N. V. Datla, B. Konh, M. Honarvar, T. K. Podder, A. P. Dicker, Y. Yu, and P. Hutapea. A model to predict deflection of bevel-tipped active needle advancing in soft tissue. *Medical Engineering & Physics*, 36(3):285–293, 2014.

[31] L. Frasson, S. Ko, A. Turner, T. Parittotokkaporn, J. F. Vincent, and F. R. y Baena. Sting: a soft-tissue intervention and neurosurgical guide to access deep brain lesions

through curved trajectories. *Proceedings of the Institution of Mechanical Engineers, Part H: Journal of Engineering in Medicine*, 224(6):775–788, 2010.

[32] R. J. Webster III, J. S. Kim, N. J. Cowan, G. S. Chirikjian, and A. M. Okamura. Nonholonomic modeling of needle steering. *International Journal of Robotics Research*, 25(5-6):509–525, 2006.

[33] S. Misra, K. B. Reed, A. S. Douglas, K. Ramesh, and A. M. Okamura. Needle-tissue interaction forces for bevel-tip steerable needles. In *IEEE RAS & EMBS International Conference on Biomedical Robotics and Biomechatronics*, pages 224–231, 2008.

[34] W. Assaad, A. Jahya, P. Moreira, and S. Misra. Finite-element modeling of a bevel-tipped needle interacting with gel. *Journal of Mechanics in Medicine and Biology*, 15(05):1550079, 2015.

[35] K. B. Reed, A. M. Okamura, and N. J. Cowan. Modeling and control of needles with torsional friction. *IEEE Transactions on Biomedical Engineering*, 56(12):2905–2916, 2009.

[36] J. P. Swensen, M. Lin, A. M. Okamura, and N. J. Cowan. Torsional dynamics of steerable needles: modeling and fluoroscopic guidance. *IEEE Transactions on Biomedical Engineering*, 61(11):2707–2717, 2014.

[37] T. Wedlick and A. Okamura. Characterization of pre-curved needles for steering in tissue. In *Annual International Conference of the IEEE Engineering in Medicine and Biology Society*, pages 1200 –1203, 2009.

[38] F. Jelínek, E. A. Arkenbout, P. W. J. Henselmans, R. Pessers, and P. Breedveld. Classification of joints used in steerable instruments for minimally invasive surgery–a review of the state of the art. *Journal of Medical Devices*, 9(1):010801–1 –010801–11, 2015.

[39] J. Catherine, C. Rotinat-Libersa, and A. Micaelli. Comparative review of endoscopic devices articulations technologies developed for minimally invasive medical procedures. *Applied Bionics and Biomechanics*, 8(2):151–171, 2011.

[40] N. Simaan. Snake-like units using flexible backbones and actuation redundancy for enhanced miniaturization. In *IEEE International Conference on Robotics and Automation*, pages 3012–3017, 2005.

[41] J. Peirs, H. Van Brussel, D. Reynaerts, and G. De Gersem. A flexible distal tip with two degrees of freedom for enhanced dexterity in endoscopic robot surgery. In *Proceedings of the 13th Micromechanics Europe Workshop*, pages 271–274, 2002.

[42] D. B. Camarillo, C. F. Milne, C. R. Carlson, M. R. Zinn, and J. K. Salisbury. Mechanics modeling of tendon-driven continuum manipulators. *IEEE Transactions on Robotics*, 24(6):1262–1273, 2008.

[43] R. J. Webster III and B. A. Jones. Design and kinematic modeling of constant curvature continuum robots: a review. *International Journal of Robotics Research*, 29(13):1661–1683, 2010.

[44] Y. Bailly, Y. Amirat, and G. Fried. Modeling and control of a continuum style microrobot for endovascular surgery. *IEEE Transactions on Robotics*, 27(5):1024–1030, 2011.

[45] M. D. M. Kutzer, S. M. Segreti, C. Y. Brown, M. Armand, R. H. Taylor, and S. C. Mears. Design of a new cable-driven manipulator with a large open lumen: preliminary applications in the minimally-invasive removal of osteolysis. In *IEEE International Conference on Robotics and Automation*, pages 2913–2920, 2011.

[46] Y. Haga, Y. Muyari, S. Goto, T. Matsunaga, and M. Esashi. Development of minimally invasive medical tools using laser processing on cylindrical substrates. *Electrical Engineering in Japan*, 176(1):65–74, 2011.

[47] J. A. Bell, C. E. Saikus, K. Ratnayaka, V. Wu, M. Sonmez, A. Z. Faranesh, J. H. Colyer, R. J. Lederman, and O. Kocaturk. A deflectable guiding catheter for real-time mri-guided interventions. *Journal of Magnetic Resonance Imaging*, 35(4):908–915, 2012.

[48] American Cancer Society. Cancer facts & figures 2014. Technical report, American Cancer Society, 2014.

[49] W. T. Brown, X. Wu, F. Fayad, J. F. Fowler, B. E. Amendola, S. García, H. Han, A. de la Zerda, E. Bossart, Z. Huang, et al. Cyberknife® radiosurgery for stage I lung cancer: results at 36 months. *Clinical Lung Cancer*, 8(8):488–492, 2007.

[50] E. Yu, C. Lewis, A. Luisa Trejos, R. V Patel, and R. A Malthaner. Lung cancer brachytherapy: robotics-assisted minimally invasive approach. *Current Respiratory Medicine Reviews*, 7(5):340–353, 2011.

[51] SuperDimension. SuperDimension i-Logic System. Available: http://www.superdimension.com, 2010.

[52] Veran Medical Technologies. SPiN Drive, 2012.

[53] Y. Zhou, K. Thiruvalluvan, L. Krzeminski, W. H. Moore, Z. Xu, and Z. Liang. Ct-guided robotic needle biopsy of lung nodules with respiratory motion–experimental system and preliminary test. *The International Journal of Medical Robotics and Computer Assisted Surgery*, 9(3):317–330, 2013.

[54] ABTA. “American Brain Tumor Association”. From http://abta.org, Accessed 2011.

[55] C. Nimsky, J. Rachinger, H. Iro, and R. Fahlbusch. Adaptation of a hexapod-based robotic system for extended endoscope-assisted transsphenoidal skull base surgery. *Minimally Invasive Neurosurgery*, 47(1):41–6, 2004.

[56] C.-A. O. Nathan, V. Chakradeo, K. Malhotra, H. D'Agostino, and R. Patwardhan. The voice-controlled robotic assist scope holder aesop for the endoscopic approach to the sella. *Skull Base*, 16(3):123, 2006.

[57] K. Eichhorn and F. Bootz. Clinical requirements and possible applications of robot assisted endoscopy in skull base and sinus surgery. *Intraoperative Imaging, Acta Neurochirurgica Supplementum*, 109:237–240, 2011.

[58] P. J. Swaney, P. A. York, H. B. Gilbert, J. Burgner-Kahrs, and R. J. Webster III. Design, fabrication, and testing of a needle-sized wrist for surgical instruments. *ASME Journal of Medical Devices*, 2016. In Review.

[59] P. J. Swaney, H. B. Gilbert, R. J. Hendrick, O. Commichau, R. Alterovitz, and R. J. Webster III. Transoral Steerable Needles in The Lung: How Non-Annular Concentric Tube Robots Can Improve Targeting. In *Hamlyn Symposium on Medical Robotics*, 2015.

[60] A. W. Mahoney, P. J. Swaney, A. A. Remirez, and R. J. Webster III. Kinematics of a flexure-tip steerable needle. *IEEE Transactions on Robotics*, 2016. In Preparation.

[61] P. J. Swaney, A. W. Mahoney, A. A. Remirez, E. P. Lamers, B. I. Hartley, R. H. Feins, R. Alterovitz, and R. J. Webster III. Toward transoral peripheral lung access: combining continuum robots and steerable needles. *Journal of Medical Robotics Research*, 2016. In Press.

[62] P. J. Swaney, H. B. Gilbert, R. J. Webster III, P. T. Russell III, and K. D. Weaver. Endonasal Skull Base Tumor Removal Using Concentric Tube Continuum Robots: A Phantom Study. *Journal of Neurological Surgery Part B: Skull Base*, 76(2):145–149, 2015.

[63] N. Abolhassani, R. Patel, and M. Moallem. Needle insertion into soft tissue: A survey. *Medical Engineering & Physics*, 29(4):413–31, 2007.

[64] J. Engh, G. Podnar, D. Kondziolka, and C. Riviere. Toward effective needle steering in brain tissue. *Annual International Conference of the IEEE Engineering in Medicine and Biology Society*, pages 559 –562, 2006.

[65] J. Xu, V. Duindam, R. Alterovitz, J. Pouliot, J. Cunha, I.-C. Hsu, and K. Goldberg. Planning "fireworks" trajectories for steerable medical needles to reduce patient trauma. In *IEEE/RSJ International Conference on Intelligent Robots and Systems*, pages 4517–4522, 2009.

[66] K. Reed, A. Majewicz, V. Kallem, R. Alterovitz, K. Goldberg, N. Cowan, and A. Okamura. Robot-assisted needle steering. *IEEE Robotics & Automation Magazine*, 18(4):35 –46, 2011.

[67] V. Kallem and N. Cowan. Image guidance of flexible tip-steerable needles. *IEEE Transactions on Robotics*, 25(1):191 –196, 2009.

[68] A. Asadian, M. Kermani, and R. Patel. Robot-assisted needle steering using a control theoretic approach. *Journal of Intelligent & Robotic Systems*, 62:397–418, 2011.

[69] R. Alterovitz, M. Branicky, and K. Goldberg. Motion planning under uncertainty for image-guided medical needle steering. *International Journal of Robotics Research*, pages 1361–1374, 2008.

[70] S. Misra, K. B. Reed, B. W. Schafer, K. T. Ramesh, and A. M. Okamura. Mechanics of flexible needles robotically steered through soft tissue. *International Journal of Robotics Research*, 29(13):1640–1660, 2010.

[71] A. Asadian, M. Kermani, and R. Patel. A novel force modeling scheme for needle insertion using multiple Kalman filters. *IEEE Transactions on Instrumentation and Measurement*, 61(2):429 –438, 2012.

[72] D. S. Minhas, J. A. Engh, M. M. Fenske, and C. N. Riviere. Modeling of needle steering via duty-cycled spinning. In *Annual International Conference of the IEEE Engineering in Medicine and Biology Society*, pages 2756–2759, 2007.

[73] R. J. Webster III, J. S. Kim, N. J. Cowan, G. S. Chirikjian, and A. M. Okamura. Nonholonomic Modeling of Needle Steering. *International Journal of Robotics Research*, 25(5-6):509–525, 2006.

[74] S. Okazawa, R. Ebrahimi, J. Chuang, S. Salcudean, and R. Rohling. Hand-held steerable needle device. *IEEE/ASME Transactions on Mechatronics*, 10(3):285–296, 2005.

[75] L. Frasson, S. Y. Ko, A. Turner, T. Parittotokkaporn, J. F. Vincent, and F. Rodriguez y Baena. Sting: a soft-tissue intervention and neurosurgical guide to access deep brain lesions through curved trajectories. *Proceedings of the Institution of Mechanical Engineers, Part H: Journal of Engineering in Medicine*, 224(6):775–788, 2010.

[76] R. J. Webster III, J. Memisevic, and A. M. Okamura. Design considerations for robotic needle steering. In *IEEE International Conference on Robotics and Automation*, pages 3599–3605, 2005.

[77] P. A. York, P. J. Swaney, H. B. Gilbert, and R. J. Webster III. A wrist for needle-sized surgical robots. In *IEEE International Conference on Robotics and Automation*, pages 1776–1781, 2015.

[78] A. Kuntz, L. G. Torres, R. H. Feins, R. J. Webster III, and R. Alterovitz. Motion planning for a three-stage multilumen transoral lung access system. In *IEEE/RSJ International Conference on Intelligent Robots and Systems*, pages 3255–3261, 2015.

[79] A. Kuntz, P. J. Swaney, A. W. Mahoney, R. H. Feins, Y. Z. Lee, R. J. Webster III, and R. Alterovitz. Toward transoral peripheral lung access: steering bronchoscope-

deployed needles through porcine lung tissue. In *Hamlyn Symposium on Medical Robotics*, 2016.

[80] A. R. Aurora and J. L. Ponsky. Future perspectives on scarless surgery: where we have been and where we are going. In *Scar-Less Surgery*, pages 341–350. Springer, 2013.

[81] R.-H. Yuan, W.-J. Lee, and S.-C. Yu. Mini-laparoscopic cholecystectomy: a cosmetically better, almost scarless procedure. *Journal of Laparoendoscopic & Advanced Surgical Techniques*, 7(4):205–211, 1997.

[82] C. H. Snyderman, R. L. Carrau, A. B. Kassam, A. Zanation, D. Prevedello, P. Gardner, and A. Mintz. Endoscopic skull base surgery: principles of endonasal oncological surgery. *Journal of Surgical Oncology*, 97(8):658–664, 2008.

[83] M. Badr-el Dine. Value of ear endoscopy in cholesteatoma surgery. *Otology & Neurotology*, 23(5):631–635, 2002.

[84] P. Golanó, J. Vega, L. Pérez-Carro, and V. Götzens. Ankle anatomy for the arthroscopist. part I: The portals. *Foot and Ankle Clinics*, 11(2):253–273, 2006.

[85] P. Berkelman and J. Ma. A compact modular teleoperated robotic system for laparoscopic surgery. *International Journal of Robotics Research*, 28(9):1198–1215, 2009.

[86] J. Shang, D. Noonan, C. Payne, J. Clark, M. H. Sodergren, A. Darzi, and G. Yang. An articulated universal joint based flexible access robot for minimally invasive surgery. In *IEEE International Conference on Robotics and Automation*, pages 1147–1152, 2011.

[87] W.-H. Shin and D.-S. Kwon. Surgical robot system for single-port surgery with

novel joint mechanism. *IEEE Transactions on Biomedical Engineering*, 60(4):937–944, 2013.

[88] B. Zhao and C. A. Nelson. Decoupled cable-driven grasper design based on planetary gear theory. *Journal of Medical Devices*, 7(2):020918, 2013.

[89] F. Jelínek, R. Pessers, and P. Breedveld. Dragonflex–smart steerable laparoscopic instrument. *Journal of Medical Devices*, 7(2):020911, 2013.

[90] C. Ishii and K. Kobayashi. Development of a new bending mechanism and its application to robotic forceps manipulator. In *IEEE International Conference on Robotics and Automation*, pages 238–243, 2007.

[91] F. Hammond, R. Howe, and R. Wood. Dexterous high-precision robotic wrist for micromanipulation. In *International Conference on Advanced Robotics*, pages 1–8, 2013.

[92] M. B. Hong and Y.-H. Jo. Design of a novel 4-dof wrist-type surgical instrument with enhanced rigidity and dexterity. *IEEE/ASME Transactions on Mechatronics*, 19(2):500–511, April 2014.

[93] W. Sieklicki, M. Zoppi, and R. Molfino. Superelastic compliant mechanisms for needlescopic surgical wrists. In *ASME/IFToMM International Conference on Reconfigurable Mechanisms and Robots*, pages 392–399, 2009.

[94] X. He, V. van Geirt, P. Gehlbach, R. Taylor, and I. Iordachita. IRIS: integrated robotic intraocular snake. In *IEEE International Conference on Robotics and Automation*, pages 1764–1769, 2015.

[95] M. S. Moses, M. D. Kutzer, H. Ma, and M. Armand. A continuum manipulator made of interlocking fibers. In *IEEE International Conference on Robotics and Automation*, pages 4008–4015, 2013.

[96] T. Y. Nai, J. L. Herder, and G. J. Tuijthof. Steerable mechanical joint for high load transmission in minimally invasive instruments. *Journal of Medical Devices*, 5(3):034503, 2011.

[97] D. Wei, Y. Wenlong, H. Dawei, and D. Zhijiang. Modeling of flexible arm with triangular notches for applications in single port access abdominal surgery. In *IEEE International Conference on Robotics and Biomimetics*, pages 588–593, 2012.

[98] J. Liu, B. Hall, M. Frecker, and E. W. Reutzel. Compliant articulation structure using superelastic nitinol. *Smart Materials and Structures*, 22(9):094018, 2013.

[99] J.-S. Kim, D.-Y. Lee, K. Kim, S. Kang, and K.-J. Cho. Toward a solution to the snapping problem in a concentric-tube continuum robot: Grooved tubes with anisotropy. In *IEEE International Conference on Robotics and Automation*, pages 5871–5876, 2014.

[100] H. Azimian, P. Francis, T. Looi, and J. Drake. Structurally-redesigned concentric-tube manipulators with improved stability. In *IEEE/RSJ International Conference on Intelligent Robots and Systems*, pages 2030–2035, 2014.

[101] S. C. Ryu, P. Renaud, R. J. Black, B. L. Daniel, and M. R. Cutkosky. Feasibility study of an optically actuated mr-compatible active needle. In *IEEE/RSJ International Conference on Intelligent Robots and Systems*, pages 2564–2569, 2011.

[102] J. Burgner-Kahrs, D. C. Rucker, and H. Choset. Continuum robots for medical applications: A survey. *IEEE Transactions on Robotics*, 31(6):1261–1280, 2015.

[103] D. C. Rucker, B. A. Jones, and R. J. Webster III. A geometrically exact model for externally loaded concentric tube continuum robots. *IEEE Transactions on Robotics*, 26(5):769–780, 2010.

[104] P. E. Dupont, J. Lock, B. Itkowitz, and E. Butler. Design and control of concentric-tube robots. *IEEE Transactions on Robotics*, 26(2):209–225, 2010.

[105] R. J. Hendrick, S. D. Herrell, and R. J. Webster III. A multi-arm hand-held robotic system for transurethral laser prostate surgery. In *IEEE International Conference on Robotics and Automation*, pages 2850–2855, 2014.

[106] A. H. Gosline, N. V. Vasilyev, E. J. Butler, C. Folk, A. Cohen, R. Chen, N. Lang, P. J. Del Nido, and P. E. Dupont. Percutaneous intracardiac beating-heart surgery using metal mems tissue approximation tools. *International Journal of Robotics Research*, 31(9):1081–1093, 2012.

[107] J. Burgner, D. C. Rucker, H. B. Gilbert, P. J. Swaney, P. T. Russell, K. D. Weaver, and R. J. Webster III. A telerobotic system for transnasal surgery. *IEEE Transactions on Mechatronics*, 19(3):996–1006, 2014.

[108] M. Torabi, R. Gupta, and C. J. Walsh. Compact robotically steerable image-guided instrument for multi-adjacent-point (map) targeting. *IEEE Transactions on Robotics*, 30(4):802–815, 2014.

[109] R. J. Webster III and B. A. Jones. Design and kinematic modeling of constant curvature continuum robots: a review. *International Journal of Robotics Research*, 29(13):1661–1683, 2010.

[110] A. Pelton, J. DiCello, and S. Miyazaki. Optimisation of processing and properties of medical grade nitinol wire. *Minimally Invasive Therapies and Allied Technologies*, 9:107–118, 2000.

[111] R. Watkins and J. Shaw. Shape memory alloy column buckling: An experimental study. *ICAST, Palm Beach, Aruba*, 2013.

[112] G. Tan and Y. Liu. Comparative study of deformation-induced martensite stabilisation via martensite reorientation and stress-induced martensitic transformation in niti. *Intermetallics*, 12(4):373–381, 2004.

[113] Memry Corporation. Nitinol tube, July 2015.

[114] A. Üneri, M. Balicki, J. Handa, P. Gehlbach, R. H. Taylor, I. Iordachita, et al. New steady-hand eye robot with micro-force sensing for vitreoretinal surgery. In *IEEE RAS and EMBS International Conference on Biomedical Robotics and Biomechatronics*, pages 814–819, 2010.

[115] P. J. Swaney, A. W. Mahoney, A. A. Remirez, E. P. Lamers, B. I. Hartley, R. H. Feins, R. Alterovitz, and R. J. Webster III. Tendons, concentric tubes, and a bevel tip: three steerable robots in one transoral lung access system. In *IEEE International Conference on Robotics and Automation*, pages 5378–5383, 2015.

[116] The International Early Lung Cancer Action Program Investigators. Survival of patients with stage I lung cancer detected on CT screening. *The New England Journal of Medicine*, 355(17):1763–1771, 2006.

[117] M. J. Horner, L. A. G. Ries, M. Krapcho, N. Neyman, R. Aminou, N. Howlader, S. F. Altekruse, E. J. Feuer, L. Huang, A. Mariotto, B. A. Miller, D. R. Lewis, M. P. Eisner, D. G. Stinchcomb, and B. K. Edwards. SEER cancer statistics review, 1975-2006, National Cancer Institute. Bethesda, MD. Available: http://seer.cancer.gov/csr/, 2009.

[118] J. S. Wang Memoli, P. J. Nietert, and G. A. Silvestri. Meta-analysis of guided bronchoscopy for the evaluation of the pulmonary nodule. *Chest*, 142(2):385–393, 2012.

[119] G. Krishna and M. K. Gould. Minimally invasive techniques for the diagnosis of peripheral pulmonary nodules. *Current Opinion in Pulmonary Medicine*, 14:282–286, 2008.

[120] N. Kothary, L. Lock, D. Y. Sze, and L. V. Hofmann. Computed tomography–guided percutaneous needle biopsy of pulmonary nodules: impact of nodule size on diagnostic accuracy. *Clinical Lung Cancer*, 10(5):360–363, 2009.

[121] T. Miyazawa. History of the flexible bronchoscope. *Progress in Respiratory Research: Interventional Bronchoscopy. Basel: Krager*, pages 16–21, 2000.

[122] W. A. Baaklini, M. A. Reinoso, A. B. Gorin, A. Sharafkaneh, and P. Manian. Diagnostic yield of fiberoptic bronchoscopy in evaluating solitary pulmonary nodules. *Chest*, 117(4):1049–1054, 2000.

[123] C. Gilbert, J. Akulian, R. Ortiz, H. Lee, and L. Yarmus. Novel bronchoscopic strategies for the diagnosis of peripheral lung lesions: Present techniques and future directions. *Respirology*, 19(5):636–644, 2014.

[124] S. A. Merritt, J. D. Gibbs, K.-C. Yu, V. Patel, L. Rai, D. C. Cornish, R. Bascom, and W. E. Higgins. Image-guided bronchoscopy for peripheral lung lesions: a phantom study. *Chest*, 134(5):1017–1026, 2008.

[125] T. R. Gildea, P. J. Mazzone, D. Karnak, M. Meziane, and A. C. Mehta. Electromagnetic navigation diagnostic bronchoscopy: a prospective study. *American Journal of Respiratory and Critical Care Medicine*, 174(9):982–989, 2006.

[126] D. Makris, A. Scherpereel, S. Leroy, B. Bouchindhomme, J.-B. Faivre, J. Remy, P. Ramon, and C.-H. Marquette. Electromagnetic navigation diagnostic bronchoscopy for small peripheral lung lesions. *The European Respiratory Journal*, 29(6):1187–1192, 2007.

[127] R. Eberhardt, D. Anantham, F. Herth, D. Feller-Kopman, and A. Ernst. Electromagnetic navigation diagnostic bronchoscopy in peripheral lung lesions. *Chest*, 131(6):1800–1805, 2007.

[128] W. Krimsky and L. M. Seijo. Bronchoscopy and the peripheral nodule in the age of lung cancer screening and targeted therapies. *Current Respiratory Care Reports*, 1(1):67–71, 2012.

[129] F. J. Herth, R. Eberhardt, D. Sterman, G. A. Silvestri, H. Hoffmann, and P. L. Shah. Bronchoscopic transparenchymal nodule access (BTPNA): first in human trial of a novel procedure for sampling solitary pulmonary nodules. *Thorax*, 70(4):326–332, 2015.

[130] M. Takai, T. Izumo, C. Chavez, T. Tsuchida, and S. Sasada. Transbronchial needle aspiration through a guide sheath with endobronchial ultrasonography (GS-TBNA) for peripheral pulmonary lesions. *Annals of Thoracic and Cardiovascular Surgery*, 20(1):19–25, 2014.

[131] H. B. Gilbert, D. C. Rucker, and R. J. Webster III. *Concentric tube robots: the state of the art and future directions*, volume 114, pages 253–269. Springer International Publishing, 16 edition, 2016.

[132] R. J. Webster III, A. M. Okamura, and N. J. Cowan. Toward active cannulas: Miniature snake-like surgical robots. In *IEEE/RSJ International Conference on Intelligent Robots and Systems*, pages 2857–2863, 2006.

[133] P. Sears and P. Dupont. A steerable needle technology using curved concentric tubes. In *IEEE/RSJ International Conference on Intelligent Robots and Systems*, pages 2850–2856, 2006.

[134] M. Torabi, R. Gupta, and C. Walsh. Compact robotically steerable image-guided instrument for multi-adjacent-point (map) targeting. *IEEE Transactions on Robotics*, 30(4):802–815, 2014.

[135] H. Yu, J.-H. Shen, K. Joos, and N. Simaan. Design, calibration and preliminary

testing of a robotic telemanipulator for OCT guided retinal surgery. In *IEEE International Conference on Robotics and Automation*, pages 225–231, 2013.

[136] L. A. Lyons, R. J. Webster III, and R. Alterovitz. Motion planning for active cannulas. In *IEEE/RSJ International Conference on Intelligent Robots and Systems*, pages 801–806, 2009.

[137] E. J. Butler, R. Hammond-Oakley, S. Chawarski, A. H. Gosline, P. Codd, T. Anor, J. R. Madsen, P. E. Dupont, and J. Lock. Robotic neuro-endoscope with concentric tube augmentation. In *IEEE/RSJ International Conference on Intelligent Robots and Systems*, pages 2941–2946, 2012.

[138] N. Abolhassani, R. V. Patel, and M. Moallem. Needle insertion into soft tissue: a survey. *Medical Engineering & Physics*, 29(4):413–431, 2007.

[139] K. B. Reed, A. Majewicz, V. Kallem, R. Alterovitz, K. Goldberg, N. J. Cowan, and A. M. Okamura. Robot-assisted needle steering. *IEEE Robotics and Automation Magazine*, 18(4):35–46, 2011.

[140] L. A. Lyons, R. J. Webster III, and R. Alterovitz. Planning active cannula configurations through tubular anatomy. In *IEEE International Conference on Robotics and Automation*, pages 2082–2087, 2010.

[141] L. G. Torres, R. J. Webster III, and R. Alterovitz. Task-oriented design of concentric tube robots using mechanics-based models. In *IEEE/RSJ International Conference on Intelligent Robots and Systems*, pages 4449–4455, 2012.

[142] D. C. Rucker, J. Das, H. B. Gilbert, P. J. Swaney, M. I. Miga, N. Sarkar, and R. J. Webster III. Sliding mode control of steerable needles. *IEEE Transactions on Robotics*, 29:1289–1299, 2013.

[143] E. P. Lamers, A. A. Remirez, P. J. Swaney, and R. J. Webster III. A bronchial puncture mechanism for transoral access to the lung parenchyma. In *Design of Medical Devices Conference*, 2015.

[144] R. J. Hendrick, H. B. Gilbert, and R. J. Webster III. Designing snap-free concentric tube robots: A local bifurcation approach. In *IEEE International Conference on Robotics and Automation*, pages 2256–2263, 2015.

[145] J. Ha, F. Park, and P. Dupont. Achieving elastic stability of concentric tube robots through optimization of tube precurvature. In *IEEE/RSJ International Conference on Intelligent Robots and Systems*, pages 864–870, 2014.

[146] D. Minhas, J. Engh, and C. Riviere. Testing of neurosurgical needle steering via duty-cycled spinning in brain tissue in vitro. In *International Conference of the IEEE Engineering in Medicine and Biology Society*, pages 258–261, 2009.

[147] H. B. Gilbert, J. Neimat, and R. J. Webster III. Concentric tube robots as steerable needles: Achieving follow-the-leader deployment. *IEEE Transactions on Robotics*, 31(2):246–258, 2015.

[148] J. R. Bekeny, P. J. Swaney, R. J. Webster III, P. T. Russell, and K. D. Weaver. Forces applied at the skull base during transnasal endoscopic transsphenoidal pituitary tumor excision. *Journal of Neurological Surgery. Part B, Skull Base*, 74(6):337, 2013.

[149] J. D. Casler, A. M. Doolittle, and E. A. Mair. Endoscopic surgery of the anterior skull base. *The Laryngoscope*, 115(1):16–24, 2005.

[150] M. S. Kabil, J. B. Eby, and H. K. Shahinian. Fully endoscopic endonasal vs. transseptal transsphenoidal pituitary surgery. *Minimally Invasive Neurosurgery*, 48(06):348–354, 2005.

[151] G. Zada, D. F. Kelly, P. Cohan, C. Wang, and R. Swerdloff. Endonasal transsphenoidal approach to treat pituitary adenomas and other sellar lesions: an assessment of efficacy, safety, and patient impressions of the surgery. *Journal of Neurosurgery*, 98(2):350–358, 2003.

[152] A. Tabaee, V. K. Anand, Y. Barrón, D. H. Hiltzik, S. M. Brown, A. Kacker, M. Mazumdar, and T. H. Schwartz. Endoscopic pituitary surgery: a systematic review and meta-analysis. *Journal of Neurosurgery*, 111(3):545–554, 2009.

[153] H.-D. Jho and R. L. Carrau. Endoscopic endonasal transsphenoidal surgery: experience with 50 patients. *Journal of Neurosurgery*, 87(1):44–51, 1997.

[154] H.-D. Jho. Endoscopic transsphenoidal surgery. *Journal of Neuro-Oncology*, 54(2):187–195, 2001.

[155] A. Rudnik, T. Zawadzki, M. Wojtacha, P. Bazowski, J. Gamrot, B. Galuszka-Ignasiak, and I. Duda. Endoscopic transnasal transsphenoidal treatment of pathology of the sellar region. *Minimally Invasive Neurosurgery*, 48(2):101–107, 2005.

[156] I. Koren, T. Hadar, Z. H. Rappaport, and E. Yaniv. Endoscopic transnasal transsphenoidal microsurgery versus the sublabial approach for the treatment of pituitary tumors: endonasal complications. *The Laryngoscope*, 109(11):1838–1840, 1999.

[157] D.-Y. Cho and W.-R. Liau. Comparison of endonasal endoscopic surgery and sublabial microsurgery for prolactinomas. *Surgical neurology*, 58(6):371–375, 2002.

[158] M. T. Sheehan, J. L. Atkinson, J. L. Kasperbauer, B. J. Erickson, and T. B. Nippoldt. Preliminary comparison of the endoscopic transnasal vs the sublabial transseptal approach for clinically nonfunctioning pituitary macroadenomas. *Mayo Clinic Proceedings*, 74(7):661–670, 1999.

[159] P. Cappabianca, L. M. Cavallo, A. Colao, and E. de Divitiis. Surgical complications associated with the endoscopic endonasal transsphenoidal approach for pituitary adenomas. *Journal of Neurosurgery*, 97(2):293–298, 2002.

[160] D. R. White, R. E. Sonnenburg, M. G. Ewend, and B. A. Senior. Safety of minimally invasive pituitary surgery (mips) compared with a traditional approach. *The Laryngoscope*, 114(11):1945–1948, 2004.

[161] R. T. Kelley, J. L. Smith, and G. M. Rodzewicz. Transnasal endoscopic surgery of the pituitary: modifications and results over 10 years. *The Laryngoscope*, 116(9):1573–1576, 2006.

[162] S. Shah and G. Har-El. Diabetes insipidus after pituitary surgery: incidence after traditional versus endoscopic transsphenoidal approaches. *American Journal of Rhinology*, 15(6):377–379, 2001.

[163] C. H. Snyderman, H. Pant, R. L. Carrau, D. Prevedello, P. Gardner, and A. B. Kassam. What are the Limits of Endoscopic Sinus Surgery?: The Expanded Endonasal Approach to the Skull Base. *The Keio Journal of Medicine*, 58(3):152–160, 2009.

[164] L. M. Cavallo, F. Esposito, and P. Cappabianca. Surgical limits in transnasal approach to opticocarotid region and planum sphenoidale: an anatomic cadaveric study. *World Neurosurgery*, 73(4):301–303, 2010.

[165] P. Cappabianca, L. M. Cavallo, and E. de Divitiis. Endoscopic endonasal transsphenoidal surgery. *Neurosurgery*, 55(4):933–941, 2004.

[166] E. de Divitiis, P. Cappabianca, and L. M. Cavallo. Endoscopic transsphenoidal approach: adaptability of the procedure to different sellar lesions. *Neurosurgery*, 51(3):699–707, 2002.

[167] A. Garg, R. C. Dwivedi, S. Sayed, R. Katna, A. Komorowski, K. A. Pathak, P. Rhys-Evans, and R. Kazi. Robotic surgery in head and neck cancer: a review. *Oral Oncology*, 46(8):571–6, 2010.

[168] A. Parmar, D. G. Grant, and P. Loizou. Robotic Surgery in Ear Nose and Throat. *European Archives of Oto-Rhino-Laryngology*, 267(4):625–633, 2010.

[169] A. Arora, A. Cunningham, G. Chawdhary, C. Vicini, G. S. Weinstein, A. Darzi, and N. Tolley. Clinical applications of Telerobotic ENT-Head and Neck surgery. *International Journal of Surgery*, 9(4):277–84, 2011.

[170] M. Kupferman, F. Demonte, F. C. Holsinger, and E. Hanna. Transantral robotic access to the pituitary gland. *Otolaryngology–Head and Neck Surgery*, 141(3):413–5, 2009.

[171] B. W. O'Malley and G. S. Weinstein. Robotic skull base surgery: preclinical investigations to human clinical application. *Archives of Otolaryngology–Head & Neck Surgery*, 133(12):1215–1219, 2007.

[172] V. Karimyan, M. Sodergren, J. Clark, G.-Z. Yang, and A. Darzi. Navigation systems and platforms in natural orifice translumenal endoscopic surgery (NOTES). *International Journal of Surgery*, 7(4):297–304, 2009.

[173] F. Borumandi, M. Heliotis, C. Kerawala, B. Bisase, and L. Cascarini. Role of robotic surgery in oral and maxillofacial, and head and neck surgery. *British Journal of Oral and Maxillofacial Surgery*, 50(5):389–393, 2012.

[174] M. Piccigallo, U. Scarfogliero, C. Quaglia, G. Petroni, P. Valdastri, A. Menciassi, and P. Dario. Design of a novel bimanual robotic system for single-port laparoscopy. *IEEE/ASME Transactions on Mechatronics*, 15(6):871–878, 2010.

[175] P. F. Escobar, M. Kebria, and T. Falcone. Evaluation of a novel single-port robotic platform in the cadaver model for the performance of various procedures in gynecologic oncology. *Gynecologic Oncology*, 120(3):380–384, 2011.

[176] A. Bajo, R. E. Goldman, L. Wang, D. Fowler, and N. Simaan. Integration and preliminary evaluation of an insertable robotic effectors platform for single port access surgery. In *IEEE International Conference on Robotics and Automation*, pages 3381–3387, 2012.

[177] J. Wurm, T. Dannenmann, C. Bohr, H. Iro, and K. Bumm. Increased safety in robotic paranasal sinus and skull base surgery with redundant navigation and automated registration. *International Journal of Medical Robotics and Computer Assisted Surgery*, 01(03):42, 2005.

[178] M. Matinfar, C. Baird, A. Batouli, R. Clatterbuck, and P. Kazanzides. Robot-Assisted Skull Base Surgery. In *IEEE/RSJ International Conference on Intelligent Robots and Systems*, pages 865–870, 2007.

[179] T. Xia, C. Baird, G. Jallo, K. Hayes, N. Nakajima, N. Hata, and P. Kazanzides. An integrated system for planning, navigation and robotic assistance for skull base surgery. *International Journal of Medical Robotics and Computer Assisted Surgery*, 4(4):321–30, 2008.

[180] H.-S. Yoon, S. M. Oh, J. H. Jeong, S. H. Lee, K. Tae, K.-C. Koh, and B.-J. Yi. Active bending endoscope robot system for navigation through sinus area. In *IEEE/RSJ International Conference on Intelligent Robots and Systems*, pages 967–972, 2011.

[181] P. E. Dupont, J. Lock, B. Itkowitz, and E. Butler. Design and control of concentric-tube robots. *IEEE Transactions on Robotics*, 26:209–225, 2010.

[182] D. C. Rucker, B. A. Jones, and R. J. Webster III. A Geometrically Exact Model

for Externally Loaded Concentric-Tube Continuum Robots. *IEEE Transactions on Robotics*, 26(5):769–780, 2010.

[183] T. Anor, J. R. Madsen, and P. E. Dupont. Algorithms for design of continuum robots using the concentric tubes approach: a neurosurgical example. In *IEEE International Conference on Robotics and Automation*, pages 667–673, 2011.

[184] G. Guthart and J. Salisbury. The Intuitive telesurgery system: overview and application. In *IEEE International Conference on Robotics and Automation*, pages 618–621, 2000.

[185] J. K. Liu, L. D. Christiano, S. K. Patel, R. S. Tubbs, and J. A. Eloy. Surgical nuances for removal of tuberculum sellae meningiomas with optic canal involvement using the endoscopic endonasal extended transsphenoidal transplanum transtuberculum approach. *Neurosurgical Focus*, 30(5):E2, 2011.

[186] J. Burgner, P. J. Swaney, D. C. Rucker, H. B. Gilbert, S. T. Nill, P. T. Russell III, K. D. Weaver, and R. J. Webster III. A bimanual teleoperated system for endonasal skull base surgery. In *IEEE/RSJ International Conference on Intelligent Robots and Systems*, pages 2517–2523, 2011.

[187] J. Burgner-Kahrs. *Task-specific Design of Tubular Continuum Robots for Surgical Applications*. Springer, 2015.

[188] J. Burgner, P. J. Swaney, R. A. Lathrop, K. D. Weaver, and R. J. Webster III. Debulking from within: a robotic steerable cannula for intracerebral hemorrhage evacuation. *IEEE Transactions on Biomedical Engineering*, 60(9):2567–2575, 2013.

[189] D. Makarets, G. Noh, K. Kim, and D. Lee. Preliminary study of utilizing plastic tubes as a component of continuum robots. In *International Conference on Control, Automation and Systems*, pages 217–220, 2014.

[190] E. Amanov, T.-D. Nguyen, and J. Burgner-Kahrs. Additive manufacturing of patient-specific tubular continuum manipulators. In *SPIE Medical Imaging*, pages 94151P–94151P, 2015.

[191] Fundamentals of Laparoscopic Surgery, 2012.

[192] Z. S. Roth, B. Mooring, and B. Ravani. An overview of robot calibration. *IEEE Journal of Robotics and Automation*, 3(5):377–385, 1987.

[193] J. M. Hollerbach and C. W. Wampler. The calibration index and taxonomy for robot kinematic calibration methods. *International Journal of Robotics Research*, 15(6):573–591, 1996.

[194] J.-M. Renders, E. Rossignol, M. Becquet, and R. Hanus. Kinematic calibration and geometrical parameter identification for robots. *IEEE Transactions on Robotics and Automation*, 7(6):721–732, 1991.

[195] J.-H. Borm and C.-H. Meng. Determination of optimal measurement configurations for robot calibration based on observability measure. *International Journal of Robotics Research*, 10(1):51–63, 1991.

[196] H. Zhuang and Z. S. Roth. Method for kinematic calibration of stewart platforms. *Journal of Robotic Systems*, 10(3):391–405, 1993.

[197] W. Khalil and S. Besnard. Self calibration of stewart-gough parallel robots without extra sensors. *IEEE Transaction on Robotics and Automation*, 15(6):1116–1121, 1999.

[198] D. Daney and I. Z. Emiris. Robust parallel robot calibration with partial information. In *IEEE International Conference on Robotics and Automation*, pages 3262–3267, 2001.

[199] K. Xu and N. Simaan. An investigation of the intrinsic force sensing capabilities of continuum robots. *IEEE Transactions on Robotics*, 24(3):576–587, 2008.

[200] R. J. Webster III, J. M. Romano, and N. J. Cowan. Mechanics of precurved-tube continuum robots. *IEEE Transactions on Robotics*, 25(1):67–78, 2009.

[201] L. Wang and N. Simaan. *Investigation of Error Propagation in Multi-backbone Continuum Robots*. Springer, 2014.

[202] C. Escande, T. Chettibi, R. Merzouki, V. Coelen, and P. M. Pathak. Kinematic calibration of a multisection bionic manipulator. *IEEE/ASME Transactions on Mechatronics*, 20(2):663–674, 2015.

[203] R. J. Webster III, J. M. Romano, and N. J. Cowan. Kinematics and calibration of active cannulas. In *IEEE International Conference on Robotics and Automation*, pages 3888–3895, 2008.

[204] J. Hollerbach, W. Khalil, and M. Gautier. Model identification. In *Springer Handbook of Robotics*, pages 321–344. Springer, 2008.

[205] R. J. Hendrick, C. R. Mitchell, S. D. Herrell, and R. J. Webster III. Hand-held transendoscopic robotic manipulators: a transurethral laser prostate surgery case study. *International Journal of Robotics Research*, 34(15):1559–1572, 2015.

[206] C. L. Lawson and R. J. Hanson. *Solving least squares problems*, volume 161. SIAM, 1974.

[207] J. Ding, K. Xu, R. E. Goldman, P. K. Allen, D. L. Fowler, and N. Simaan. Design, simulation and evaluation of kinematic alternatives for insertable robotic effectors platforms in single port access surgery. In *IEEE International Conference on Robotics and Automation*, pages 1053–1058, 2010.

[208] H. B. Gilbert, P. J. Swaney, J. Burgner, K. D. Weaver, P. T. Russell III, and R. J. Webster III. A feasibility study on the use of concentric tube continuum robots for endonasal skull base tumor removal. In *Hamlyn Symposium on Medical Robotics*, 2012.

[209] T. S. Higgins, C. Courtemanche, D. Karakla, B. Strasnick, R. V. Singh, J. L. Koen, and J. K. Han. Analysis of transnasal endoscopic versus transseptal microscopic approach for excision of pituitary tumors. *American Journal of Rhinology*, 22(6):649–652, 2008.

[210] G. Vargas, B. Gonzalez, C. Ramirez, A. Ferreira, E. Espinosa, V. Mendoza, G. Guinto, B. Lopez-Felix, E. Zepeda, and M. Mercado. Clinical characteristics and treatment outcome of 485 patients with nonfunctioning pituitary macroadenomas. *International Journal of Endocrinology*, 2015.

[211] W. Sun, L. G. Torres, J. van den Berg, and R. Alterovitz. Safe motion planning for imprecise robotic manipulators by minimizing probability of collision. In *International Symposium on Robotics Research*, pages 685–701, 2013.

[212] A. Mahoney, T. Bruns, P. J. Swaney, and R. J. Webster III. On the inseparable nature of sensor selection, sensor placement, and state estimation in continuum robots or "where to put your sensors and how to use them". In *IEEE International Conference on Robotics and Automation*, pages 4472 – 4478, 2016.

[213] X.-Y. Gong, A. R. Pelton, T. W. Duerig, N. Rebelo, and K. Perry. Finite element analysis and experimental evaluation of superelastic nitinol stent. In *International Conference on Shape Memory and Superelastic Technologies*, pages 453–462, 2004.

[214] C. Bergeles, A. H. Gosline, N. V. Vasilyev, P. J. Codd, P. J. del Nido, and P. E. Dupont. Concentric tube robot design and optimization based on task and anatomical constraints. *IEEE Transactions on Robotics*, 31(1):67–84, 2015.

[215] C. Baykal, L. G. Torres, and R. Alterovitz. Optimizing design parameters for sets of concentric tube robots using sampling-based motion planning. In *IEEE/RSJ International Conference on Intelligent Robots and Systems*, pages 4381–4387, 2015.

[216] J. J. Abbott, P. Marayong, and A. M. Okamura. Haptic Virtual Fixtures for Robot-Assisted Manipulation. *Springer Tracts in Advanced Robotics*, pages 49–64, 2007.

[217] T. Travaglini, P. J. Swaney, K. D. Weaver, and R. J. Webster III. Initial experiments with the leap motion as a user interface in robotic endonasal surgery. In *IFTOMM International Symposium on Robotics & Mechatronics*, 2015.

Appendices

Appendix A

Constructing a Flexure-Tip Steerable Needle

This appendix is included to assist those who want to build a flexure-tip needle for research. Since the publication of [6], I have had multiple requests from other steerable needle researchers seeking guidance creating flexure-tip needles, in addition to hearing other graduate students at conferences discuss their attempts at building the needle. During the initial prototyping of my first flexure-tip needle, I had many failures myself and understand how difficult building such a small articulating needle can be. This guide provides the best building and assembly practices I have discovered thus far, and I hope it saves other graduate students and researchers time and effort.

A.1 Items Needed

- Nitinol tube (superelastic) sized to the desired needle gauge
- 0.127 mm nitinol wire (superelastic)
- JB-Kwik epoxy
- Wicking super glue
- Dremel tool with cutoff wheel and abrasive wheel
- Drill bit sized to slightly larger than OD of nitinol tube
- Drill bit sized to slightly smaller than ID of nitinol tube
- Items for fixturing such as acrylic or aluminum blocks
- Acrylic sheet (at least 12.7 mm)

- Flat surface of thickness $= \frac{OD}{2} - \frac{0.127}{2}$ mm. Note that sheets of paper work extremely well here.

A.2 Build Process

1. Smooth the end of the nitinol tube being used to create the flexure-tip needle. Do this with the Dremel tool.

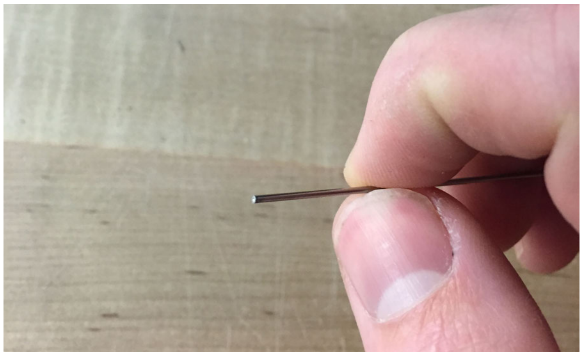

2. Use the dremel tool to bevel the end of the nitinol tube. The length and angle of the bevel can be varied, but we have seen the best performance in gelatin using a bevel length of 4 mm and a bevel angle of approximately 10 °.

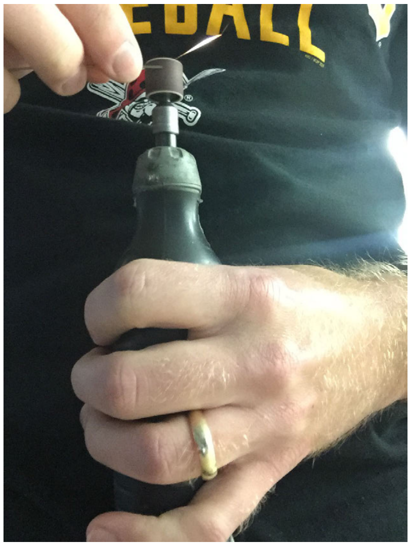

3. Using the drill bit sized slightly larger than the OD of the tube, drill a vertical hole in the acrylic sheet that is deeper than the length of the bevel by at least 1 mm.

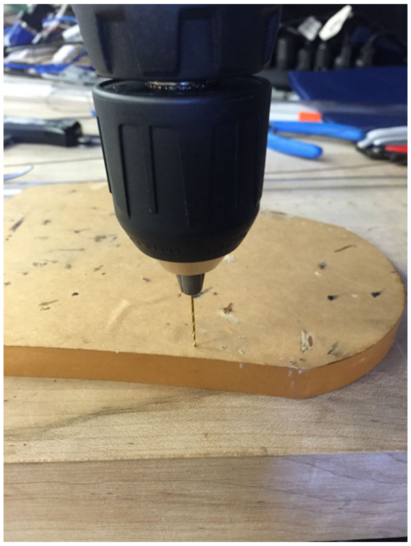

4. Place the nitinol tube with the beveled end in the hole you just created in the acrylic sheet.

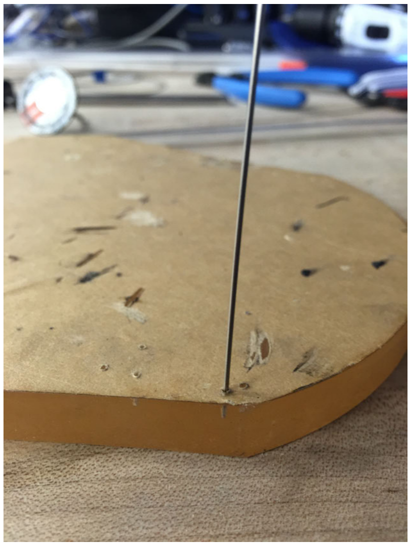

5. Use the dremel cutoff wheel to separate the bevel needle tip from the nitinol tube. It is fine if the nitinol sticks up above the acrylic sheet, the length of the bevel tip will be adjusted in the next step.

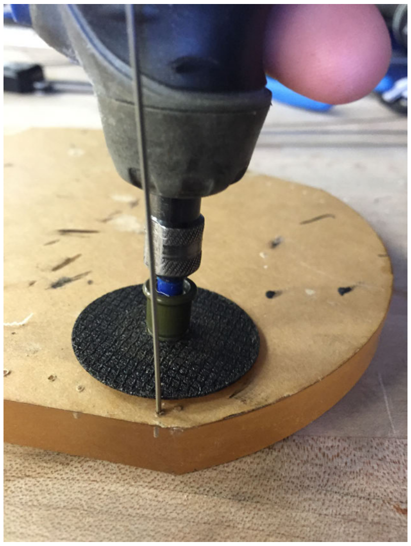

6. Using the abrasive wheel on the dremel, clean up and smooth the end of the bevel tip making it parallel to the acrylic sheet. This step is important, as it helps to ensure an even gap between the bevel tip and the needle shaft.

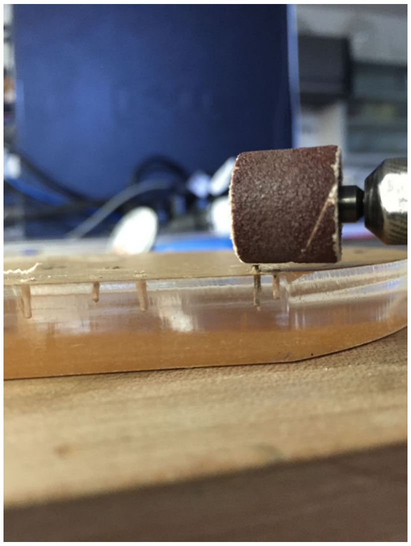

7. Clean up the inside of the bevel tip by using the drill bit sized slightly smaller than the ID of the nitinol tube to remove any nitinol chips left by the abrasive cutting wheel.

8. Remove the bevel tip from the acrylic sheet and use sandpaper to remove any leftover rough edges from the bevel tip, these will mostly occur at the back of the bevel tip.

9. Place the bevel tip in a safe location (it is prone to get lost due to the small size) and cut off three short (≈ 30 mm) lengths of 0.127 mm nitinol wire.

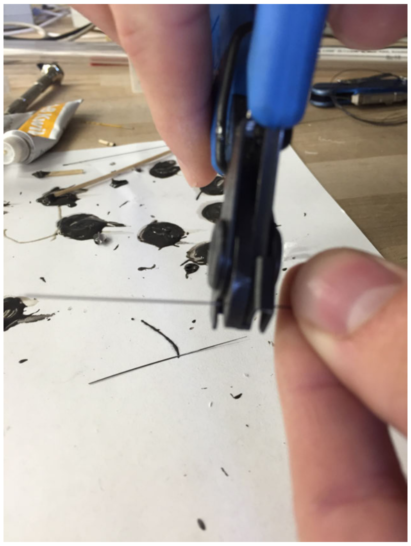

10. Prepare a small batch of JB-Kwik. Take the 3 nitinol wires and align one of their ends, ensuring that the wires lie in a plane. Do this with your fingers and then dip the end of the nitinol wires in the JB-Kwik. Remove excess JB-Kwik, this step is just to keep the wires aligned. Additionally, you can apply wicking grade super glue to the end of the wires after using JB-Kwik to ensure that the wires stay aligned.

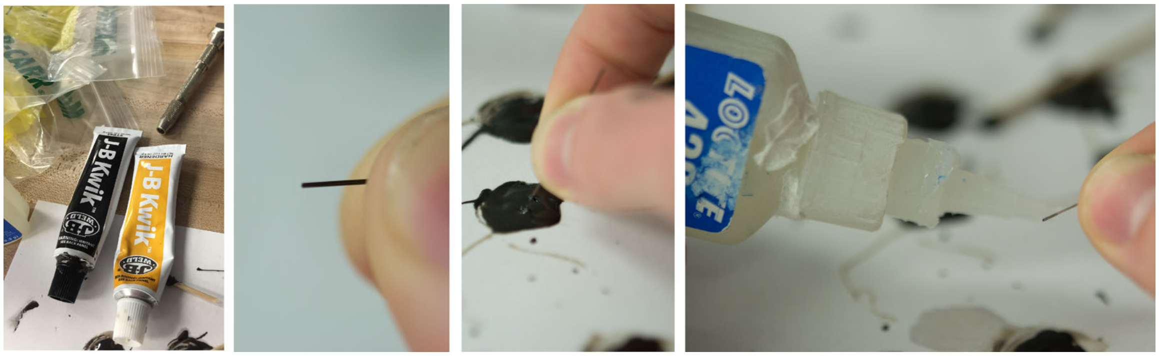

11. Retrieve the bevel tip from the safe location you placed it, and using a small nitinol wire or similar disposable instrument, place JB-Kwik on the flat end of the bevel tip where you will insert the 3 aligned nitinol wires that comprise the flexure joint.

12. Place JB-Kwik on the end of the 3 aligned nitinol wires as well, and insert the aligned wires into the bevel tip. Ensure that the wires do not protrude out from the bevel tip, and use additional JB-Kwik if needed. Clean up any JB-Kwik that is not located inside the bevel tip using a thin nitinol wire or sheet of paper.

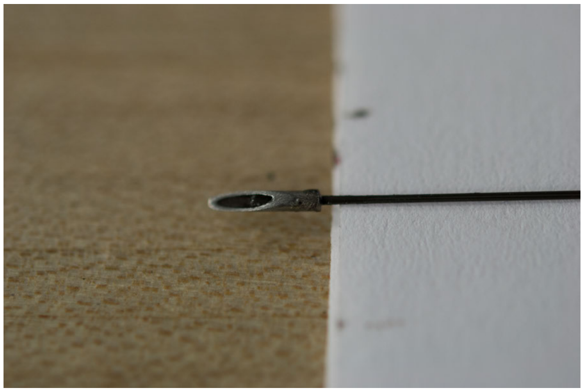

13. Using the flat surface of thickness $= \frac{OD}{2} - \frac{0.127}{2}$ mm (again, try using sheets of paper), place the aligned nitinol wires on this surface and the bevel tip on the table top. This aligns the nitinol wires with the approximate center line of the bevel tip. Ensure that the bevel tip is aligned with the nitinol wires such that a force on the bevel tip causes the flexure to bend (see [6] for details). Also ensure that the nitinol wires are parallel to the bevel tip. Place a weight or fixturing piece on both the nitinol wires and the bevel tip to keep both aligned while the epoxy sets.

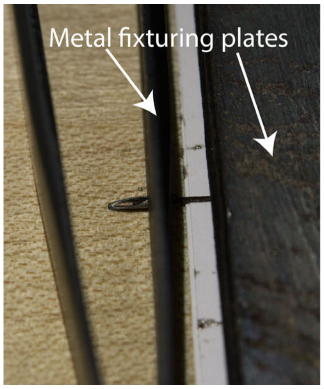

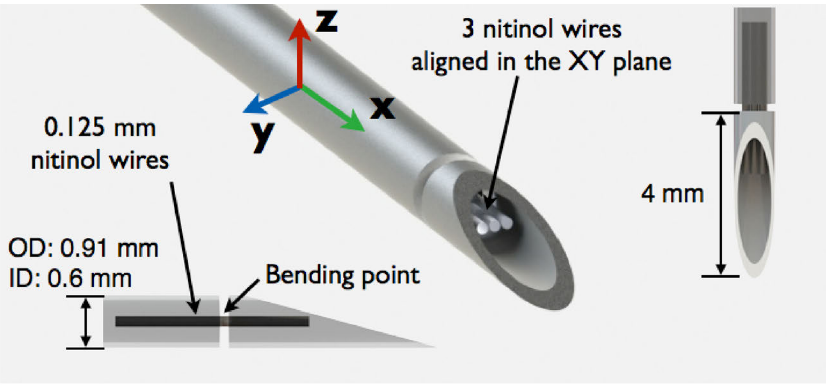

14. After the epoxy has set, cut off the excess length of nitinol wires, leaving only ≈ 8-10 mm of nitinol wire.

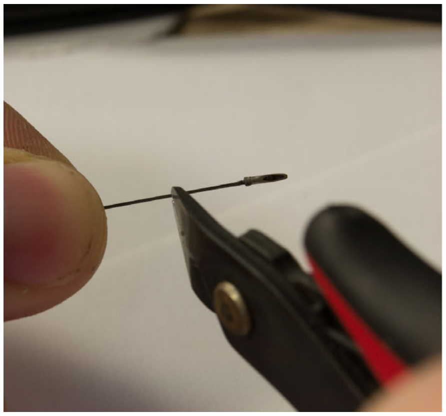

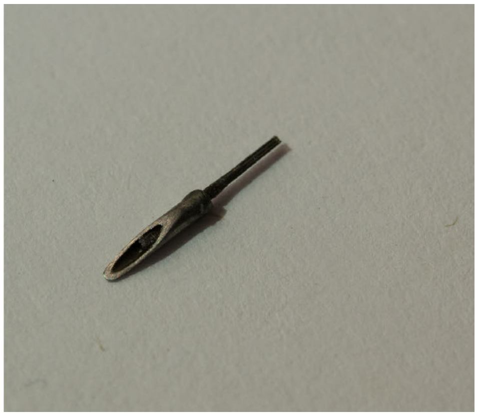

15. Clean up the leftover nitinol tube that will comprise the needle shaft as was done in Step 1. Make another batch of JB-Kwik and dip the end of the nitinol wires in it. Also, place JB-Kwik on the end of the nitinol tube. Finally, insert the nitinol wires into the needle shaft, leaving a small gap between the bevel tip and the needle shaft. You can use a sheet of paper or a thin nitinol wire to clean up any epoxy that is bridging the gap between the bevel tip and the needle shaft. It is critical to make sure that the needle shaft and the bevel tip are parallel to one another, you can use a straight-edge to do this.

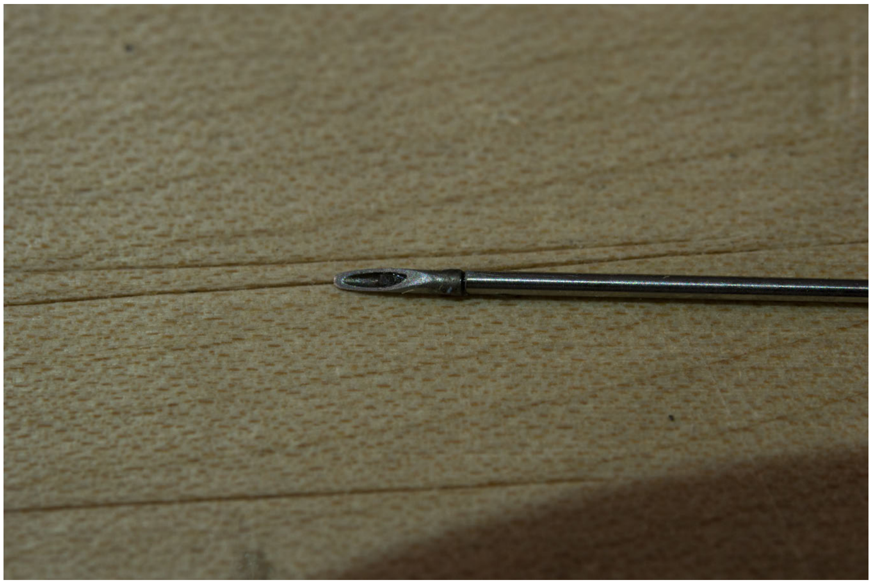

16. Let the epoxy set for at least 10 minutes, and then you can test the flexure-tip by bending it by hand until the bevel tip hits the needle shaft (the hard stop). If the flexure-tip does not perform well (is too stiff or too flimsy), you can remove the bevel tip and clean out the epoxy from the nitinol tube using the drill and appropriately sized bit and start again.

17. Finally, fill in the bevel tip with epoxy to make a smooth beveled surface.